Numerical Investigation of Passive Heat Transfer Enhancement in Mixed Convective Turbulent Flows

By

Vasileios Champilomatis

Student Nr: 5135184

in partial fulfilment of the requirements for the degree of

Master of Science

in Mechanical Engineering,
track of
Energy, Flow & Process Technology

at the Delft University of Technology,

to be defended publicly on the
10th December 2021

Supervisor:	Dr.ir. J.W.R. Peeters
Thesis committee:	Prof. dr. ir. B.J. Boersma
	Dr. ir. M.J.B.M. Pourquie

TU Delft

Contents

List of Figures

List of Tables

Abstract

Heat transfer deterioration has been observed by researchers in turbulent upward flows under the effect of buoyancy. This is a problem for industrial applications since deteriorated heat transfer requires heat exchangers of increased volume and cost. Passive heat transfer enhancement in turbulent mixed convection upward flows through a uniformly heated pipe is studied numerically, using RANS modelling. A constant properties approach is implemented, using the Boussinesq approximation to predict the influence of buoyancy. Turbulence is modelled using two different models, the “Menter shear stress transport turbulence model” and “Spalart-Allmaras” model. Numerical simulations of air flows are conducted at a turbulent Reynolds number of $Re = 5300$, at a uniform pipe wall heating rate of $q_{wall} = 1285\ W/m^2$. The effect of transverse rib geometries on heat transfer is studied for various pitch-to-diameter, p/D, and depth-to-diameter, e/D, ratios, with ranges equal to $p/D = 1 - 1.75$ and $e/D = 0.1 - 0.175$. The effect of ribs on heat transfer is compared to the effect on flow friction, using the overall enhancement ratio, η. Results show that transverse rib geometries can lead to a maximum overall enhancement of $\eta = 2.20$ and $\eta = 2.30$ depending on the turbulence model. Recommendations for further research are presented in the end.

1.Introduction

1.1 Importance of Heat Transfer

When it comes to engineering, heat transfer is highly important to many applications, concerning conversion, exchange, use or generation of heat. Heat exchangers, devices for transferring or dissipating heat, are used nowadays in refrigeration, air conditioning, space heating, power generation and chemical processes and are essential parts of most industries associated with the modern world. The search for efficient energy usage has led engineers to developing different structures and architectures of heat transfer devices, aiming to reduce size, cost, and fuel consumption.

Since the 20th century, much attention has been given to enhancing the heat transfer performance of devices related to the matter, by different means including taking advantage of surface roughness structures that have shown to have a positive effect on heat transfer, by promoting turbulence in the flow of working fluids. Results of experimental and numerical studies are promising, although there are still engineering areas that have not been investigated in depth. Turbulent mixed convection flows, or flows that combine forced and natural convection, are found in many engineering applications, including electronic devices cooled by fans, nuclear reactors, gas-cooled reactors, supercritical water-cooled reactors, solar chimney power plants and rocket propulsion systems. In such flows, where buoyant and pressure forces interact, it has been observed that the flow tends to become laminar at certain points, depending on the case, causing heat transfer to deteriorate and heat transfer rates to drop, since turbulence promotes mixing of the flow, which favors heat transfer by convection. There has not been extensive research around the effect that surface roughness would have on mixed convection flows, although it seems logical that certain geometries could prevent their laminarization and lead to higher heat transfer efficiency. Thus, surface roughness effect on turbulent mixed convection is a highly promising and interesting subject and will be the focus of this study.

In the following section mixed convection flows and the problems encountered when dealing with such flows are discussed. Subsequently, classical heat transfer augmentation techniques and their effect on heat transfer and flow drag are shown. Finally, a brief review on modelling techniques on relevant flows is presented concluding into the main research questions of this thesis.

1.2 Buoyancy Driven Turbulent Flows (Heat Transfer Deterioration)

Mixed convection flows occur in many technological applications, including solar receivers exposed to wind currents, electronic devices cooled by fans, cooling of nuclear reactors and more and, generally, mixed convection occurs when natural and forced convection mechanisms act together to transfer heat. The term mixed convection, according to Jackson [1], describes heat transfer in flows where a non-uniform density variation exists, leading to gravitational body force variations. Such variations result into a flow field with significant differences compared to a fluid that flows under uniform density conditions. Jackson [1] states that the effects of buoyancy on heat transfer can be the dominant factor on turbulent regimes. In this work, a comprehensive review of experimental and theoretical studies on mixed convection flow in vertical tubes is presented. As shown in Jackson's work, in upward flows, where forced and free convection are aligned, local heat transfer coefficients are lower than those for forced flow alone. It is reported that with higher effects of buoyancy, heat transfer becomes enhanced, while it is impaired under moderate buoyancy effect.

The study of turbulent mixed convection through channels has received considerable attention through the years. Wang et al. [2] studied experimentally buoyancy-aided and buoyancy-opposed turbulent flows in a vertical plane passage. Zhang et al. [3] presents experimental measurements and analysis of buoyancy-assisted mixed convection in a vertical square channel. Kasagi et al. [4] used Direct Numerical Simulations (DNS) to investigate turbulent mixed convection between two vertical parallel plates kept at different temperatures. One of the most important observations was made during early work on supercritical steam generators by Shitsman [5] and Ackerman [6], who noted severe localized heat transfer impairment in upward mixed convection flows at supercritical conditions, shown in Figure 1, and initially attributed the effect to be similar to film-boiling, named ‘’pseudoboiling’’. However, it became apparent later that the effect was a result of buoyancy and is not restricted to near-critical conditions but can occur in fluids at lower pressures as shown by experiments performed by Steiner [7], Kenning [8] and Fewster [9].

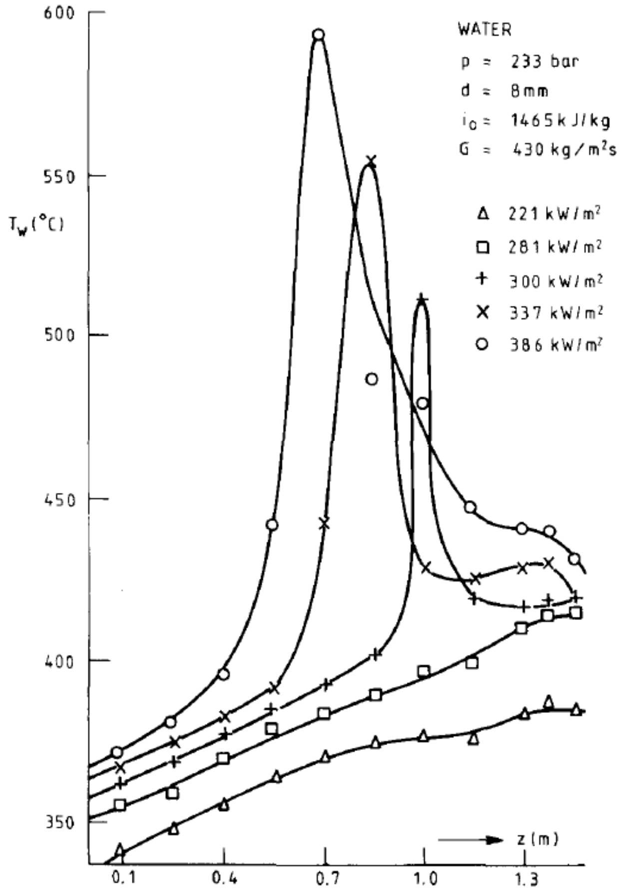

Figure 1: [34] Localized impairment of heat transfer due to buoyancy adapted from Shitsman.

An explanation about the physical mechanism behind the heat transfer deterioration in mixed convection upward flows was first proposed among others by Hall et. al [10] and is summed up in a report by Jackson [11]. In such a flow it is assumed that there is a layer of fluid at uniform density ρ_w adjacent to the wall, the buoyant layer, and a second layer with a higher density ρ_b at the core of the fluid. The distribution of the shear stress at the edge of the buoyant layer is shown in Figure 1 in which it is evident that for a particular boundary layer thickness δ, the stress is reduced to zero at the edge

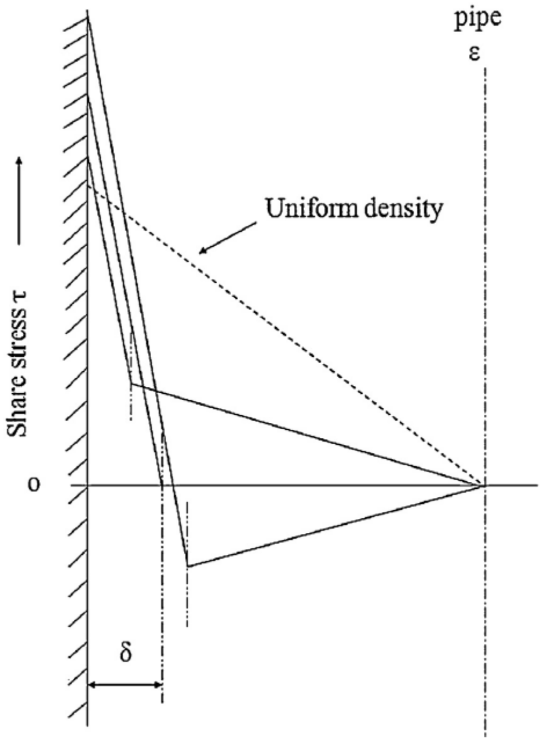

Figure 2: [11] Shear stress distributions for different thicknesses of the buoyant layer.

The effect of the shear stress distribution on the diffusion of turbulence is significant since turbulence is maintained by an energy input arising from shearing of the fluid due to the mean velocity gradient, translated as the turbulent shear stress τ_T multiplied by the velocity gradient. Ultimately, a decrease in the shear stress will result in a decrease in the turbulent shear stress and, assuming that the mixing length l does not increase significantly by the density variation, a decrease in the turbulent diffusivity given by $\varepsilon = \sqrt{\rho l^2 |\tau_T|}$. In an upward flow, as the process develops along a tube, the wall temperature rises, and the density difference becomes bigger along with the buoyant layer thickness. If the layer becomes thick enough to reduce the shear stress on the edge to zero, no energy will be fed into the turbulence and the diffusivity can be reduced to a point where the flow becomes laminar. Such a phenomenon leads to deterioration in heat transfer, which is promoted by the effect of turbulence.

1.3 Passive Heat Transfer Enhancement

The study of improved heat transfer or heat transfer enhancement or augmentation, as it is usually called, has gained increasing interest already by the end of the 20th century. According to a bibliographic report by A. E. Bergles [12], a survey in 1995 cited 5676 technical publications about heat transfer augmentation and, as stated by Popov [13], this number had risen to more than 10,000 by 2012. This increase can be justified by an increasing need for energy, material, and space saving options in different industries nowadays. In process industry, attention is given to improving performance and decreasing volume and costs of heat exchangers, examples being investigations on in-tube heat transfer augmentation [14] and heat transfer augmentation benefits on plate heat exchangers [15]. Heat transfer augmentation is also investigated in the electronic industry where micro-cooling technology is implemented [16]. Heat transfer augmentation has been recently investigated in waste heat recovery systems [17],[18], since such systems offer one of the best alternative ways of reducing fossil fuel consumption and pollution and increasing energy efficiency. Heat transfer augmentation is relevant also in space applications, where size reduction is of high interest and marine applications where the heat transfer rate of heat exchangers is decreasing due to fouling.In passive techniques there is no need for external power input and the power needed for heat transfer enhancement is taken from the system itself. They use surface or geometrical modifications to the flow channel or incorporate inserts in the flow channel. Such techniques offer high potential for various applications compared to active techniques.

As stated in Bejan's Heat Transfer Handbook [19], one of the main passive techniques for heat transfer enhancement are rough surfaces, which are generally surface modifications used to promote turbulence in the flow field, with geometric features ranging from random sand-grain roughness to discrete three-dimensional surface protrusions. Roughness structures and their effect on heat and momentum transfer has been investigated in numerous experimental and numerical reports over the last few decades. The progress in this matter has been extensively reviewed by several authors, including Dewan et. al [21] followed a decade later by Ji et. al [22]. In their reviews, works of different researchers and their results are listed, including dimpled surfaces, riblets, extended protrusions, sand roughness, corrugated and twisted tubes. The effect of such surface modifications usually has a negative effect on the momentum, leading to higher pressure losses. Therefore, as stated by Dewan et al. [21], passive heat transfer augmentation methods are evaluated using the overall enhancement ratio, which is defined as the ratio of the heat transfer enhancement ratio to the friction factor ratio, given by the following formula:

$$\eta = \frac{(Nu/Nu_0)}{(f/f_0)^{\frac{1}{3}}} \tag{1}$$

where Nu, f and Nu_0, f_0 are the Nusselt numbers and friction factors for an artificially roughened surface and a smooth surface respectively. At this point it should be mentioned that authors in most heat transfer textbooks [19], [20], state that surface roughness has a more significant effect on turbulent heat transfer compared to laminar flows. A list of experimental results of the surface roughness effect on heat transfer and friction factor in tube flows is presented in Table 1.

Table 1: Heat transfer and friction factor experimental data of artificially roughened tubes.

Researcher	Re	Fluid	Type	f/f_0	Nu/Nu_0
Rabas et. al [23]	10 – 60 x 10^3	Water	Dimples	1.5 – 1.9	1.5 – 1.6
Suresh et al. [24]	2.5 – 6 x 10^3	Water	Dimples	1 – 1.1	1.5 – 1.7
Liao and Xin [25]	0.25 – 7 x 10^3	Ethylene glycol	Extended Protrusions	1.7 – 4.4	2.6 – 3.4
Li et al. [26]	15 – 60 x 10^3	Water	Discrete Ribs	2.8 – 3.5	2 – 2.1
Darzi et al. [27]	5 – 20 x 10^3	Water/Al_2O_3	Corrugated	2.5 – 3.1	2.7 – 3.2
Garcia et al. [28]	0.1 – 100 x 10^3	Water	Corrugated	1.8 – 3.8	1.4 – 2.3
Smithberg and Landis [29]	5 – 50 x 10^3	Air, Water	Twisted Tape	2.2 – 2.7	2.3 – 2.7
Gowen and Smith [30]	6 – 100 x 10^3	Air, Water, Ethylene glycol	Sand Roughness	3.5 – 5.8	2.3 – 3.3

Artificial surface roughness has a different effect on heat transfer and friction in turbulent flows, as seen from Table 1. In the following sections both these effects will be investigated.

1.4 Roughness Effect on Turbulent Heat Transfer

Artificial roughness is used as a heat transfer enhancement method because it reduces the thermal resistance by increasing the effective heat transfer surface area but mainly promotes the generation of turbulence. As mentioned before, such an enhancement is usually accompanied by an increase in pumping power. Nunner [36] was among the first to explain the effect of surface roughness on heat transfer in the case of a fully developed turbulent flow stating that the roughness elements contribute to increased heat transfer by increasing the level of turbulence in the turbulent core. Owen and Thomson [37] proposed a model, suggesting that the presence of protrusions gives rise to eddies ‘which wrap themselves around the individual excrescences and trail downstream’, as shown in Figure 4. The effect of these eddies is to draw fluid down into the valley-like regions between adjacent roughness elements which the fluid then scours before returning to mix with the main flow near the height of the roughness crests. It is suggested that the scouring action forms the basic convective mechanism of heat transfer at the wall and heat is communicated to the fluid in the space near and beyond the roughness crests by the convective motion of the horseshoe-eddies.

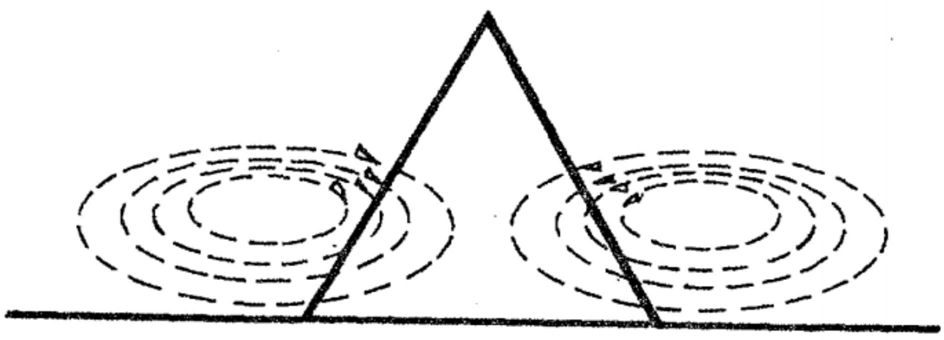

Figure 3: [37] Rough sketch of horseshoe eddies behind an excrescence proposed by Owen and Thomson.

The first researcher to propose a flow model was Nunner [36], who proposed that roughness acts to reduce the thermal resistance of the turbulence dominated wall region, without significantly affecting the viscous region. His focus, followed by works of Dipprey and Sabersky [38] was relating the Stanton number in tube flows with the skin factor, Reynolds number and molecular Prandtl number concluding into heat transfer-friction similarity laws. The experiments were performed using rough tubes containing a close-packed, granular type of surface with roughness height-to-diameter ratios ranging from 0.0024 to 0.049. By comparing analytical and experimental results the following formulas where presented:

$$St = \frac{C_f/2}{1 + 1.5Re^{-\frac{1}{8}}Pr^{-\frac{1}{6}}\left[PrC_f/C_{f,s} - 1\right]} \quad [36] \qquad (2)$$

$$St = \frac{C_f/2}{1 + \sqrt{C_f/2\left\{k_f\left[Re\sqrt{\frac{C_f}{2}}\left(\frac{\varepsilon_s}{D}\right)\right]^{0.2} Pr^{0.44} - 8.48\right\}}} \quad [38] \qquad (3)$$

where, St is the Stanton number, Re is the Reynolds number, Pr is the molecular Prandtl number, C_f is the friction coefficient for rough tubes, $C_{f,s}$ is the friction coefficient for smooth tubes, ε_s is the sand-grain roughness height, k_f is a constant depending on the roughness form and D is the tube inside diameter.

Dipprey and Sabersky [38] showed that the heat transfer enhancement exceeds the associated increase in pressure drop, although this stands only in cases where the Prandtl number was larger than 3. Similar results were obtained by Webb et al. [39], which indicated a possibility of enhancing heat transfer from rough surfaces with a minimum increase in drag. On the other hand, experimental results by Hosni et al. [40], [41] have shown that there is greater drag increase by the roughness elements than the associated heat transfer enhancement, when air is used as a fluid (Prandtl = 0.7). A theoretical study by Katoh et al. [42] on turbulent channel flows showed that when the molecular Prandtl is greater than the turbulent Prandtl number, the heat transfer enhancement can be higher than the drag enhancement, resulting into an overall enhancement ratio greater than one. As shown by Figure 5 [42], a rough surface overall enhancement ratio greater than unity can be achieved in small roughness elements, at $k^+ = 20$, when $Pr > 5$, where k^+ is used to symbolize the non-dimensional surface height. For larger heights, an overall enhancement ratio greater than unity cannot be achieved.

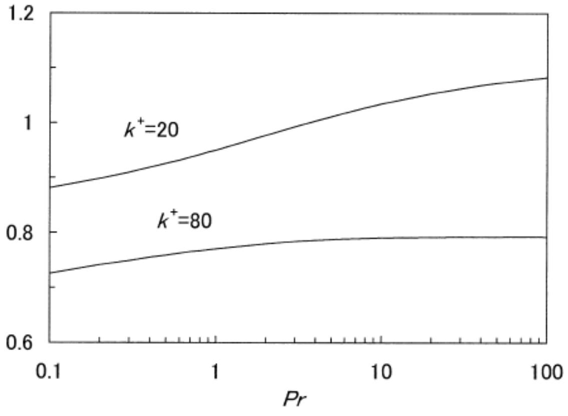

Figure 4: [42] Overall enhancement ratio of rough surfaces as a function of the Prandtl number.

Other researchers have shown that as surface height increases, the Reynolds analogy is inaccurate. Bons [43] proposed the use of the 'Reynolds analogy factor' (4) for evaluating the relative increase of heat and momentum transfer.

$$RA = \frac{2St}{C_f} \tag{4}$$

Where St and C_f denote Stanton number and skin friction coefficient respectively. He investigated several realistic rough surfaces from gas turbine blades and, after normalizing the Reynolds analogy factor with the corresponding smooth surface factor RA_0, he showed that $0.5 < \frac{RA}{RA_0} < 0.7$, meaning that momentum transfer is more enhanced by roughness than the heat transfer in such cases. Forooghi et al. [44] performed Direct Numerical Simulations (DNS) to investigate flow and heat transfer over rough surfaces with an equivalent sand roughness size of approximately 300 μm, extracted from the piston head of a single cylinder research engine. For such roughness heights, which fall into the fully rough regime, the Reynolds analogy factor as expressed by (2) was found to vary from 0.85 to 0.67. The breakdown of the Reynolds analogy has been reported in studies of flows over riblet surfaces. Choi et al. [45] carried out experiments in a low-speed wind tunnel to investigate heat transfer characteristic of triangular-profiled riblet surfaces in comparison with those of a smooth surface and noted that a 10% heat transfer coefficient increase was achieved without any drag penalty.

Although surface roughness in many cases causes a higher increase in drag compared to heat transfer, many studies have shown that the opposite can be achieved. Afanasyev et al. [46] performed an experimental investigation on spherical cavities on a flat plate placed in a wind tunnel against a low-turbulence isotropic wind flow and showed that up to an 40% heat transfer enhancement can be achieved with no appreciable effect on the hydrodynamics of the flow. Chen et al. [47] performed experiments on dimpled tubes and found that overall enhancement above one can be achieved. Such results show that heat transfer augmentation using surface roughness in turbulent flows is a promising field that should be further investigated.

1.5 Roughness Effect on Flow Friction

The effect of wall roughness has been extensively investigated for many years. Nikuradse [31] studied flow in rough pipes and worked on quantifying the effect of surface roughness on pressure drop, establishing the sand-grain roughness e, equivalent to the diameter of the sand particles used in his experiments, as a major parameter affecting the friction factor in laminar and turbulent flows. In Colebrook's work [32] the effect of surface roughness on the pressure drop is summarized in a convenient way, which became the basis for Moody diagrams, which can be found in almost any textbook on fluid mechanics.

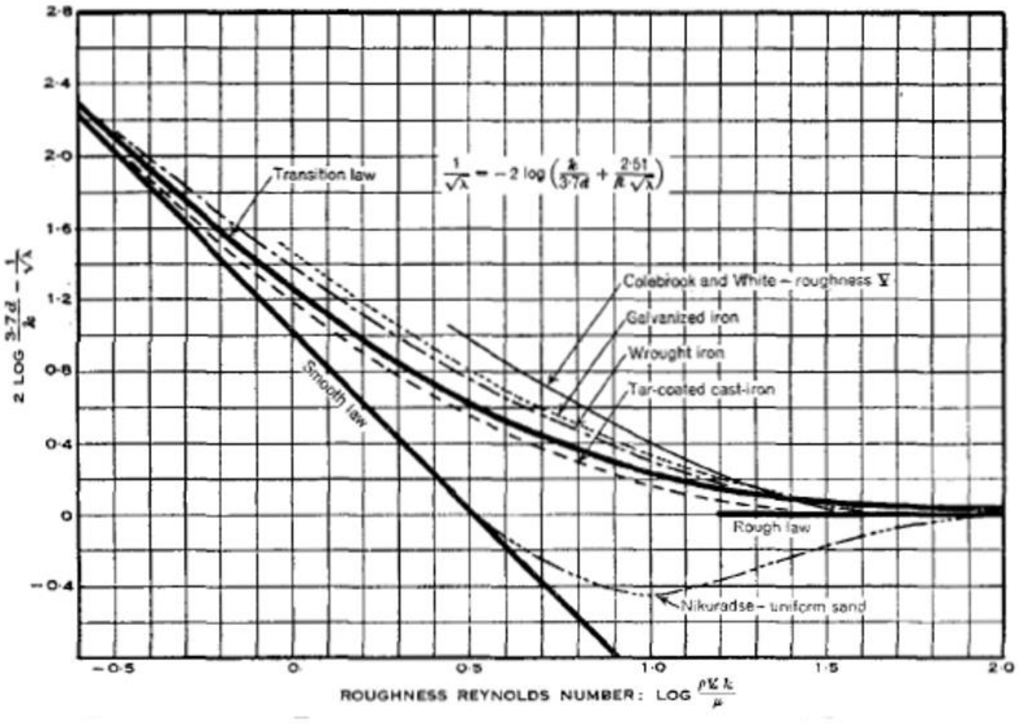

Figure 5: Colebrook's depiction of roughness's effect on the friction factor [32].

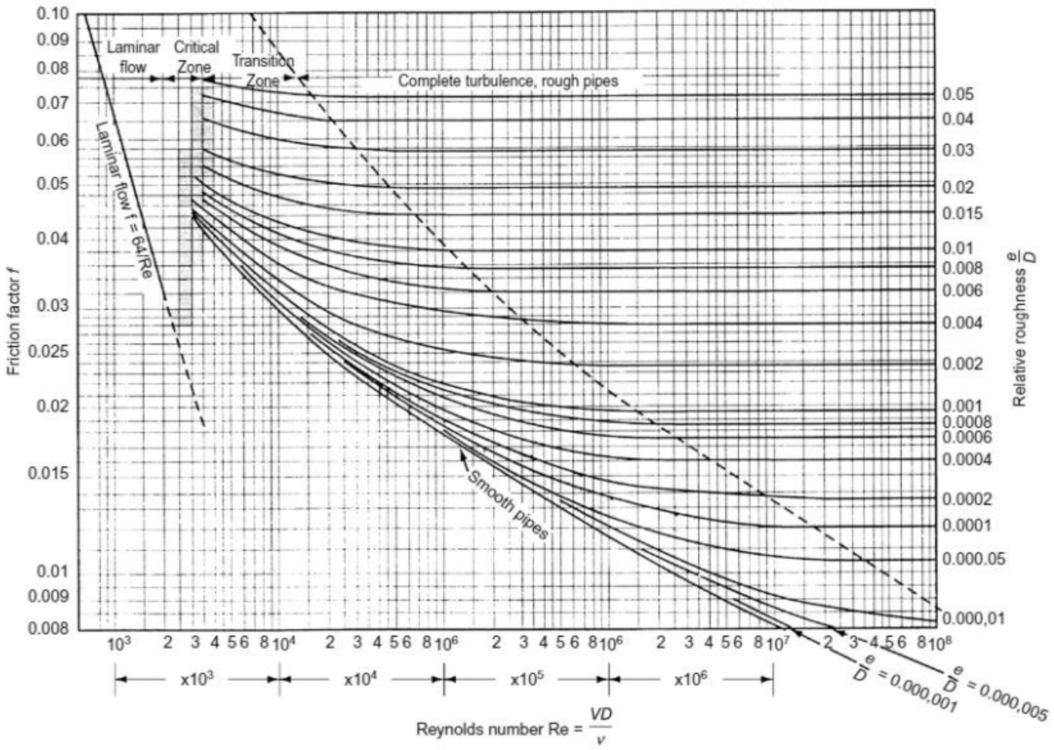

Figure 6: A typical Moody diagram, relating the Darcy–Weisbach friction factor fD, Reynolds number Re, and surface roughness for fully developed flow in a circular pipe.

In a turbulent boundary layer, vortices associated with turbulent momentum transfer and drag forces are produced and dissipated. Drag at the region next to the wall is driven by streamwise vortices which spin along the axis of the flow and are dominant in the viscous sublayer. It is the interaction of such streamwise vortices traveling through the mean flow field, with the wall surface and adjacent vortices that leads to bursting motions, leading to an increase in drag [33]. As surface roughness increases, turbulence in the flow increases and generally, friction increases [34]. An exception has been reported using riblets that are aligned with the flow direction and are able to achieve a significant reduction in drag [35].

1.6 Research Questions

Wall roughness typically leads to heat transfer and friction enhancement. Although heat transfer augmentation is always considered a positive effect, increasing friction is an unwanted by-effect. Buoyancy driven turbulent flows, found in many engineering applications, are not characterized by effective heat transfer, due to the laminarization caused by the effect of buoyancy as explained. Combining these two arguments a question arises, can passive heat transfer augmentation methods solve the problem of heat transfer deterioration in turbulent mixed convection flows? Since studies focusing on this subject are scarce and the results would be highly beneficial, it is of high importance to perform simulations on turbulent mixed convection flows on the search for an answer to the following questions:

- Can simple artificial roughness geometries promote turbulence and prevent laminarization, leading to enhanced heat transfer in mixed convection flows?
- What is the effect of roughness elements' height and arrangement on heat transfer in turbulent mixed convection flows?
- What is the cost in terms of momentum transfer and is the enhancement in heat transfer higher related to that?

Answering these questions will be the goal of the study.

2. Methodology

2.1 Reynolds – Averaged Navier – Stokes (RANS)

Engineers dealing with practical problems around the globe deal with turbulent flows in most cases, making them the focus of computational fluid dynamics (CFD) nowadays. Turbulence is a three-dimensional, unsteady phenomenon, which causes motions of various scales. The wide range of scales in motions is the main challenge in turbulence simulations since the computational domain needs to be at least an order of magnitude larger than the scales characterizing the turbulent energy, while the mesh needs to be fine enough to resolve up to the smallest dynamically significant length-scale. Direct numerical simulations (DNS) are the most accurate approach to solving such problems, since the Navier-Stokes equations are numerically solved directly for all the different length scales in the flow. This makes it a very computationally expensive tool that can be realistically used only in simple flows at low Reynolds numbers.

A computationally less intensive tool has been developed, the Reynolds-averaged Navier-Stokes (RANS) simulations, which have been used for decades to analyze turbulent flows. This tool reduces the computational time greatly by solving for time- or ensemble- averaged quantities while the effect of all the scales of instantaneous turbulent motion is modelled by a turbulence model. Such a method is practical and has served engineers in the past decades, however RANS have inherent limitations with complex, separated, and unsteady flows. In such cases, RANS models are never able to accurately reproduce an entire flow field and they are inconsistent when it comes to accurate representation of vortices, unsteady flow structure or flow recirculation regions [48]. In the present study, saving computational time is of higher importance compared to very high accuracy and thus, RANS is the tool of choice.

Although it will become clearer in the next section, in the approach of RANS, after decomposing the flow variables into mean and fluctuating parts and averaging the Navier-Stokes equations, an unknown term is produced, the **“Reynolds-stress tensor”**. Finding a way of modelling this term has been the focus of researchers since the late 1800’s, when concept of the “eddy viscosity” was proposed by Boussinesq in 1877 [49]. The main RANS models that have been developed since are classified by Alfonsi [50] in the following categories:

Zero-equation models

In such models, known also as mean-velocity field closures [51], only a system of partial differential equations for the mean field is solved.

One-equation models

Compared to the zero-equation models, an equation is added, which refers to the calculation of the turbulence velocity scale, usually in terms of the average kinetic energy. One of the most used one-equation models was developed by Spalart and Allmaras in 1994 (“*SA*” model) [52] as an attempt to give a better boundary layer prediction in the presence of adverse pressure gradients, compared to the “*k-ε*” two-equation model.

Two-equation models

Compared to the one-equation models, an additional transport equation is involved. One of the basic models that fall into this category is the “*k-ε*” model, in which the second transport equation is expressed in terms of the kinetic-energy dissipation rate, *ε*. As with the “*SA”* model, the “Standard Menter Shear Stress Transport” or simply “*k-ωSST*” model has been developed [53] for a better boundary layer representation. In this model the second equation is expressed in terms of the turbulent specific dissipation rate, ω. This model is known for its simplicity and numerical stability compared to other two-equation turbulent models. Two- and one-equation models can also be described as mean turbulent field closures [51].

Stress-equation models

This models, known also as mean Reynolds-stress closures [51], or “$\tau_{ij} - \varepsilon$” models, involve solving a number of additional transport equations for the components of the Reynolds-stress tensor τ_{ij} and one for the dissipation rate, ε, compared to the zero-equation models.

RANS in mixed convection flows

RANS is a very popular tool for simulations among researchers, due to the small computational cost compared to Direct Numerical Simulations (DNS) and examples can be also found in simulating mixed convection turbulent flows. Oler et al. [54] worked on simulating turbulent mixed convection flows in a differentially heated plane channel, assessing common RANS models while comparing them to results from obtained from DNS.

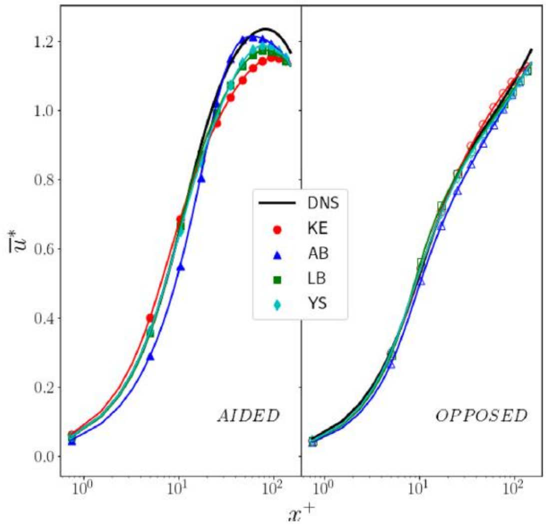

Figure 7: [54] Comparison of mean velocity profiles between RANS models and DNS.

Gentry et al. [55] compared RANS results using the “*k*-*ε*” turbulence model with experimental results referring to steady-state mixed convection sodium flows and found a very good match between computed temperatures and experimental data. Kim et al. [56] reported a CFD analysis of buoyancy-aided turbulent mixed convection flows within a heated vertical rectangular duct, using RANS modeling. Comparisons with experimental results were made using different turbulence models. Wu et al. [57] investigated transverse buoyant jet-induced mixed convection inside a large thermal cycling chamber with perforated plates, both experimentally and numerically using RANS modelling. Grassi et al. [58] studied mixed convection within heated horizontal pipes using RANS modelling and noted important deviations from experimental data as seen from Figure 8. Such recent examples show that RANS is an essential tool among researchers worldwide in a variety of engineering applications and will be the tool of choice in the current work.

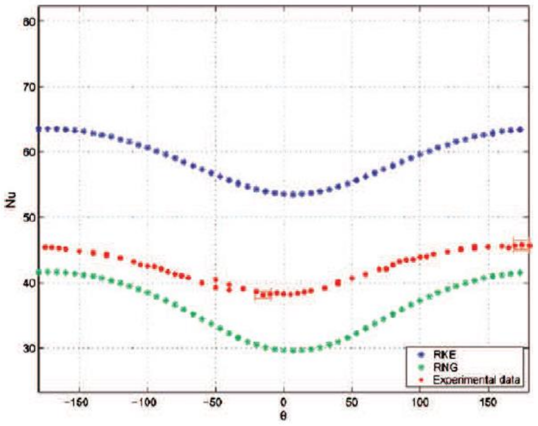

Figure 8: Comparison of Nusselt variation in cylindrical coordinates between experimental data and RANS models [58].

2.2 RANS Governing Equations

For a Newtonian fluid, for which shear stress in the fluid is proportional to the velocity gradient, the fundamental physical principles of fluid dynamics are described by the widely known Navier – Stokes equations, which describe the mass, momentum, and energy conservation along the flow domain. Considering that density and temperature variations with respect to a reference state as well as incompressibility along the flow, the **Boussinesq approximation** can be used, which simplifies the analysis. The equations then take the following form:

Mass conservation:

$$\frac{\partial u_i}{\partial x_i} = 0 \tag{5}$$

Momentum conservation:

$$\frac{\partial u_i}{\partial \mathrm{t}} + u_j \frac{\partial u_i}{\partial \mathrm{x}_j} = -\frac{1}{\rho_0}\frac{\partial p}{\partial x_i} + \nu \frac{\partial^2 u_i}{\partial \mathrm{x}_j\, \partial \mathrm{x}_j} - \beta_T \theta g \tag{6}$$

Energy conservation

$$\frac{\partial \theta}{\partial \mathrm{t}} + u_j \frac{\partial \theta}{\partial \mathrm{x}_j} = \kappa \frac{\partial^2 \theta}{\partial \mathrm{x}_j\, \partial \mathrm{x}_j} \tag{7}$$

where u_i is the velocity, p is the pressure and θ is the potential temperature at any instance. Additionally, ρ_0 is a constant reference density, ν is the kinematic viscosity, β_T is the thermal expansion coefficient and κ is the molecular heat diffusivity. In turbulent flows the main quantities of the flow, velocity, pressure and temperature can be decomposed into a mean and a fluctuating part. This method is known as *Reynolds decomposition*, which can be summed up as:

$$u_i = U_i + u_i' \tag{8}$$

$$p = P + p' \tag{9}$$

$$\theta = \varTheta + \theta' \tag{10}$$

In the equations (8), (9), (10) the mean quantities are represented by (U_i, P, Θ) and the fluctuated parts by (u_i', p', θ'). It needs to be noted that the mean quantities correspond to ensemble averages of an infinite number of turbulent flow realizations, $u_i^{(k)}$. This averaging operator is useful for theoretical applications due to a series of convenient mathematical properties and, using the velocity as an example, can be expressed as:

$$U_i = \bar{u}_i = \lim_{N\to\infty} \frac{1}{N} \sum_{k=1}^{N} u_i^{(k)} \tag{11}$$

The Reynolds-averaged Navier-Stokes (RANS) can then be derived by imposing the decomposed quantities on the original Navier-Stokes equations, in which $\frac{D}{Dt} = \frac{\partial}{\partial \mathrm{t}} + U_k \frac{\partial}{\partial x_k}$ is the material derivative along the mean flow.

Mass conservation:

$$\frac{\partial U_i}{\partial x_i} = 0 \tag{12}$$

Momentum conservation:

$$\frac{DU_i}{Dt} = -\frac{1}{\rho_0}\frac{\partial P}{\partial x_i} + \nu \frac{\partial^2 U_i}{\partial \mathrm{x}_j\, \partial \mathrm{x}_j} - \frac{\partial \overline{u'_i u'_j}}{\partial \mathrm{x}_j} - \beta_T \Theta g \tag{13}$$

Energy conservation

$$\frac{D\Theta}{Dt} = \kappa \frac{\partial^2 \Theta}{\partial \mathrm{x}_j\, \partial \mathrm{x}_j} - \frac{\partial \overline{u'_j \theta'}}{\partial \mathrm{x}_j} \tag{14}$$

Comparing the RANS to the original Navier-Stokes equations, one can notice the difference between them lies on the terms $\frac{\partial \overline{u'_i u'_j}}{\partial \mathrm{x}_j}$ and $\frac{\partial \overline{u'_j \theta'}}{\partial \mathrm{x}_j}$. These terms involve the non-linear quantities $\overline{u'_i u'_j}$ and $\overline{u'_j \theta'}$. The first quantity, known as the Reynolds-stress tensor, describes the additional flux of momentum due to the velocity fluctuations, while the second quantity describes the additional heat flux because of velocity-temperature fluctuations' interactions. These two quantities are unknown, leading to the so-called *turbulence closure problem,* requiring additional modelling for them.

2.3 Turbulence Models

One of the most widely used formulations for modelling Reynold stresses and turbulent heat flux is the eddy-viscosity approach, firstly introduced by Boussinsesq. According to this approach, ν_t, the eddy viscosity, acts as a coefficient of proportionality between the Reynolds shear stress and the mean strain rate. Similarly, an eddy diffusivity, κ_t, can be introduced to describe the turbulent heat flux as follows:

$$\overline{u'_i u'_j} = -\nu_t \left(\frac{\partial U_i}{\partial x_j} + \frac{\partial U_j}{\partial x_i} \right) + \frac{2}{3} k \delta_{ij} \tag{15}$$

$$\overline{u'_j \theta'} = -\kappa_t \frac{\partial \Theta}{\partial x_i} \tag{16}$$

where k is the turbulent kinetic energy. Using this approach, the closure problem now shifts to modelling $\nu_t = \frac{\mu_t}{\rho}$ and κ_t. In the following section two of the well-known models of this approach, used in the current work, are explained.

Menter Shear Stress Transport Turbulence Model

The first model used in this work is the “Standard Menter Shear Stress Transport” two-equation turbulence model, which will be referred to as *“k-ωSST”* model. It is a widely used turbulence model that is based on physical experiments and has been shaped over the past two decades, aiming to predict engineering solutions to common engineering problems [63]. Proposed by Menter [53], this model solves two separate transport equations for two independent turbulent quantities, the turbulent kinetic energy k and the turbulent specific dissipation rate ω:

$$\frac{\partial(\rho k)}{\partial \mathrm{t}} + \frac{\partial\left(\rho u_j k\right)}{\partial x_j} = P - \beta^* \rho \omega k + \frac{\partial}{\partial x_j}\left[(\mu + \sigma_k \mu_t)\frac{\partial k}{\partial x_j}\right] \tag{17}$$

$$\frac{\partial(\rho \omega)}{\partial \mathrm{t}} + \frac{\partial\left(\rho u_j \omega\right)}{\partial x_j} = \frac{\gamma}{\nu_t} P - \beta_1 \rho \omega^2 + \frac{\partial}{\partial x_j}\left[(\mu + \sigma_\omega \mu_t)\frac{\partial \omega}{\partial x_j}\right] + 2(1 - F_1)\frac{\rho \sigma_{\omega 2}}{\omega}\frac{\partial k}{\partial x_j}\frac{\partial \omega}{\partial x_j} \tag{18}$$

where

$$P = \tau_{ij}\frac{\partial u_i}{\partial x_j} \tag{19}$$

$$\tau_{ij} = \mu_t\left(2S_{ij} - \frac{2}{3}\frac{\partial u_k}{\partial x_k}\delta_{ij}\right) - \frac{2}{3}\rho k \delta_{ij} \tag{20}$$

$$S_{ij} = \frac{1}{2}\left(\frac{\partial u_i}{\partial x_j} + \frac{\partial u_j}{\partial x_i}\right) \tag{21}$$

The turbulent eddy viscosity is computed from:

$$\mu_t = \frac{\rho \alpha_1 k}{\max(\alpha_1 \omega, \Omega F_2)} \tag{22}$$

Each of the constants, φ, included in the model is a blend of an inner, denoted with 1, and an outer constant, denoted with 2, is expressed as:

$$\varphi = F_1 \varphi_1 + (1 - F_1)\varphi_2 \tag{23}$$

Additional functions of the model are given:

$$F_1 = \tanh(arg_1^4) \tag{24}$$

$$arg_1 = \min\left[max\left(\frac{\sqrt{k}}{\beta^* \omega d}, \frac{500\nu}{d^2 \omega}\right), \frac{4\rho \sigma_{\omega 2} k}{CD_{k\omega} d^2}\right] \tag{25}$$

$$F_2 = \tanh(arg_2^2) \tag{26}$$

$$arg_2 = max\left(2\frac{\sqrt{k}}{\beta^{*}\omega d}, \frac{500\nu}{d^2\omega}\right) \tag{27}$$

In the above equations, d is the distance from the field point to the nearest wall and $\Omega = \sqrt{2W_{ij}W_{ij}}$ is the vorticity magnitude, with

$$W_{ij} = \frac{1}{2}\left(\frac{\partial u_i}{\partial x_j} - \frac{\partial u_j}{\partial x_i}\right) \tag{28}$$

The constants of the model and their default values are included in Table 2.

Table 2: "k-ωSST" model constants.

Constant	Value
γ_1	$\frac{\beta_1}{\beta^{*}} - \frac{\sigma_{\omega 1}\kappa^2}{\sqrt{\beta^{*}}}$
γ_2	$\frac{\beta_2}{\beta^{*}} - \frac{\sigma_{\omega 2}\kappa^2}{\sqrt{\beta^{*}}}$
κ	0.41
σ_{k1}	0.85
σ_{k2}	1
$\sigma_{\omega 1}$	0.5
$\sigma_{\omega 2}$	0.856
β_1	0.075
β_2	0.0828
β^{*}	0.09
α_1	0.31

Spalart - Allmaras Turbulence Model

The second model used, is the one-equation turbulence model proposed by Spalart and Allmaras [52] and will be referred to as "*SA*" model. According to this model, a solution to the turbulence viscosity ν_t is obtain by solving one equation, which refers to a modified turbulence viscosity $\tilde{\nu}$, as follows:

$$\frac{\partial\tilde{\nu}}{\partial \mathrm{t}} + u_j\frac{\partial\tilde{\nu}}{\partial x_j} = c_{b1}(1 - f_{t2})\tilde{S}\tilde{\nu} - \left[c_{w1}f_w - \frac{c_{b1}}{\kappa^2}f_{t2}\right]\left(\frac{\tilde{\nu}}{d}\right)^2 + \frac{1}{\sigma}\left[\frac{\partial}{\partial x_j}\left((\nu + \tilde{\nu})\frac{\partial\tilde{\nu}}{\partial x_j}\right) + c_{b2}\frac{\partial\tilde{\nu}}{\partial x_\iota}\frac{\partial\tilde{\nu}}{\partial x_\iota}\right] \tag{29}$$

The turbulent eddy viscosity is computed as:

$$\mu_t = \rho\tilde{\nu}f_{u1} \tag{30}$$

$$f_{u1} = \frac{x^3}{x^3 + {c_{u1}}^3} \tag{31}$$

$$x = \frac{\tilde{\nu}}{\nu} \tag{32}$$

Additional definitions are given:

$$\tilde{S} = \Omega + \frac{\tilde{\nu}}{\kappa^2 d^2} f_{u2} \tag{33}$$

$$f_{u2} = 1 - \frac{x}{1 + x f_{u1}} \tag{34}$$

$$f_w = g \left[\frac{1 + c_{w3}^6}{g^6 + c_{w3}^6} \right]^{\frac{1}{6}} \tag{35}$$

$$g = r + c_{w2}(r^6 - r) \tag{36}$$

$$r = \min \left[\frac{\tilde{\nu}}{\tilde{S} \kappa^2 d^2}, 10 \right] \tag{37}$$

$$f_{t2} = c_{t3} \exp(-c_{t4} x^2) \tag{38}$$

In the above equations, d is the distance from the field point to the nearest wall and $\Omega = \sqrt{2 W_{ij} W_{ij}}$ is the vorticity magnitude, with W_{ij} given by equation (28). The constants of the model and their default values are included in Table 3.

Table 3: "SA" model constants.

Constant	**Value**
c_{w1}	$\frac{c_{b1}}{\kappa^2} + \frac{1 + c_{b2}}{\sigma}$
c_{b1}	0.1355
c_{b2}	0.622
σ	2/3
κ	0.41
c_{w2}	0.3
c_{w3}	2
c_{u1}	7.1
c_{t3}	1.2
c_{t4}	0.5

2.4 OpenFOAM-Thermophysical Solvers

Simulating mixed convection flows through artificially roughened pipes is the objective of the current work. “OpenFOAM” has been the software of choice, since it is one of the most used free, open-source software developed. In this chapter details concerning the thermophysical modelling of the cases are included.

Solvers

In OpenFOAM there is no generic solver applicable to all cases. On the contrary, the user is required to make a choice between a set of available solvers, depending on the nature of the problem. In our case, the most suitable category of solvers is the one presented as solvers for “Heat transfer and buoyancy-driven flows”, in the OpenFOAM User Guide [59].

The first application solver that was used is the **buoyantBoussinesqPimpleFoam**, a solver developed intended for cases of transient, buoyant, turbulent flows of incompressible fluids. In the most generic form, the mass and momentum conservation equations solved by the solver are [60]:

$$\frac{\partial \rho}{\partial \mathrm{t}} + \nabla \cdot (\rho \boldsymbol{u}) = 0 \tag{39}$$

$$\frac{\partial (\rho \boldsymbol{u})}{\partial \mathrm{t}} + \nabla \cdot (\rho \boldsymbol{u}\boldsymbol{u}) = -\nabla p + \rho \boldsymbol{g} + \nabla \cdot \left(2\mu_{eff} D(\boldsymbol{u})\right) - \nabla \left(\frac{2}{3}\mu_{eff}(\nabla \cdot \boldsymbol{u})\right) \tag{40}$$

where $\boldsymbol{u}$ represents the velocity field, p the pressure field, ρ the density field and $\boldsymbol{g}$ is the gravitational acceleration**.** The sum of the molecular and the turbulent viscosity is represented by the effective viscosity μ_{eff}, while the rate of strain tensor is described by

$$D(\boldsymbol{u}) = \frac{1}{2}(\nabla \boldsymbol{u} + (\nabla \boldsymbol{u})^T) \tag{41}$$

When using this solver, the **Boussinesq approximation** is used. According to it when the variation of density is small, one can treat the density as a constant and treat it as a variable only in the gravitational term “$\rho \boldsymbol{g}$”. This is an assumption that is made and will be valid throughout this work. The approximation can be implemented by expressing density as a linear function of temperature, T:

$$\rho \approx \rho_0[1 - \beta(T - T_0)] \tag{42}$$

where β is the volumetric thermal expansion coefficient and is treated as a constant. Additionally, two more constants need to be defined, ρ_0 and T_0, representing a reference density and a reference temperature respectively. After defining a new variable, $p_{rgh} = (p - \rho \boldsymbol{g} \cdot \boldsymbol{r})/\rho_0$, with $\boldsymbol{r}$ describing the position vector, one can derive the final momentum conservation equation:

$$\frac{\partial \boldsymbol{u}}{\partial \mathrm{t}} + \nabla \cdot (\boldsymbol{u}\boldsymbol{u}) = -\nabla p_{rgh} - (\boldsymbol{g} \cdot \boldsymbol{r})\nabla \left(\frac{\rho}{\rho_0}\right) + \nabla \cdot \left(2\nu_{eff} D(\boldsymbol{u})\right) \tag{43}$$

After experimenting with the **buoyantBoussinesqPimpleFoam** solver it became clear that it was not the best choice, as it led to instabilities in the flow domain for the variety of thermophysical properties and boundary conditions tested, and it was switched to the **buoyantPimpleFoam,** which is a solver available in OpenFOAM, suitable for transient, buoyant, turbulent, compressible flows. The Boussinesq approximation in this solver can be implemented the simulation in the **"thermophysicalProperties"** dictionary included in the **"constant"** folder of the simulation directory. In this file, the thermophysical model is defined by specifying the following:

Type: ***heRhoThermo***
This is a general thermophysical model calculation based on enthalpy h or internal energy e, and density ρ.

Mixture: *pureMixture*
This is a general thermophysical model calculation for passive gas mixtures.

Transport: *const*
Assumes a constant dynamic viscosity μ and Prandtl number Pr that need to be specified.

Thermo: *hConst*
Assumes a constant specific heat c_p model with evaluation of enthalpy h and entropy s.

EquationOfState: *Boussinesq*
The Boussinesq approximation is applied by defining ρ_0, T_0 and β.

Specie: *specie*
The molecular weight of the working fluid is specified.

Energy: *sensibleEnthalpy*
The energy equation is solved in enthalpy terms, while heat of formation is not included, leading to the energy equation:

$$\frac{\partial(\rho h)}{\partial \mathrm{t}} + \nabla \cdot (\rho \boldsymbol{u} h) + \frac{\partial(\rho K)}{\partial \mathrm{t}} + \nabla \cdot (\rho \boldsymbol{u} K) - \frac{\partial p}{\partial \mathrm{t}} = \nabla \cdot \left(\alpha_{eff} \nabla h\right) + \rho \boldsymbol{u} \cdot \boldsymbol{g} \qquad (44)$$

Where α_{eff} is the sum of laminar and turbulent thermal diffusivities. $K \equiv |\boldsymbol{u}^2|/2$ is the kinetic energy per unit mass and the enthalpy per unit mass, $h \equiv e + p/\rho$, is the sum of the internal energy per unit mass, e, and the kinematic pressure.It needs to be noted that the variable p_{rgh} is used likewise for the solution of the pressure field and the equations (37), (38) explained above are applicable for the **buoyantPimpleFoam** solver as well [61].

Additional dictionaries required in the **"constant"** folder are the **"g"** dictionary, where the value of the gravitational acceleration is specified, as well as the **"turbulenceProperties**" dictionary, where turbulence is set on by specifying the type of simulation, in our case RANS modeling, and turbulence model.

2.5 OpenFOAM-Numerical Schemes

The **“system”** directory includes the **“fvSchemes”** dictionary, which sets the numerical schemes for different terms in the equations that need to be solved for each simulation. In this dictionary, the following are specified:

Time Schemes

Specified under the “**ddtSchemes**” sub-dictionary, it is responsible for first time derivative $(\partial / \partial t)$ terms. In our case, the Eulerian time scheme was chosen for all simulations, which is a first order, bounded, implicit scheme. This was done using the keyword **Euler.**

Gradient Schemes

Gradient terms, (∇), are discretized according to the scheme specified. In our case the standard finite volume discretisation of Gaussian integration was chosen. Since the particular scheme requires interpolation of values from cell centres to face centres, the choice of interpolation scheme needs to be chosen as well. In our simulations a linear interpolation scheme was chosen, using the keyword **Gauss linear**.

Divergence Schemes

In this sub-dictionary the Gauss scheme is the only choice of discretisation for divergence $(\nabla \cdot)$ terms, however an interpolation scheme needs to be specified as well. The selection is required for each field. The syntax for an entry required by OpenFOAM for the velocity field U is “div(phi,U)” followed by the scheme of choice, where “phi” refers to the flux $\varphi = \rho U$. In the simulations of this work, **Gauss upwind** was the selection of choice. “Upwind” is a first-order bounded divergence scheme in which the up-stream variables are used to calculate the derivatives in the flow field.

Laplacian Schemes

This sub-dictionary is responsible for the Laplacian (∇^2) terms. Entries require the discretisation scheme, followed by an interpolation scheme for the diffusion coefficient and a surface normal gradient scheme. In our case **Gauss linear corrected** was the entry of choice. The keyword “corrected” refers to an explicit non-orthogonal correction that can be added in cases where the vector connecting cell centres is non-orthogonal, meaning it deviates from the orthogonal scheme.

Surface Normal Gradient Schemes

The component of each gradient that is normal to a cell face is solved under schemes specified in this sub-dictionary. Required as an additional entry in the Laplacian Schemes shown above, the scheme of selection in our simulations was the “corrected” scheme, which refers to an explicit non-orthogonal correction.

2.6 OpenFOAM-Solution

The equation solvers, algorithms and tolerances are specified in the **“fvSolution”** dictionary of the “system” directory. The term “solvers” refers to the **“linear solvers”** that are used for each discretised equation, opposed to the **“application solvers”** explained earlier, which are responsible for describing the set of equations and algorithms to be solved. In the following section, the sub-dictionaries included in fvSolution are explained:

Solvers

This is the main sub-dictionary of this directory, where the linear solver used for each discretised equation needs to be specified. An entry is needed for every equation that is to be solved. Examples of the entries required are shown in Figure 9. The model of use in the example is "*k-ωSST*".

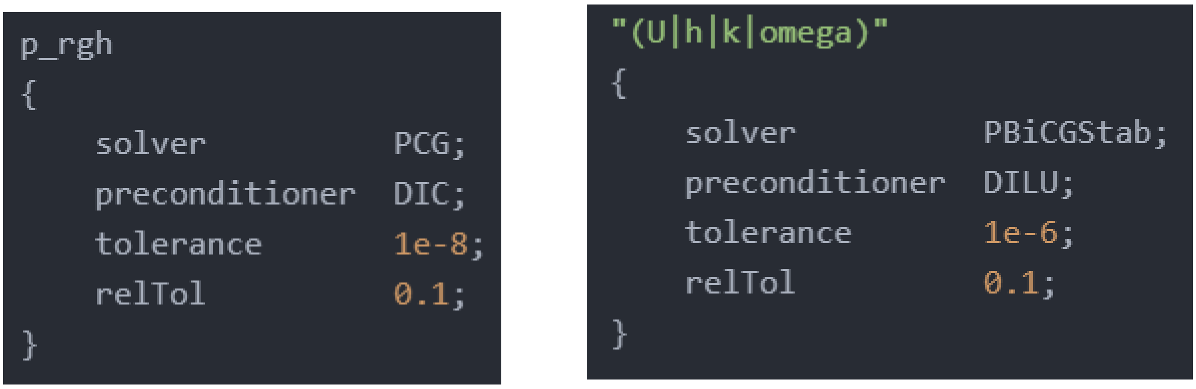

```
p_rgh
{
    solver          PCG;
    preconditioner  DIC;
    tolerance       1e-8;
    relTol          0.1;
}
```

```
"(U|h|k|omega)"
{
    solver          PBiCGStab;
    preconditioner  DILU;
    tolerance       1e-6;
    relTol          0.1;
}
```

Figure 9: Linear solver selection.

The first entry includes the selection of the linear solver, which is the **Preconditioned (bi-)conjugate gradient (PCG)** for the symmetric matrices and the **Stabilized Preconditioned (bi-) conjugate gradient (PBiCGStab)** for the cases of velocity, enthalpy, turbulent kinetic energy, and turbulent specific dissipation rate, where asymmetric matrices are found.

Additionally, as seen by the second entry, the preconditioner needs to be specified. Two different preconditioners are chosen, the **Diagonal incomplete-Cholesky (DIC)**, which is suitable for symmetric matrices, and the **Diagonal incomplete-LU (DILU)**, which is suitable for asymmetric matrices.

After each solver iteration, the residuals are evaluated, and compared to the solver tolerance specified by the user. The smaller the tolerance, the more accurate the solution will be, since it represents the acceptable difference between the left- and right-hand side of each equation solved. Two tolerances are required to be specified next the keywords **"tolerance"** and **"relTol"**. The solver stops iterating when the residual falls below the solver tolerance specified by the keyword **"tolerance"** or when the ratio of current to the initial residuals falls below the solver relative tolerance, expressed by the keyword **"relTol".**

Relaxation – Algorithm Control

Two additional sub-dictionaries are available, a sub-dictionary for under-relaxation control, a technique used for improving computational stability by specifying "**relaxation factors"** for each equation, and one for algorithm control, in which the algorithm responsible for solving the velocity-pressure field is chosen, in our case the **"PIMPLE"** algorithm. **PIMPLE** is a combination of the two other algorithms available for velocity-pressure decoupling, the **"PISO"** (Pressure Implicit with Splitting of Operator) and the **"SIMPLE"** (Semi-Implicit Method for Pressure-Linked Equations) algorithms. **PIMPLE** and **PISO** are used for transient cases, while **SIMPLE** is suitable for steady-state cases. Moreover, the number of outer correctors **"nOuterCorrectors"** can be specified, indicating how many times the system of equations is performed before moving to the next time step, as well as the number of inner correctors **"nCorrectors"**, indicating the number of times the pressure is corrected within an iteration. Finally, under the keyword **“nNonOrthogonalCorrectors”,** a correction for the mesh non-orthogonality can be used.

2.7 OpenFOAM-Mesh Generation

After the geometry of interest is defined, it is necessary that a grid is created so that the domain is separated into finite volume elements on which the numerical calculations are applied. There are certain requirements for the density of the grid, or how “fine” a grid should be, so that the simulations results are accurate enough, especially in turbulent cases. According to the boundary layer theory, in a case of a flow over a wall, the first sublayer adjacent to the wall is the **“inner layer”** as shown in Figure 10, in which viscous shear forces dominate. Accurately capturing fluid motions within the viscous sublayer is of great importance, since the wall is responsible for the generation of vorticity in the flow.

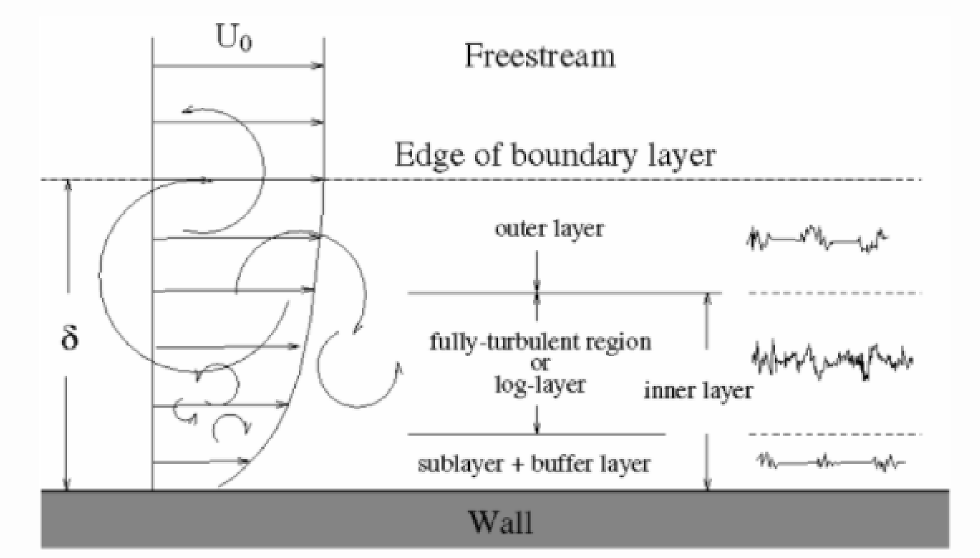

Figure 10: [62] Turbulent boundary layer structure.

The behaviour of a flow near a wall is a complicated phenomenon and capturing it in turbulent CFD modelling is a problem that has led to the formulation of a dimensionless quantity, y^+, which describes the distance from the wall measured in terms of viscous lengths, given by:

$$y^+ = \frac{\Delta y u_T}{\nu} \tag{45}$$

where ν is the kinematic viscosity, Δy is the distance from the wall and u_T is the friction or shear velocity, given by:

$$u_T = \sqrt{\frac{\tau_w}{\rho}} \tag{46}$$

where τ_w is the wall shear stress and ρ the density of the fluid. If we use a dimensionless form of the velocity, shown in equation (47), the velocity profiles within the boundary layer can be seen in Figure 11, as described by the “Law of the Wall”.

$$u^+ = \frac{u}{u_T} \tag{47}$$

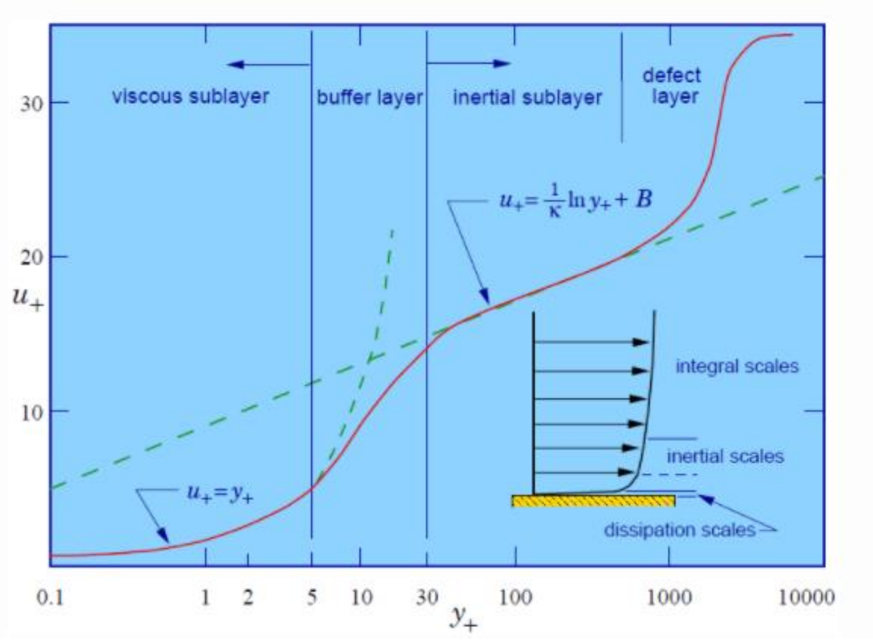

Figure 11: [62] Velocity profiles in a turbulent wall flow.

As seen from Figure 11, for $y^+ < 5$, there is a linear variation of the velocity versus the distance from the wall and a logarithmic variation for $y^+ > 30$. In the area $5 < y^+ < 30$ velocity neither the linear nor the logarithmic law stands, while the two equations intersect at $y^+ = 11$. In the buffer layer, for $y^+ < 11$ the linear approximation is more accurate and for $y^+ > 11$ the logarithmic.

In OpenFOAM, an accurate inner layer representation can be achieved by using known **"wall functions"** provided by the software, which are basically empirical correlations describing near-wall flow conditions. The use of such wall functions requires a mesh fine enough that the height of the first cell from the wall satisfies $y^+ = 30$. Such a method saves computational time. However, it lacks accuracy. To ensure higher accuracy, a finer mesh approach has been followed, in which the target value is $y^+ = 1$. This way, the whole boundary layer is resolved by the turbulent models of choice, *"k-ωSST"* and *"SA",* which are designed for this purpose. To calculate the height of the first cell Δy, one can substitute $y^+ = 1$ in equation (45) and estimate the shear velocity using the following formulas:

$$\tau_w = \frac{1}{2} C_f \rho U_0^2 \tag{48}$$

where U_0 is the inlet velocity and C_f the skin friction coefficient, estimated by the empirical correlations (49) and (50), for internal and external flows respectively:

$$C_f = 0.079 Re^{-0.25} \tag{49}$$

$$C_f = 0.058 Re^{-0.2} \tag{50}$$

Additionally, to save computational costs, the **"simple grading"** OpenFOAM utility has been used, which sets an expansion ratio of the cells along the height of the domain, since there is no need for such a dense grid away from the wall. For the density of the grid along the direction of the flow recommendations from CFD forums [63] have been followed, indicating that the same calculations can be carried out after setting a goal dimensionless distance equal to 50. More detailed information about meshing in the simulations conducted will be given in Chapter 4.

3. Model Validation

3.1 Laminar Case

As a first step to getting acquainted with modelling mixed convection cases in OpenFoam, the validation of a laminar flow case was performed. Desrayaud's numerical work [64] was chosen for this task, since it depicts a laminar, two-dimensional mixed convection flow of air in a vertical parallel – plate channel of width D, heated at a constant wall temperature T_w, as shown in Figure 12. A uniform inlet velocity profile with a magnitude of u_0 is chosen at an inlet temperature T_0.

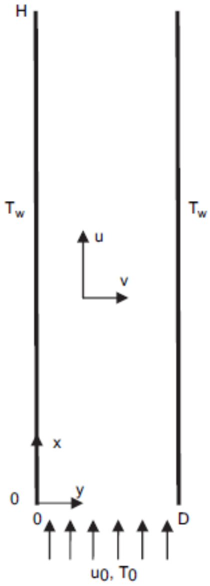

Figure 12: [64] Calculation domain and dimensional coordinate system of the parallel plate.

The target of this validation was to produce streamwise axial velocity profiles and temperature distributions as a function of position along the domain, for the following conditions:

Table 4: Constants in Desrayaud's work.

Constant	**Symbol**	**Value**
Channel width	$D\ (m)$	0.03
Channel height	$H\ (m)$	1.5
Gravitational acceleration	$g\ (ms^{-2})$	9.81
Thermal expansion coefficient	$\beta\ (K^{-1})$	3.23 x 10^{-3}
Wall temperature	$T_w\ (K)$	333
Inlet temperature	$T_0\ (K)$	283
Kinematic viscosity	$v\ (m^2s^{-1})$	1.64 x 10^{-5}
Inlet velocity	$u_0\ (ms^{-1})$	0.082
Reynolds number	Re	300.7
Grashof number	Gr	159044

where

$$Re = \frac{2Du_0}{v} \tag{51}$$

$$Gr = \frac{g\beta(T_w - T_0)D^3}{v} \tag{52}$$

For the simulation of Desrayaud's case, the buoyantBoussinesqPimpleFoam solver was used, assuming the Boussinesq approximation to be valid. The simulation was performed under a 200 x 42 grid, which is indicated as sufficient for accurate results [64]. The boundary conditions used are shown in Table 5.

Table 5: Simulation boundary conditions.

Boundary	**Velocity (u)**	**Pressure (p)**	**Hydrostatic Pressure (p_rgh)**	**Temperature (T)**
Inlet	fixedValue (0 0.082 0)	calculated	fixedFluxPressure	fixedValue (283)
Outlet	zeroGradient	fixedValue (0)	prghPressure	zeroGradient
Walls	no slip	calculated	fixedFluxPressure	fixedValue (333)

Desrayaud's temperature distributions as well as the velocity profiles are compared to those produced by Paraview, the post-processor used for OpenFoam results, in Figures 13 and 14. Different curves refer to different distances along the channel, each represented by a number following the multiplication sign. The curve represented by "x6'' represents the profile at a distance equal to six times the channel width measured from the inlet. The same logic applies to the rest of the profiles.

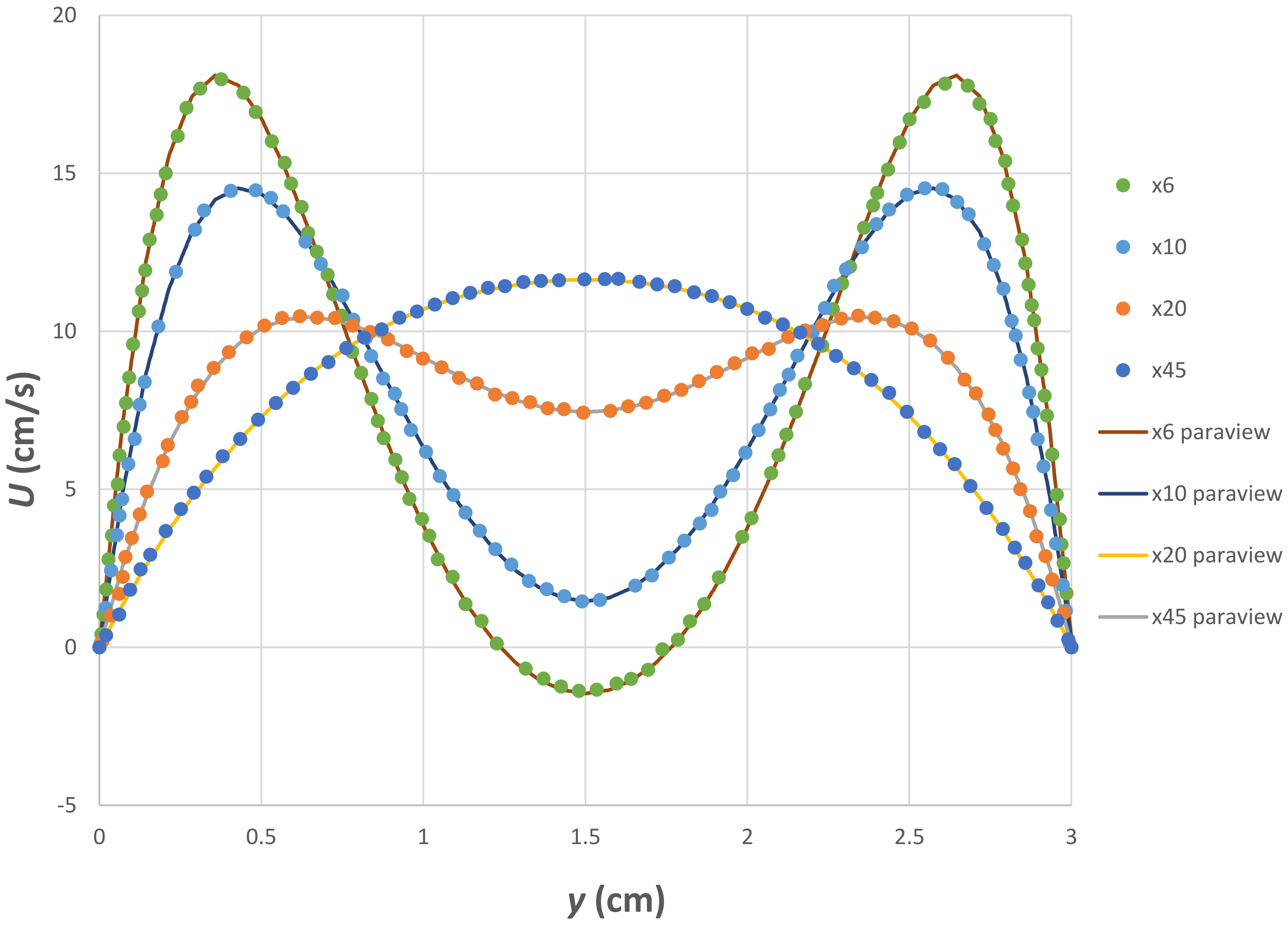

Figure 13: Laminar case velocity profiles' validation.

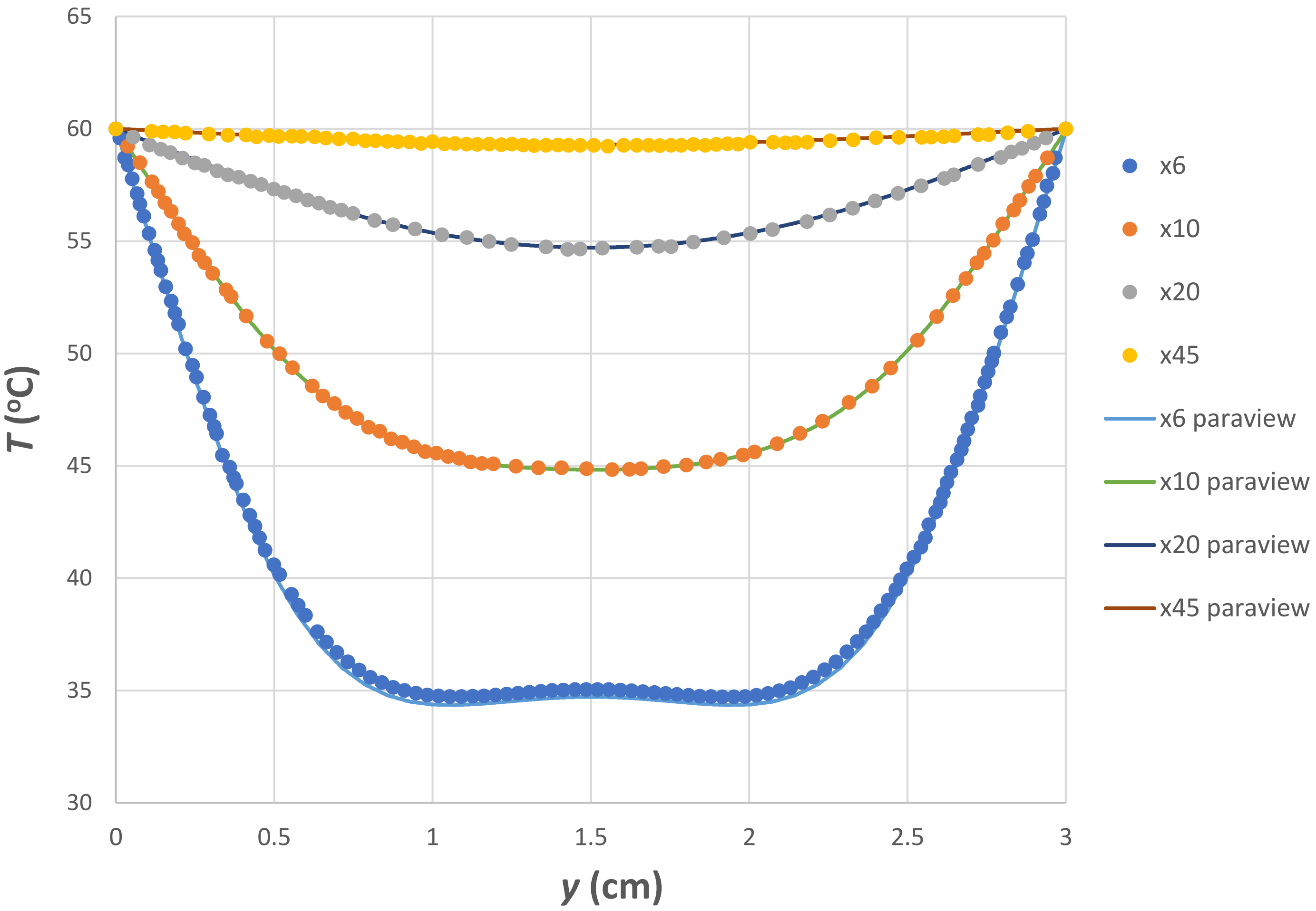

Figure 14: Laminar case temperature distribution validation.

Figures 13, 14 indicate that there is an almost perfect agreement between Desrayaud's results with the ones generated by OpenFoam.

3.2 Turbulent Case

The last step before performing the final simulations was validating a mixed convection turbulent case. Shehata's [65] experimental work on upward air flow within a vertical circular tube for different heating rates was chosen. The goal was reproducing mean temperature and mean axial velocity field variations at different distances along the tube.

Heating Rates - Velocities

Three different cases were investigated, labelled by Shehata as **"Run 618"**, **"Run 635"** and **"Run 445"** represented by different heating rates and inlet Reynolds numbers as shown in Table 6. Heating rates in this work are represented by the dimensionless heat flux q_i^+ based on inlet conditions, given by the formula:

$$q_i^+ = \frac{q_w}{GC_{p,in}T_{in}} \tag{53}$$

where q_w is the wall heat flux, G is the mean mass flux, $C_{p,in}$ the specific heat at constant pressure at the inlet and T_{in} is the inlet temperature.

Table 6: [65] Heating rates and Reynolds number values.

Case Label	Reynolds Number (inlet)	q_i^+
Run 618	6080	0.0018
Run 635	6050	0.0035
Run 445	4260	0.0045

Assuming a kinematic viscosity $\nu = 1.48 \times 10^{-5}(\frac{m^2}{s})$, inlet temperature $T_{in} = 290\ (K)$ and inlet specific heat capacity $C_{p,in} = 1000\ (\frac{J}{kgK})$ the inlet velocities and heating rates for the simulations were calculated. A diameter $D = 0.0274\ (m)$ and a heated length of 32 diameters resulting into $L = 876.8\ (m)$ were used for the calculations and simulations. The calculated inlet velocities as well as the wall heat fluxes are shown in Table 7.

Table 7: Calculated inlet velocities and wall heat fluxes used for the validation.

Case Label	Inlet velocity (m/s)	Wall heat flux (W/m^2)
Run 618	3.28	2100
Run 635	3.267	4063
Run 445	2.3	3678

Geometry - Mesh

Since the problem is axisymmetric, the tube was simulated using a two-dimensional wedge geometry for saving computational time. The front and side view of the geometry and mesh is shown in Figure 15. As seen from the figure, assuming the flow is in the z-direction, the grid consists of only one cell at the x-direction, making the problem two-dimensional. OpenFoam has a built in ‘’wedge’’ boundary condition, which can be imposed at the sides of the geometry and is considered a standard method for solving cylindrical problems.

For the mesh construction a dimensionless wall distance $y^+ = 1$ was chosen, so that the region adjacent to the wall, the viscous sublayer, can be resolved accurately without the use of wall functions. The height of the first cell close to the wall at the y-direction, Δy_1, can be calculated as explained by equations (43) – (47). The resulting mesh is summarized in Table 8.

Table 8: Meshing details.

Variable	Name	Value
Number of cells in z-direction	$N_{cells,z}$	300
Number of cells in y-direction	$N_{cells,y}$	60
Cell to cell expansion ratio (starting from the axis)	r	0.961
Total number of cells	N_{cells}	18000

For the calculations the inlet density was assumed to be $\rho = 1.225\ kg/m^3$ and the dynamic viscosity $\mu = 1.81 \times 10^{-5} kg/ms$.

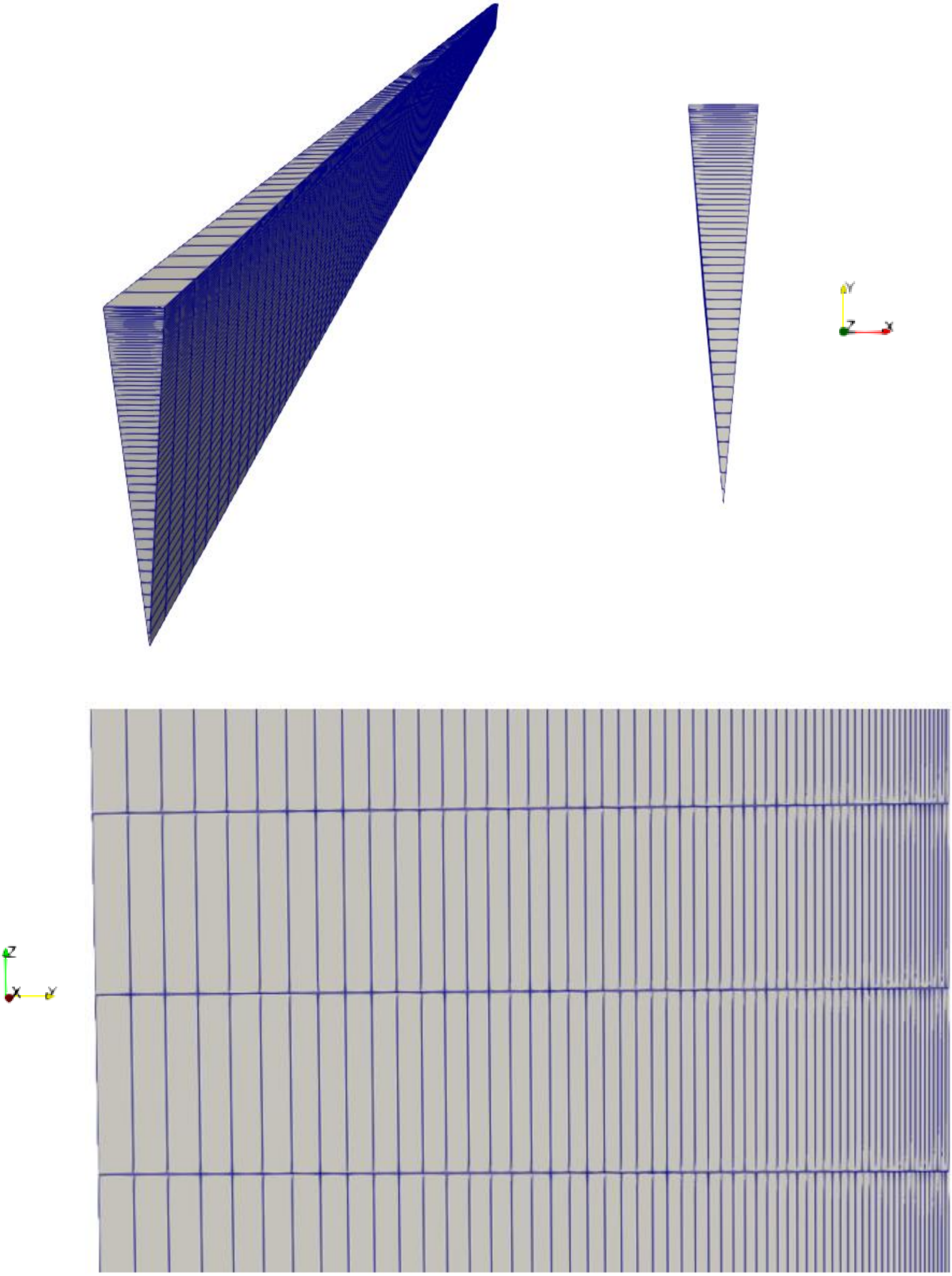

Figure 15: Geometry and mesh representation.

Turbulence model

For the validation of the turbulent case the *"k-ωSST"* turbulence model was used. The "**buoyantBoussinesqPimpleFoam**" solver was substituted by the "**buoyantPimpleFoam**" solver, since it showed better behaviour in turbulent domains, accompanied by the Boussinesq equation of state. The values used in equation (40) for the representation of the Boussinesq equation of state are shown in Table 9. The values are chosen for the average temperature noted in Shehata's results and obtained by online properties' tables [66].

Table 9: Boussinesq equation of state constants.

Variable	Name	Value
Thermal expansion coefficient	$\beta\ (K^{-1})$	0.002
Reference temperature	$T_0\ (K)$	545
Reference density	$\rho_0\ (kg/m^3)$	0.832

The boundary conditions used for **Run 618** is shown in Table 10. It must be noted that a wall function is used as a boundary condition at the wall for the "**omega**" file. Even though the mesh is fine enough, not justifying the use of a wall function, suggestions from CFD researchers [63] indicate that using one is helpful in obtaining accurate "omega" values, when using this model.

Table 10: Boundary conditions used in the simulations.

Label	**Boundary**	**U**	**p**	**prgh**	**T**	**k**	**omega**
Run 618	Wall	No Slip	calculated	Fixed flux pressure	Fixed gradient	Fixed value	Omega wall function
	Inlet	Fixed value	calculated	Fixed flux pressure	Fixed value	Fixed value	Fixed value
	Outlet	Zero gradient	calculated	Prgh pressure	Zero gradient	Zero gradient	Zero gradient

The boundary conditions presented in Table 10 apply to Runs 445 and 635 as well. The difference between each run lies in the inlet velocity "Fixed value" and wall temperature "Fixed gradient" entries. For each run, different values were selected based on the data shown in Table 7.

An additional entry is required before running the simulations, referring to initializing the turbulent kinetic energy, k, field and the turbulent specific dissipation rate, ω, field. These present a value for OpenFOAM to initialize the *"k-ωSST"* field calculation, and an accurate estimation can make the simulation less costly and more stable. The estimations were based on the following formulas:

$$I = 0.16Re^{-\frac{1}{8}} \tag{54}$$

$$k = 3/2\left(Iu_{ref}\right)^2 \tag{55}$$

$$\omega = k^{0.5}/C_\mu^{0.25}D \tag{56}$$

Where I is the turbulent intensity, C_μ a constant taken equal to 0.09 and u_{ref} is the reference velocity, taken as the inlet velocity in this case.

Results, shown in Figures 16 – 18, consist of mean axial velocity profile and temperature distribution comparisons at different distances along the tube. Results are shown against $y = R - r$, with R referring to the pipe radius and r referring to the radial position of interest. Temperature profiles are compared with the inlet temperature, while axial velocities are compared to the bulk velocity, calculated at each cross section as:

$$u_b = \frac{\int \rho u dA}{\int \rho dA} \tag{57}$$

The results presented show a satisfying level of agreement between Shehata's experimental results even though there are some differences, especially in the temperature profiles of Run 445. However, considering the high temperature differences found in Shehata's experiments, we should expect some variance due to the Boussinesq equation of state assumption, which produces inaccuracies at higher density differences. Additionally, an entrance region of non-heated pipe is present in the experiments by Shehata for flow development, which is not present in the simulations. Taking into consideration expected inaccuracies when performing RANS simulations, the validation can be characterized as successful, an important step in testing turbulence models as well as gaining experience in using OpenFOAM. A full list of the validation's figures is included in the Appendix.

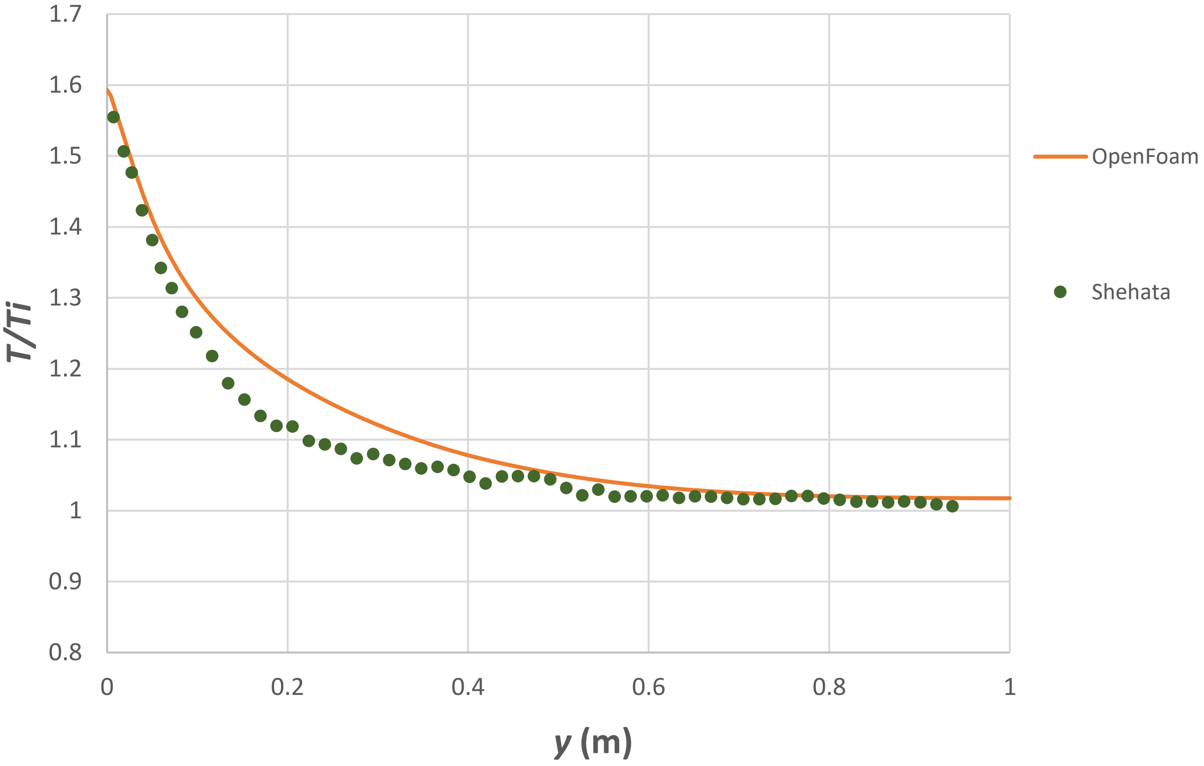

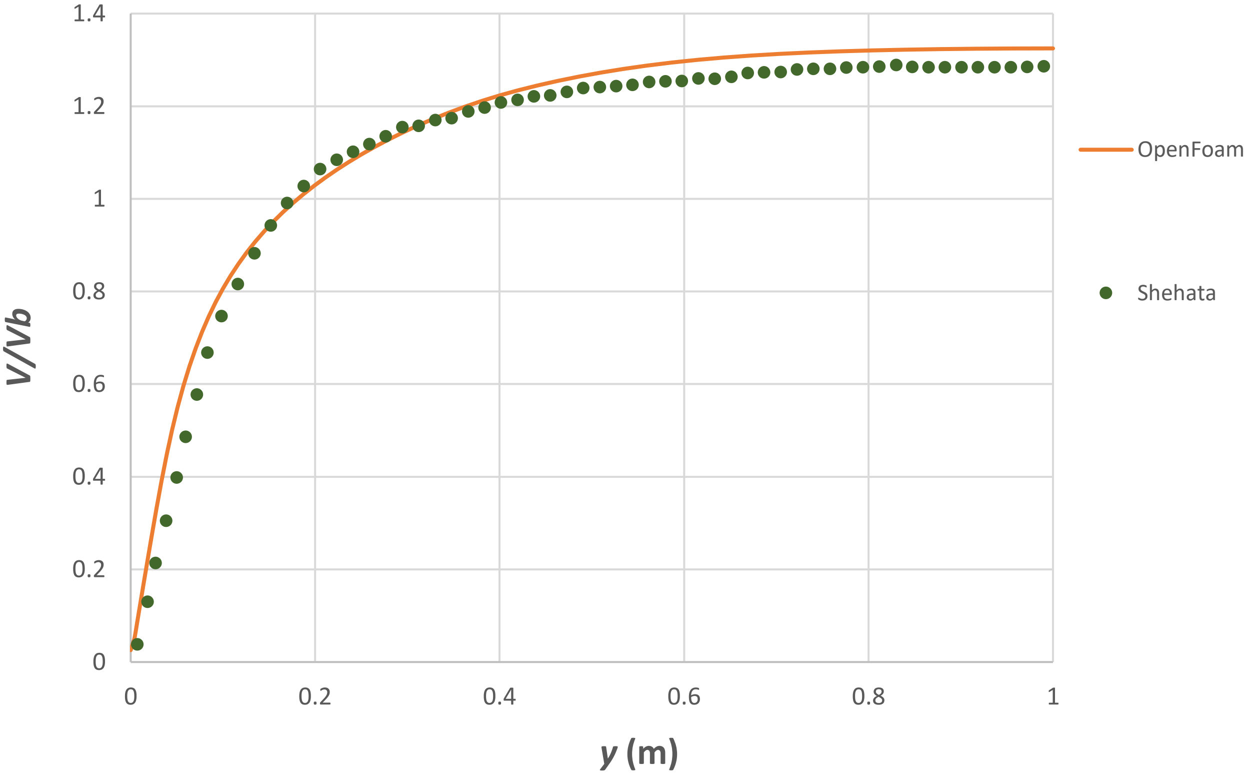

Figure 16: "Run 618" validation. Top: Temperature distribution / Bottom: Velocity profiles

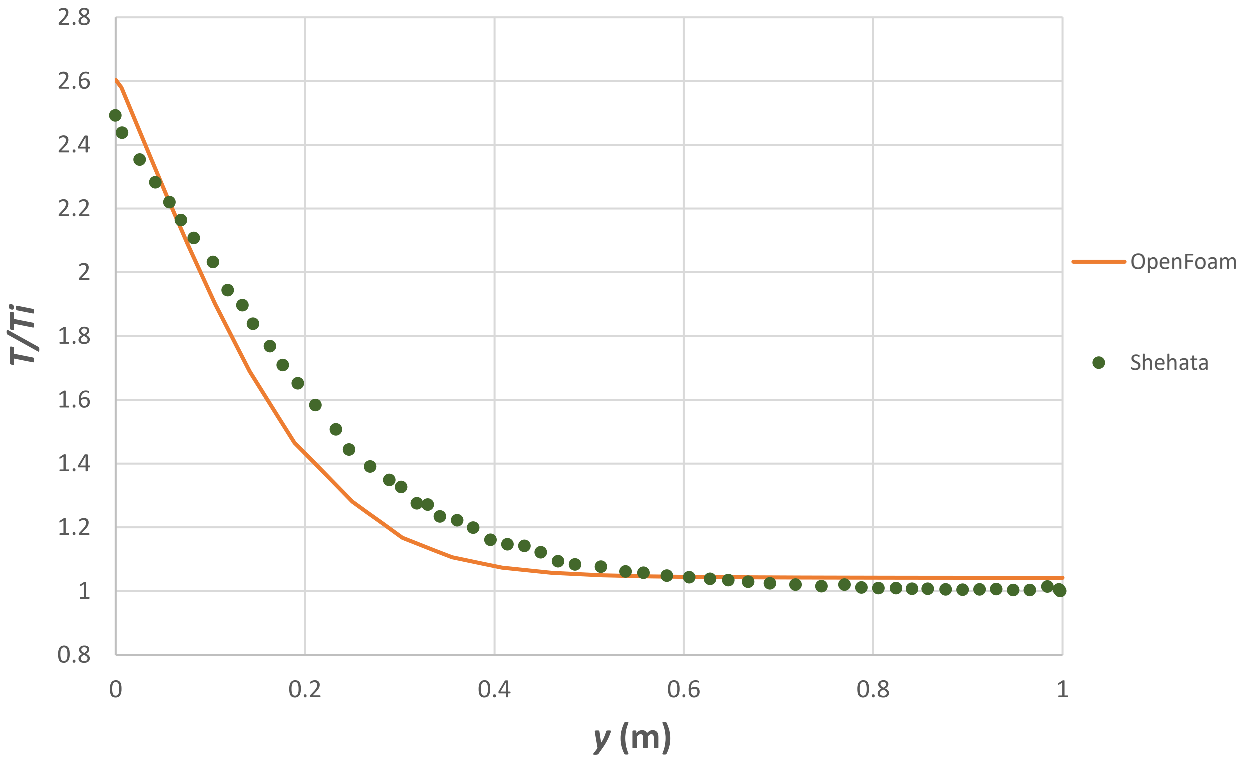

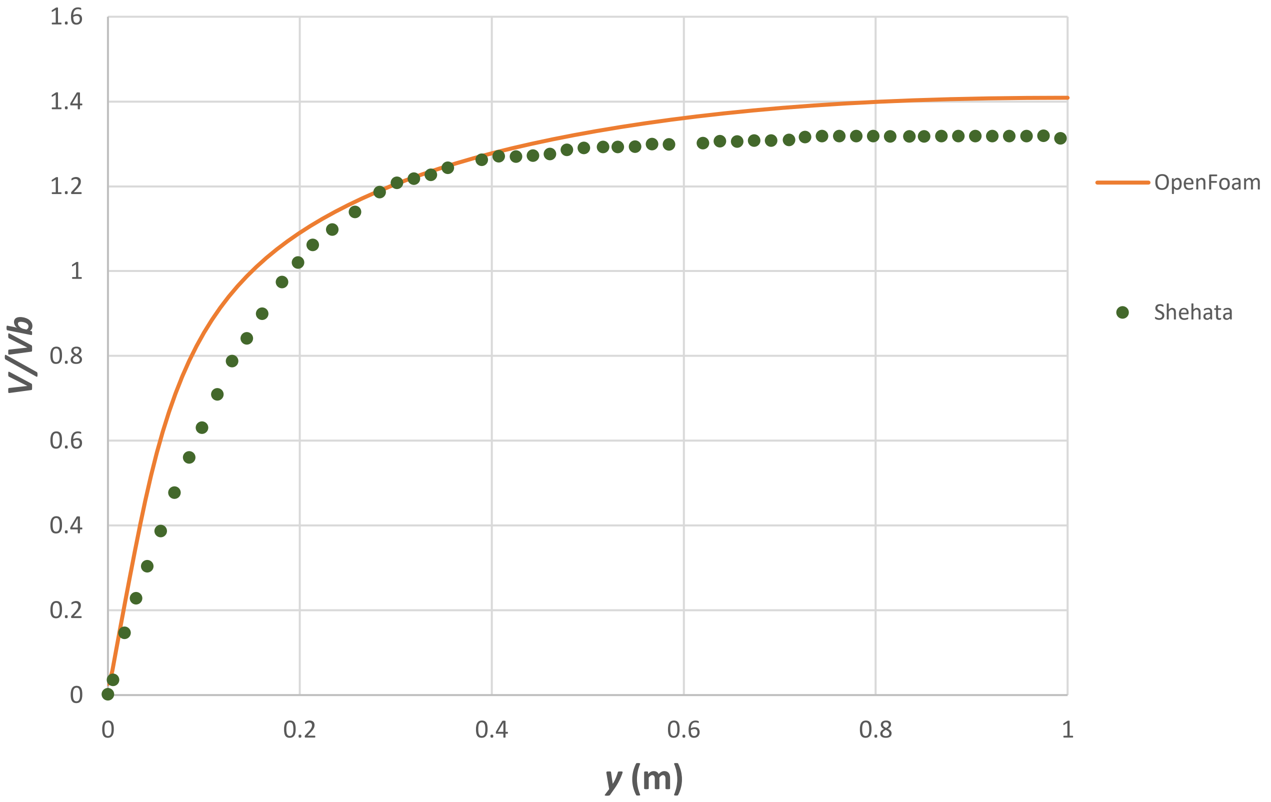

Figure 17: "Run 635" validation. Top: Temperature distribution / Bottom: Velocity profiles

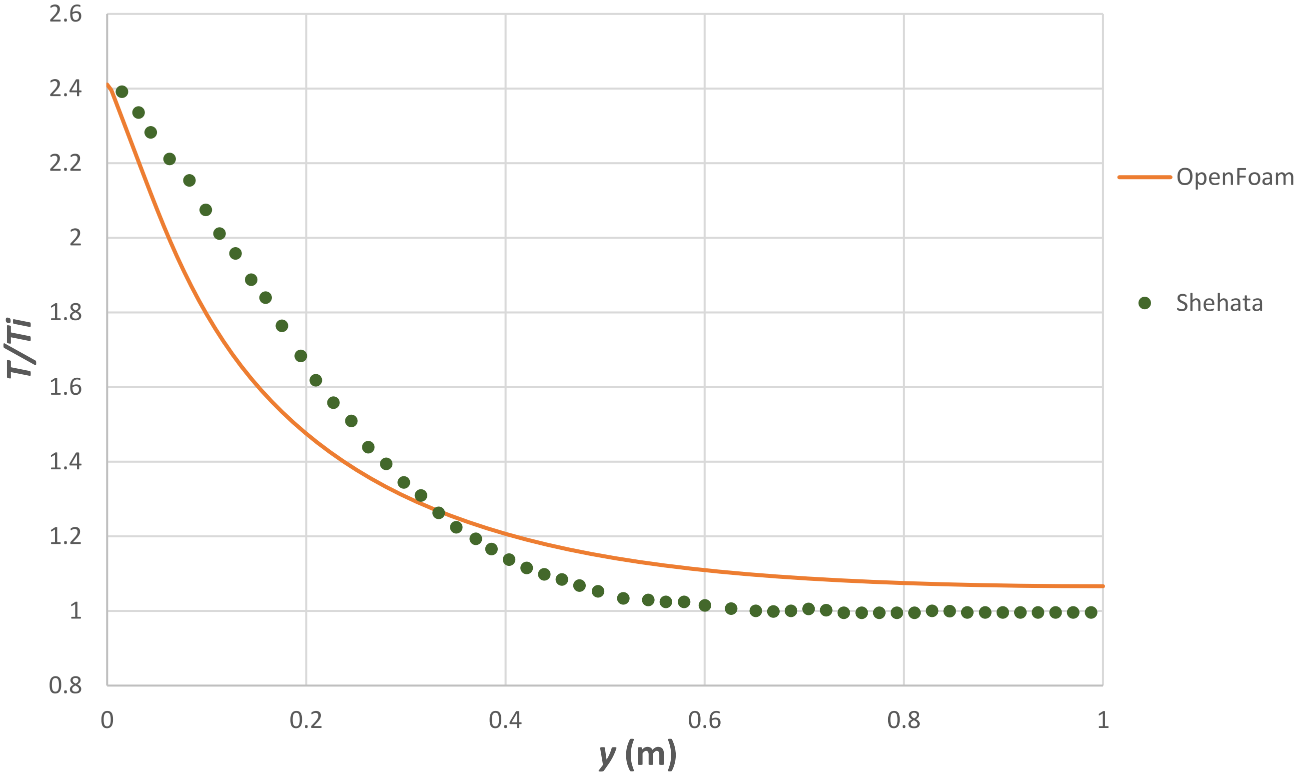

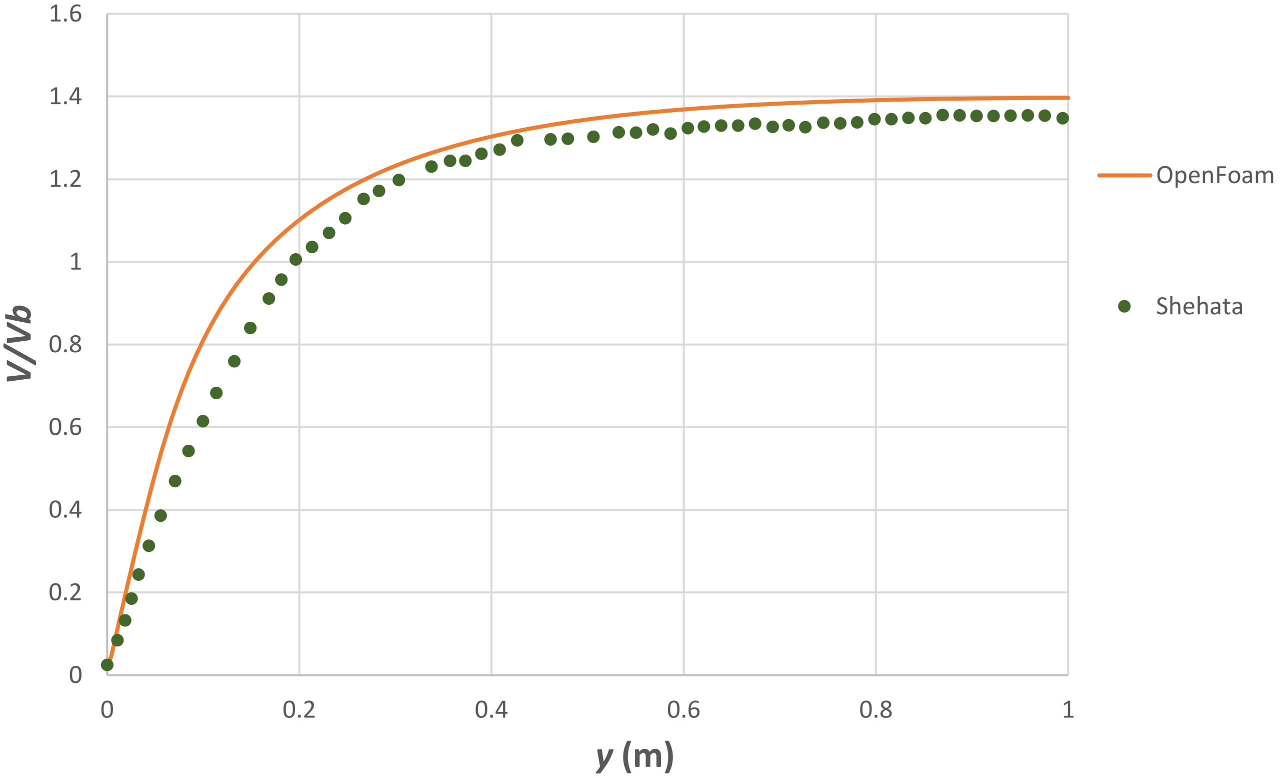

Figure 18: "Run 445" validation. Top: Temperature distribution / Bottom: Velocity profiles

4. Numerical Experiments Set-up

4.1 Base Case

The goal of the numerical experiments in this study is to investigate whether simple geometry modifications can promote heat transfer in an upward flow of air through a vertical heated pipe. As mentioned in the first chapter, the effect of buoyancy can lead to the laminarization of a turbulent upward flow, leading to heat transfer deterioration. To be able to investigate that, a base case needs to be modelled first, in which the laminarization of a turbulent flow needs to be evident. The geometry of the domain resembles the one explained in the previous chapter, developed for the validation of the "Shehata" case, where the domain was represented by a "wedge" geometry since it is an axisymmetric problem. However, the pipe length was increased so that the flow can develop further.

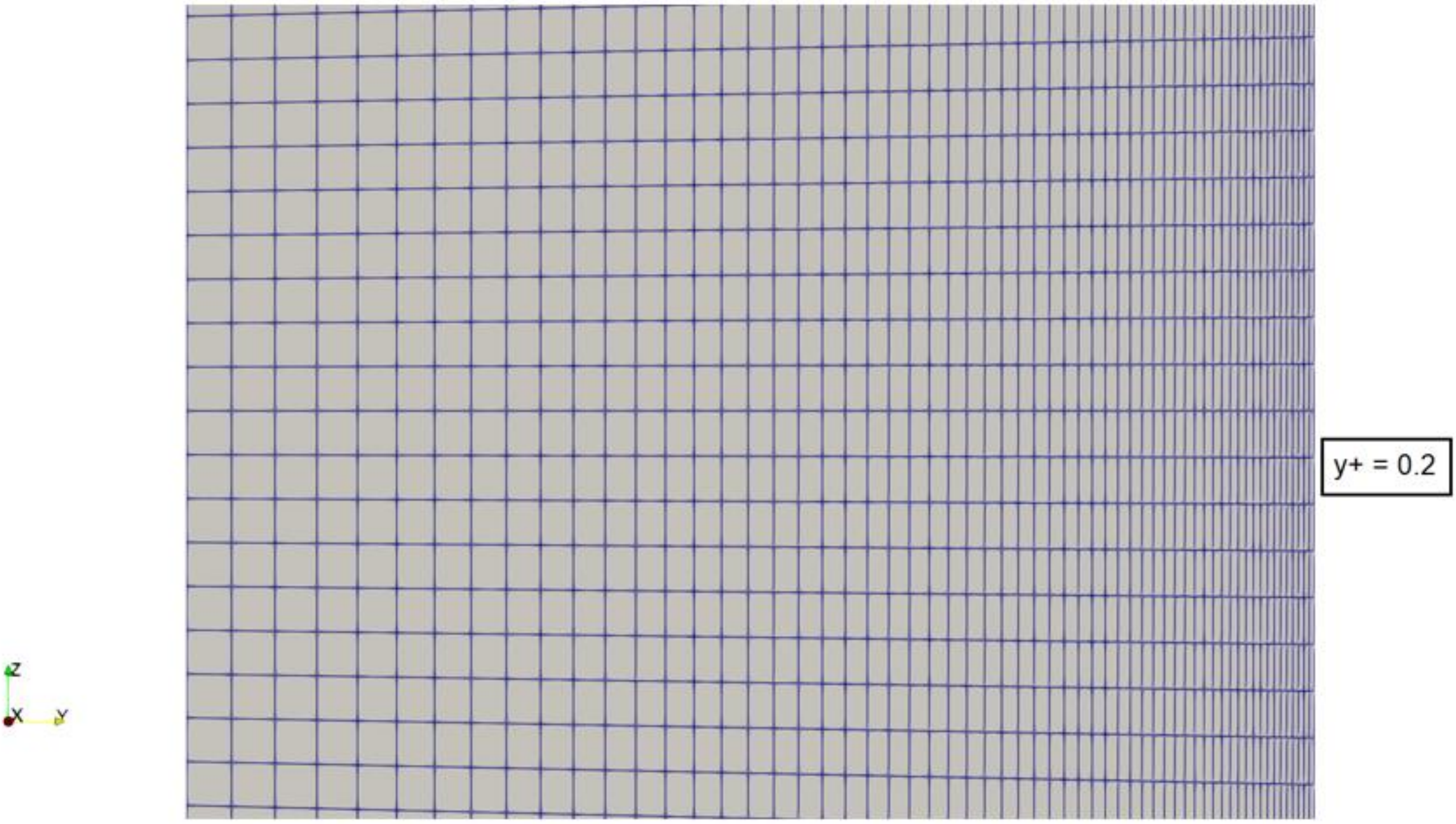

Figure 19: Base case mesh representation.

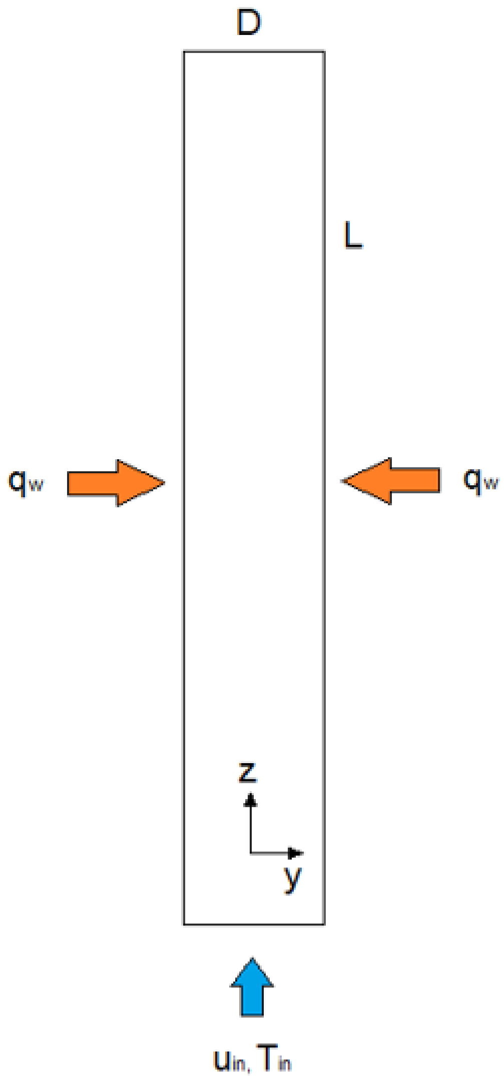

Figure 20: Base case geometry.

Table 11 includes details about the meshing and geometry of the base case, shown in Figures 19 and 20 respectively. It is important to note that air is modelled to flow towards the z-direction.

Table 11: Base case geometrical and meshing details.

Variable	**Symbol**	**Value**
Pipe length (m)	L	2
Pipe diameter (m)	D	0.1
Number of cells in z-direction	$N_{cells,z}$	1000
Number of cells in y-direction	$N_{cells,y}$	60
Y-direction cell to cell expansion ratio (starting from the axis)	r	0.961
Total number of cells	N_{cells}	60000

After creating the base geometry, flow conditions needed to be chosen carefully, so that laminarization could be evident. Table 12 includes the main flow conditions of the base case, indicating a Reynolds number higher than 4000 which falls into the turbulent regime for internal flows. For the calculations, the kinematic viscosity was taken as $v = 1.48 \times 10^{-5} \left(\frac{m^2}{s}\right)$.

Table 12: Base case flow conditions.

Variable	Symbol	Value
Inlet velocity (m/s)	u_{in}	0.785
Inlet temperature (K)	T_{in}	290
Reynolds number	Re	5304
Wall heating rate (W/m^2)	q_{wall}	1285

Equation of State - Turbulence Modelling

As mentioned in Chapter 2, the flows are modelled using the Boussinesq equation of state, defined by three constants representing the thermal expansion coefficient, a reference temperature, and a reference density. These are chosen equal to $\beta = 0.002\ K^{-1}$, $T_0 = 545\ K$ and $\rho_0 = 0.832\ kg/m^3$ as in the case of Shehata's validation shown in Table 9.

Turbulence was modelled using both "k-ωSST" and "SA", solved by **"buoyantPimpleFoam"**. In the first case, boundary and initial conditions for the turbulence kinetic energy, k, and the turbulent specific dissipation rate, ω, need to be specified. When using "SA", these are substituted by the modified turbulent viscosity $\tilde{\nu}$, which relates to the turbulent viscosity through equations (30)-(32). More specifically, in OpenFOAM the "k" and "omega" directories are substituted by "nut", representing the turbulent viscosity and "nuTilda" for the modified turbulent viscosity. Table 13 includes the initial and boundary conditions required for both turbulence models.

Table 13: Base case boundary conditions.

Field	Symbol	Initial Field	Inlet	Outlet	Wall
Velocity	U	uniform (0 0 0)	fixedValue uniform (0 0 0.785)	zeroGradient	noSlip
Pressure	P	uniform 0	calculated	calculated	calculated
Hydrostatic Pressure	p_rgh	uniform 0	fixedFluxPressure uniform 0	prghPressure	fixedFluxPressure uniform 0
Temperature	T	uniform 290	fixedValue uniform 290	zeroGradient	fixedGradient unifrom 50000
Turbulent kinetic energy	k	unifrom 0.0027	fixedValue unifrom 0.0027	zeroGradient	fixedValue uniform 1e-15
Turbulent specific dissipation rate	omega	uniform 0.96	fixedValue uniform 0.96	zeroGradient	omegaWallFunction
Turbulent viscosity (m^2/s)	nut	uniform 0.00288	calculated	zeroGradient	fixedValue uniform 0
Modified turbulent viscosity (m^2/s)	nuTilda	uniform 0.0144	fixedValue uniform 0.0144	zeroGradient	fixedValue uniform 0

Values for the initialization of the turbulent kinetic energy and specific dissipation rate were obtained using equations (55), (56). Estimations for the initialization of the “nut” field were made using the formulas [63]:

$$\nu_t = C_\mu \frac{k^2}{\varepsilon} \tag{58}$$

$$\varepsilon = \frac{{C_\mu}^{0.75} k^{1.5}}{L} \tag{59}$$

where ε represents the dissipation of turbulent kinetic energy, while the initial value of the modified turbulent viscosity field was taken equal to five times the turbulent viscosity, following suggestions from CFD forums [63]. Details for k and C_μ are shown in section 3.2, equations (52)-(54). The value of the **“fixedGradient”** boundary condition imposed at the wall on the temperature field corresponds to the gradient $\frac{\partial T}{\partial y}$ included in the wall heat flux term expressed by equation (60), assuming air conductivity $\lambda_{air} = 0.025\ (W/mK)$

$$q_{wall} = -\lambda_{air} \frac{\partial T}{\partial y} \tag{60}$$

Finally, it is noted that numerical schemes and linear solvers were chosen as explained in sections 2.5 and 2.6.

Flow Laminarization

To investigate whether the flow becomes laminar along the pipe in the base case, mean axial velocity profiles were compared for different cross-sections along the domain. Qualitatively, an indication of laminarization in mixed convection upward flows is the “M-shape” with the highest velocities being close to the heated wall followed by lower velocities towards the pipe axis. This is evident in our case, as shown by Figures 21 and 22, with three different curves representing velocity at 0.5, 1 and 1.5 meters from the inlet, using “*k-ωSST*” and “*SA*” respectively. Additionally, Figures 23 shows that the turbulent kinetic energy along the axis of the pipe decreases when using “k-ωSST”, a second indication of flow laminarization. Finally, the same logic applies to the case of “SA” modelling, with flow laminarization implied by a decrease the modified turbulent viscosity along the axis of the pipe, shown in Figure 24.

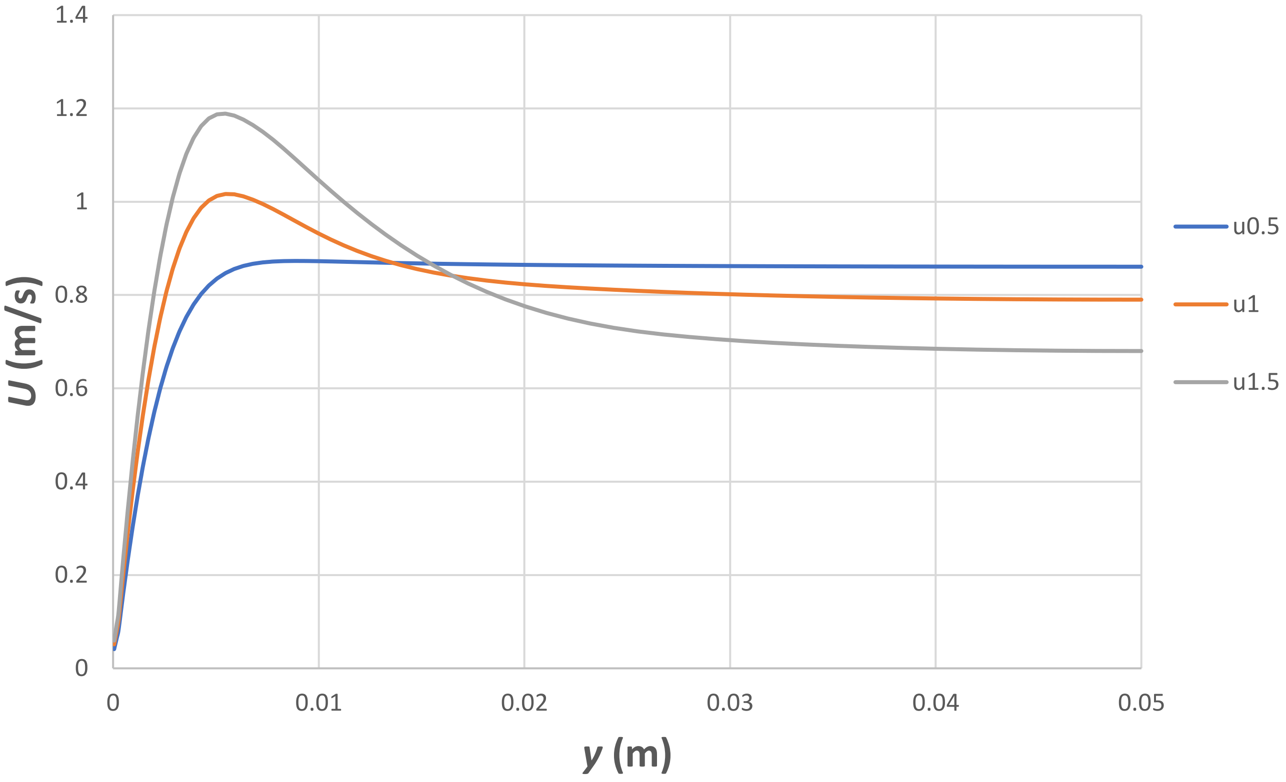

Figure 21: Base case mean axial velocity profile development using "k-ωSST".

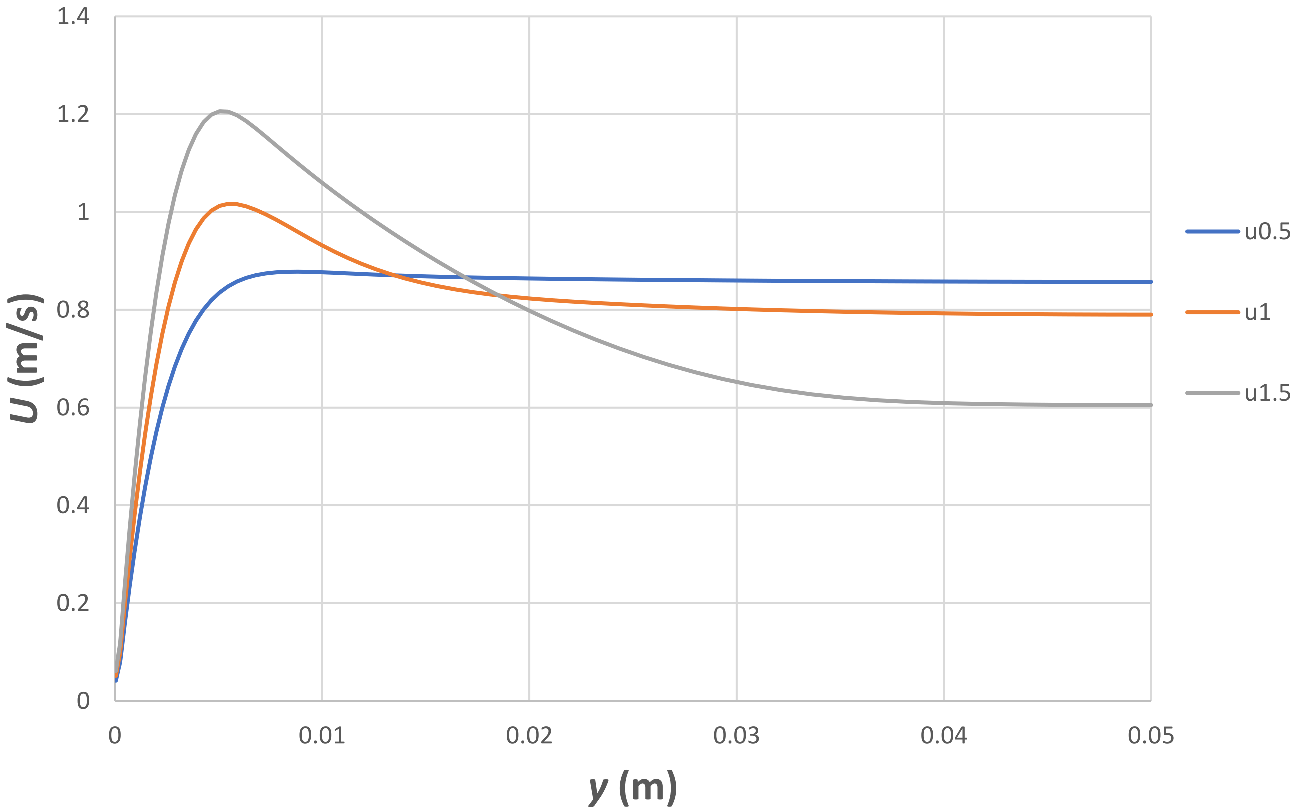

Figure 22: Base case mean axial velocity profile development using "SA".

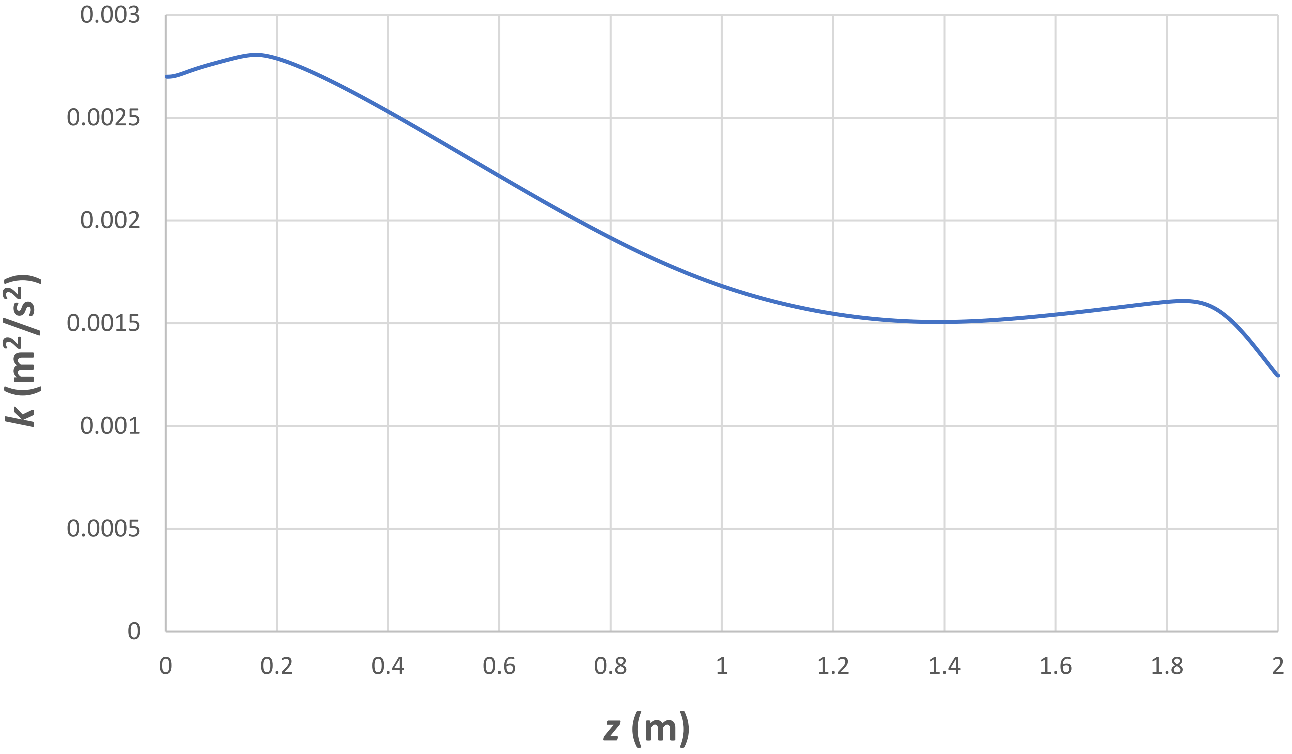

Figure 23: Base case turbulent kinetic energy development using "k-ωSST" along the pipe centerline.

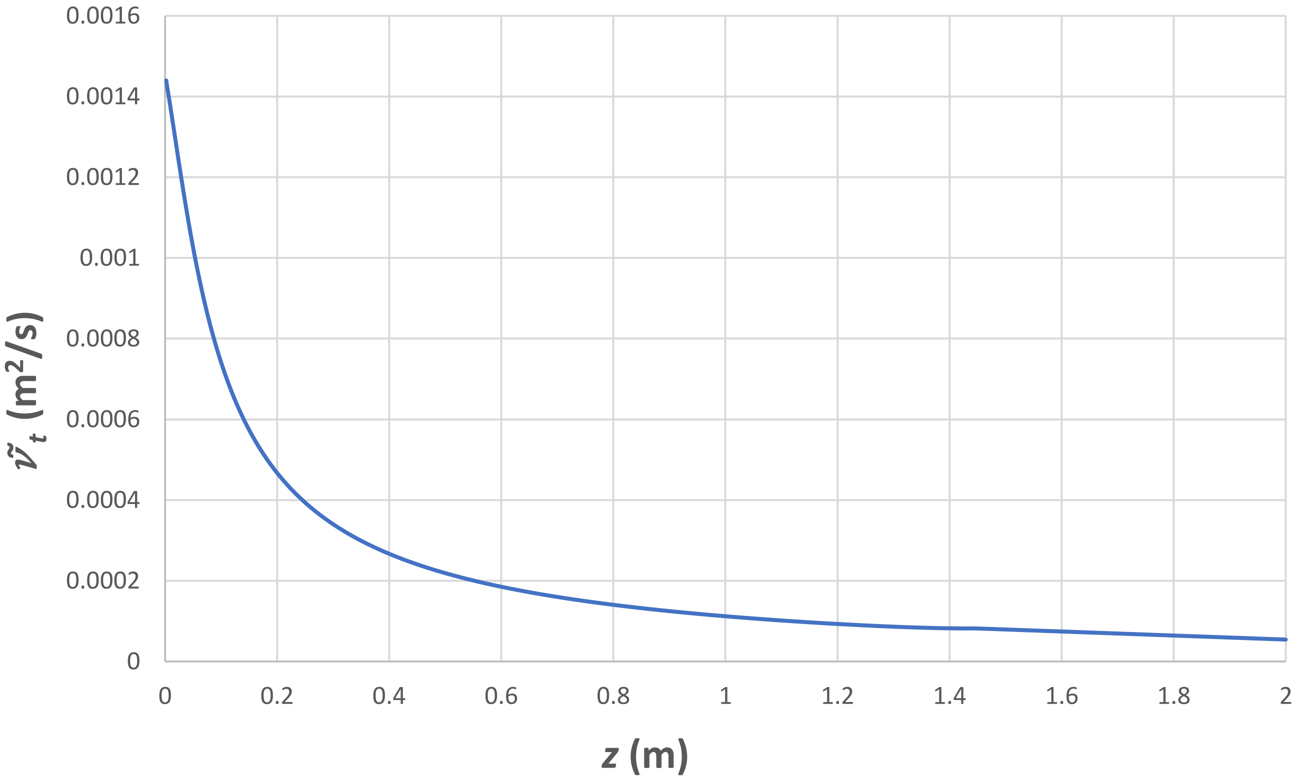

Figure 24: Base case turbulent modified turbulent viscosity development using "SA" along the pipe centerline.

4.2 Artificially Roughened Cases

The geometry of choice in the current study is a transverse rib one, with an orthogonal profile, as shown in Figure 25. Transverse ribs geometries have been researched widely for heat transfer enhancement for many years. Chang et al. [67] simulated transverse ribs in turbulent channel flows using RANS combined with the "*k-ε*" turbulence model, predicting higher effect on friction compared to heat transfer. Karwa [68] studied the effect of transverse ribs, among other rib patterns, in rectangular ducts, developing heat transfer and friction correlations. San et al. [69] investigated the effect of different pitch-to-diameter ratios in transverse rib geometries and created a performance map.

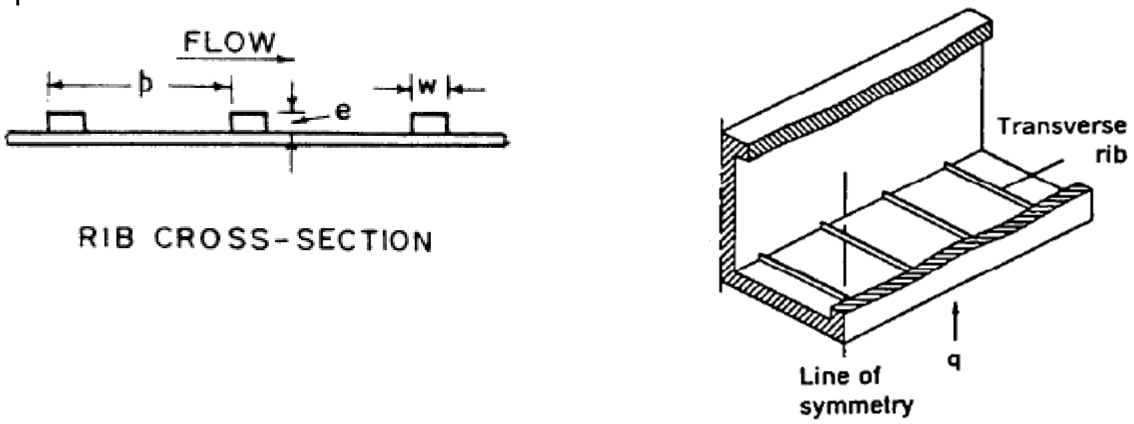

Figure 25: Transverse rib geometry representation by different researchers: Left [68] / Right [67].

Even though there is extended research on transverse rib geometries, their effect on mixed convection flows has not been extensively studied, which, combined with their simplicity, makes them an ideal choice. The geometry and mesh representation are shown in Figures 26 and 27 respectively. A wedge geometry was implemented resembling the base case.

Figure 26: Geometry representation of a transverse rib in OpenFOAM.

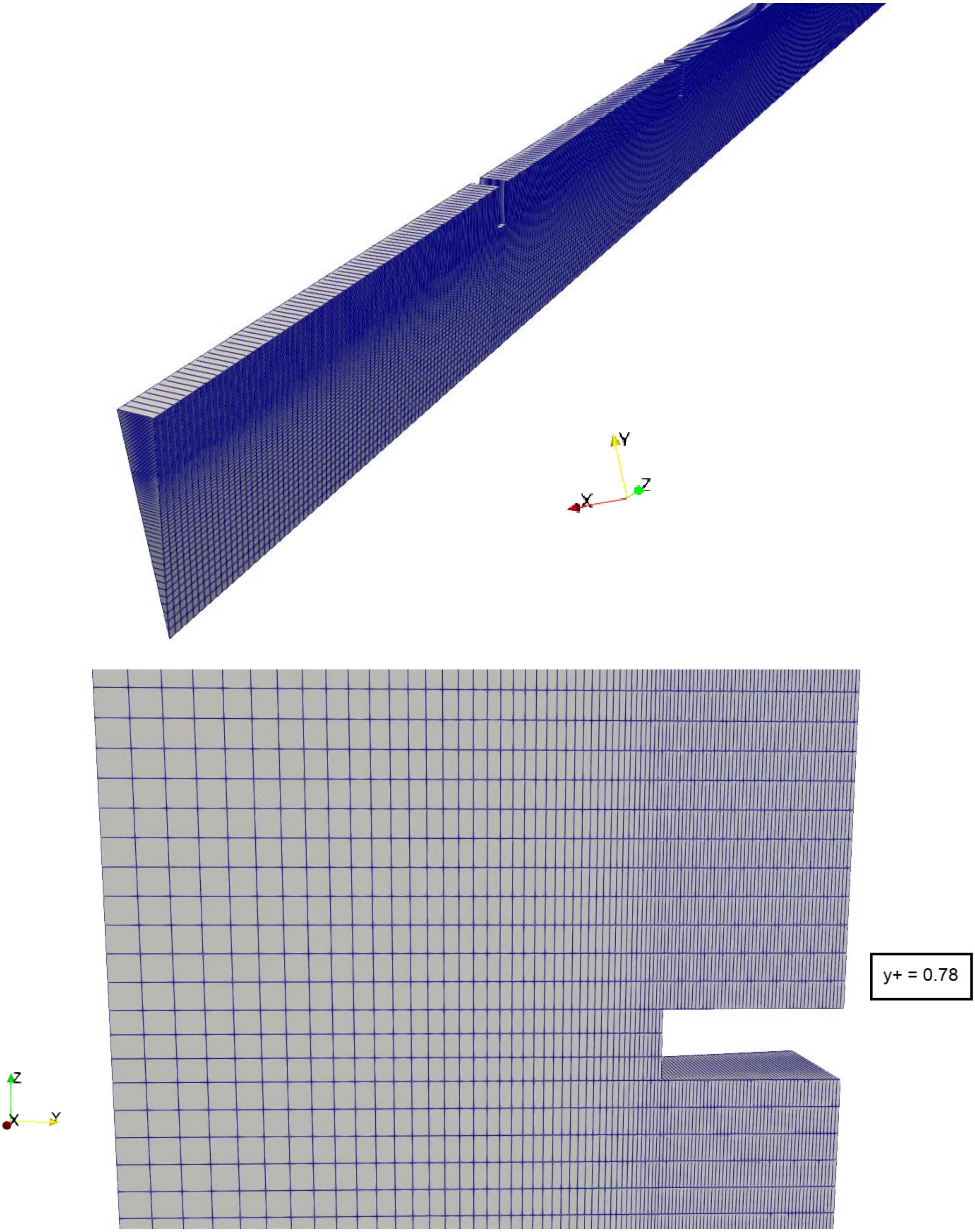

y+ = 0.78

Figure 27: Mesh representation of a transverse rib in OpenFOAM.

The geometry was meshed under the criteria explained in chapter 2.7. The major difference between the grid of a ribbed case compared to the base one, is that there are additional cells along the y-direction, so that the y^+ is kept bellow one at the tip of the rib. Figure 28 includes a representation of the most important parameters of a transverse ribbed geometry.

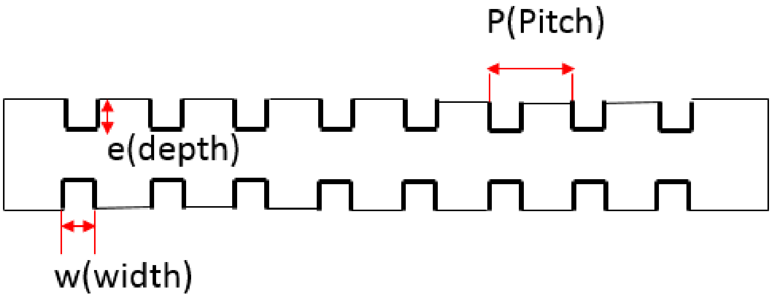

Figure 28: Geometrical parameters of a ribbed pipe.

Different pitch-to-diameter and pitch-to-depth ratios have been studied with a constant rib width. Table 14 summarizes each geometry simulated in the current study. The length and diameter of the pipe are taken equal to $L = 2\ (m)$ and $D = 0.1\ (m)$ respectively, as in the base case. Meshing for each simulation was implemented setting a target total number of cells $N_{cells} \cong 98000$.

Table 14: List of transverse rib simulations and geometrical specifications.

Simulation Name	**pitch,** $\boldsymbol{p\ (m)}$	**depth,** $\boldsymbol{e\ (m)}$	**width,** $\boldsymbol{w\ (m)}$	$\boldsymbol{p/D}$	$\boldsymbol{e/D}$	**Number of ribs** $\boldsymbol{N_{ribs}}$
J	0.15	0.01	0.005	1.5	0.1	13
M	0.15	0.0125	0.005	1.5	0.125	13
P	0.15	0.015	0.005	1.5	0.15	13
T	0.15	0.0175	0.005	1.5	0.175	13
K	0.1	0.01	0.005	1	0.1	20
N	0.1	0.0125	0.005	1	0.125	20
L	0.125	0.01	0.005	1.25	0.1	16
O	0.125	0.0125	0.005	1.25	0.125	16
Q	0.125	0.015	0.005	1.25	0.15	16
U	0.125	0.0175	0.005	1.25	0.175	16
V	0.175	0.0175	0.005	1.75	0.1	11
S	0.175	0.015	0.005	1.75	0.15	11
R	0.175	0.01	0.005	1.75	0.175	11

Table 15 summarizes the grid details of the “M” simulation and even though the number of cells in each simulation changes slightly, the difference is insignificant. Variables are split into two areas, the areas where no ribs are present, noted as “smooth” and the areas where a rib is present, noted as “rough”.

Table 15: List of transverse rib simulations and geometrical specifications.

Region	Variable	Symbol	Value
Smooth	Number of cells in z-direction	$N_{rough,z}$	75
	Number of cells in y-direction	$N_{rough,y}$	92
	Y-direction cell to cell expansion ratio (from the axis to the rib tip)	r_{rough}	0.954
Rough	Number of cells in z-direction	$N_{rough,z}$	3
	Number of cells in y-direction	$N_{rough,y}$	50
	Y-direction cell to cell expansion ratio (starting from the axis)	r_{rough}	0.954
Total	Total number of cells	N_{cells}	98238

Equation of State - Turbulence Modelling

The transverse ribbed cases were modelled in the same way as the base case, explained in section 4.1, using the **buoyantPimpleFoam** solver with the Boussinesq equation of state, investigated using *"k-ωSST"* and *"SA"* for turbulence modelling. Numerical schemes and linear solvers were chosen as explained in sections 2.5 and 2.6. The problem was set up under the boundary and initial conditions presented in Table 13.

Results on the transverse ribbed geometry on heat transfer and friction using "k-ωSST" are presented and discussed in Chapter 5, followed by the corresponding results using "SA" in Chapter 6. A performance comparison of all the simulations for both turbulence models is presented in Chapter 7.

5. Results: Menter Shear Stress Transport Turbulence Model

5.1 Heat Transfer

The enhancement achieved by the ribbed tube in each simulation is compared to the base case. Comparisons are made based on the local dimensionless Nusselt number along the pipe, given by:

$$Nu_z = \frac{hD}{\lambda_{air}} \tag{61}$$

with

$$h = \frac{q_{wall}}{T_{wall} - T_b} \tag{62}$$

$$T_b = \frac{\int \rho u \, dA}{\int \rho \, dA} \tag{63}$$

Where h is the convective heat transfer coefficient in $\frac{W}{m^2 K}$ and T_b is the bulk temperature in K. For each simulation, the local Nusselt number was evaluated at different cross sections along the length of the pipe and compared with the base case. Each point refers to the middle of the region between two consecutive ribs. An example of such a comparison is given in Figure 29, where the case coded as "R" is compared with the base case using the *"k-ωSST"* model. It is notable that the flow is still developing after ~ 1 meter, which is the case for all simulations. Thus, comparisons will be made after an entrance length, $L_{entrance} = 1\, m$ equal to 10 tube diameters, assuming that the flow is developed at that point.

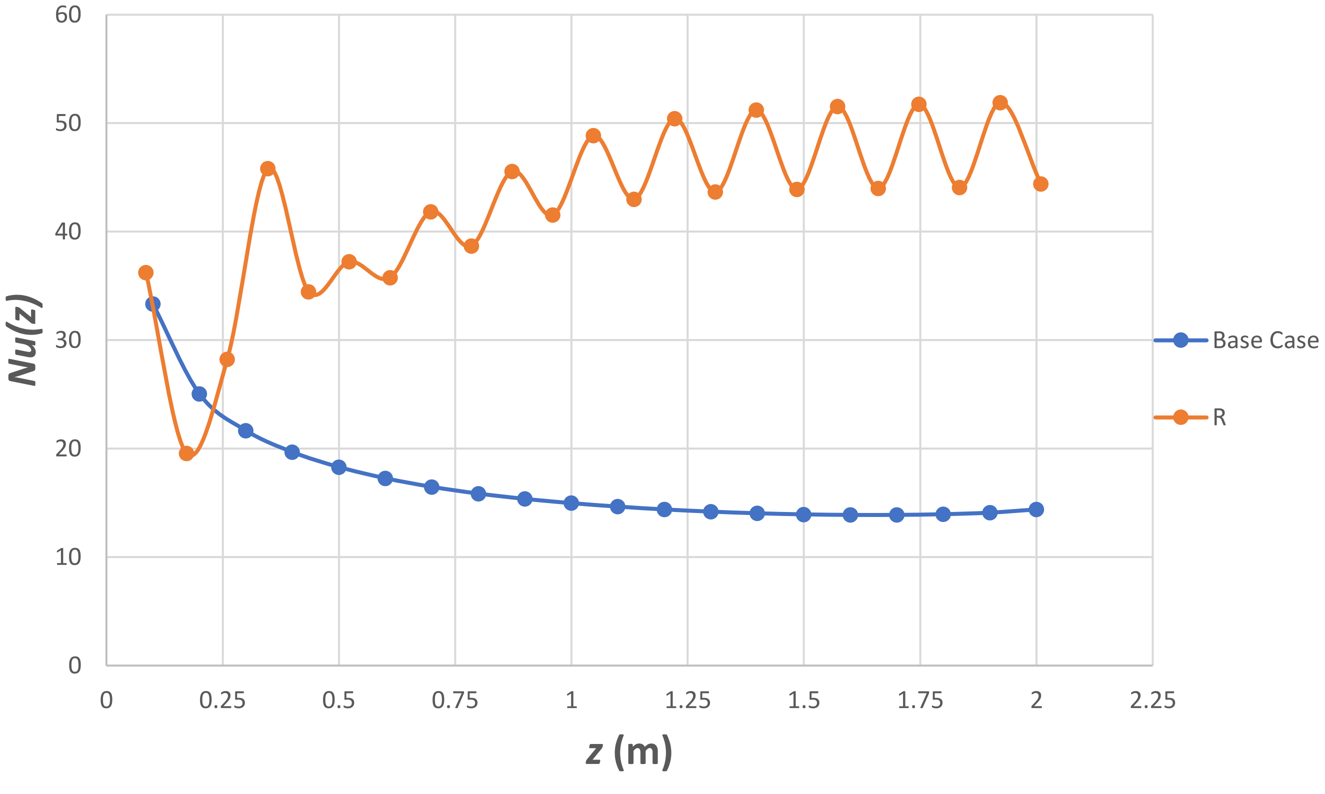

Figure 29: "R" case local Nusselt comparison with base case using "k-ωSST".

Looking at Figure 29, it becomes evident that heat transfer is promoted, achieving Nusselt ratios reaching $\frac{Nu_z}{Nu_{z0}} > 3$ in the developed region of the flow. This can be explained by investigating the difference between the bulk and the wall temperature along the pipe for the case “R”, shown in Figure 30. Temperature differences are lower compared to the base case, shown in Figure 31, for a constant wall heating rate, justifying the higher heat transfer coefficients calculated.

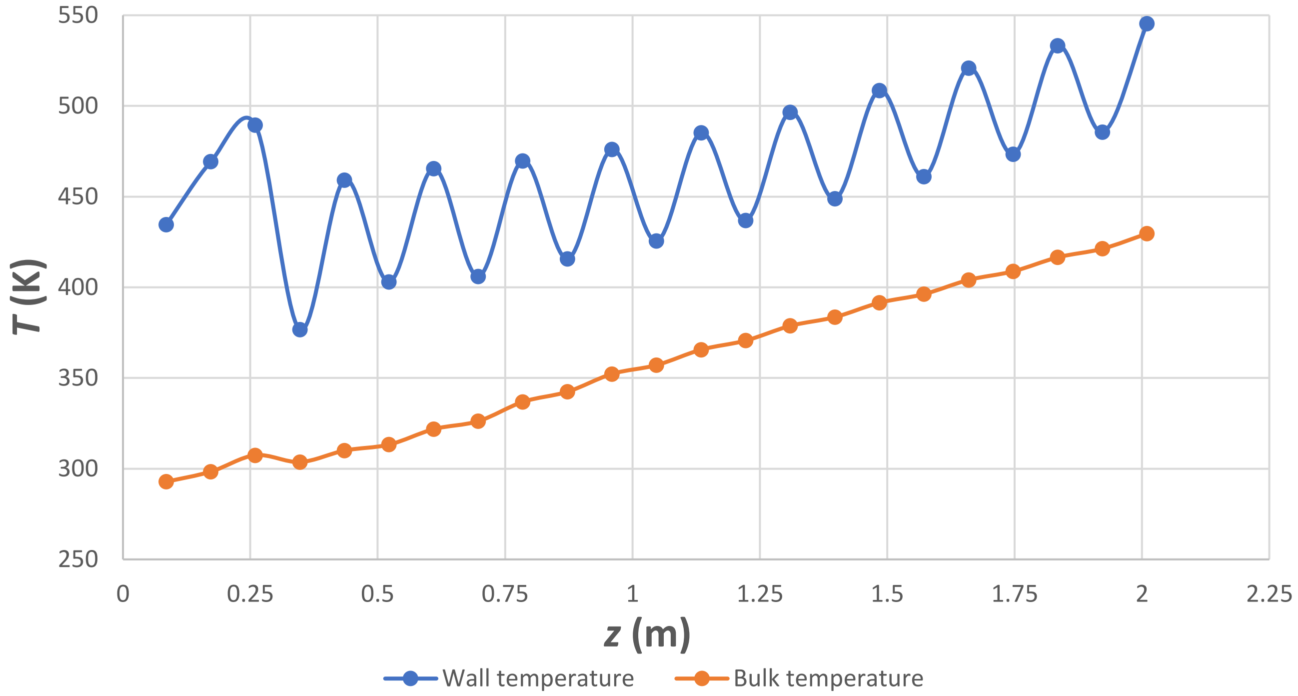

Figure 30: “R” case temperature differences along the pipe.

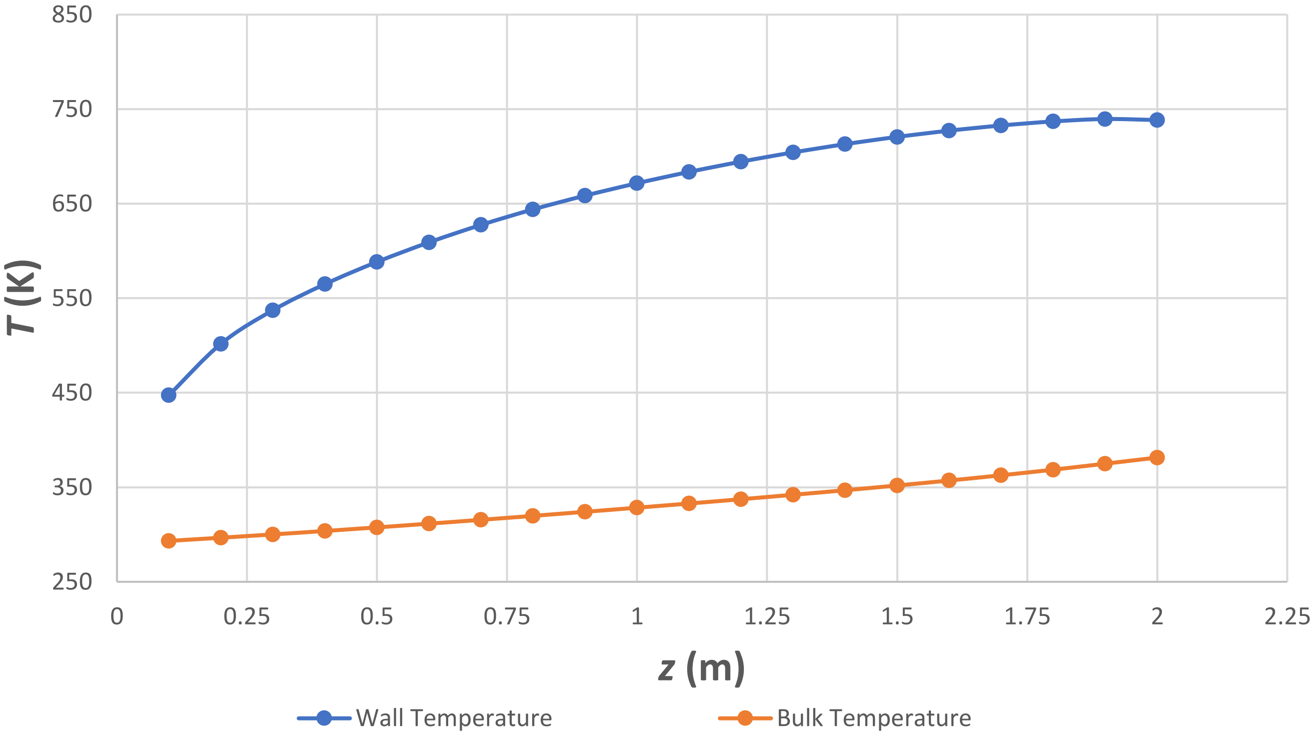

Figure 31: Base case temperature differences along the pipe.

An important remark concerning the Nusselt number development along the ribbed pipe is the oscillatory behaviour, shown in Figure 29. Nusselt number local maxima refer to cross-sections in the middle of ribs, while Nusselt number local minima are calculated for the middle of the region between two consecutive ribs. This comes because of the wall's temperature oscillatory behaviour, with local maxima referring to cross-sections at the middle of the region between consecutive ribs and local minima at cross-sections in the middle of a rib. To understand this behaviour, the Nusselt number distribution at the region between two consecutive ribs has been calculated, shown in Figure 32. The region between two consecutive ribs at a length between 1.4975 and 1.6475 meters for the "M" case has been used as an example. Figure 33 shows streamlines for the same region. Coloring is based on the values of mean axial velocity, U_z, with red regions referring to higher velocities.

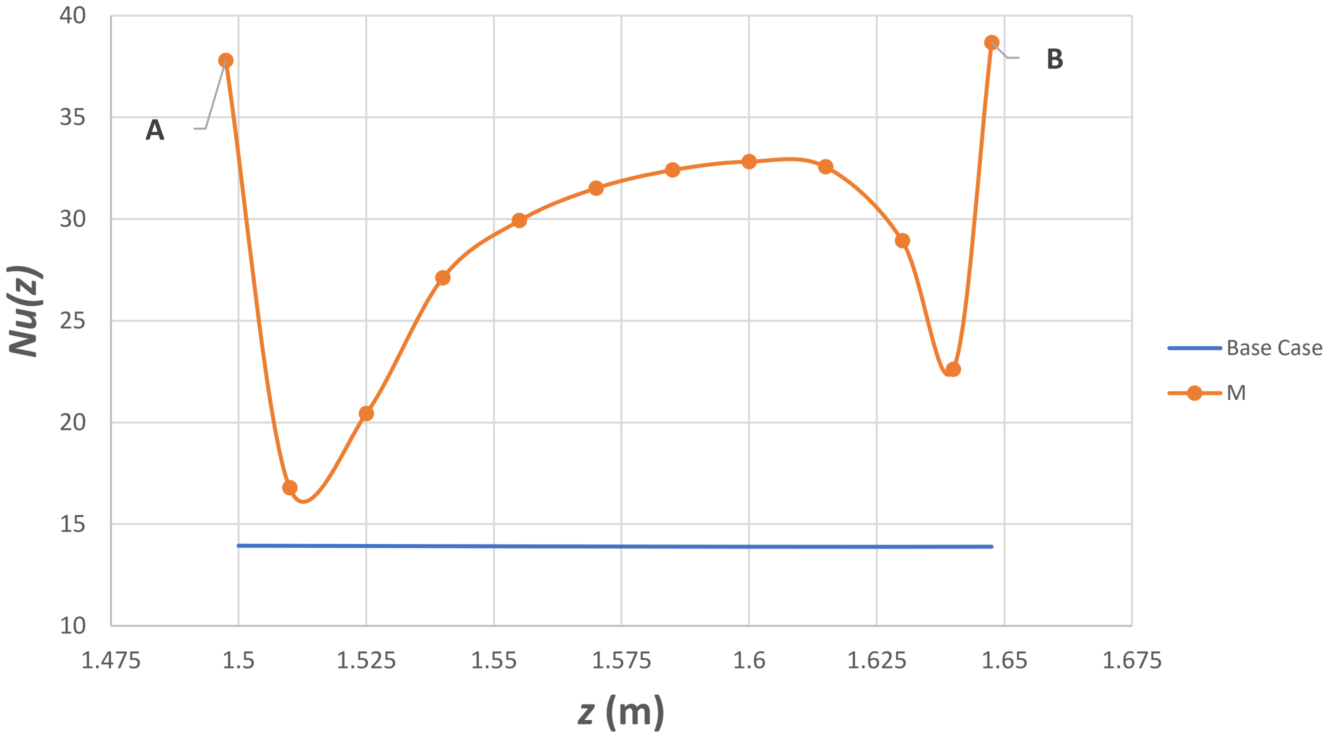

Figure 32: "M" case Nusselt development between consecutive ribs.

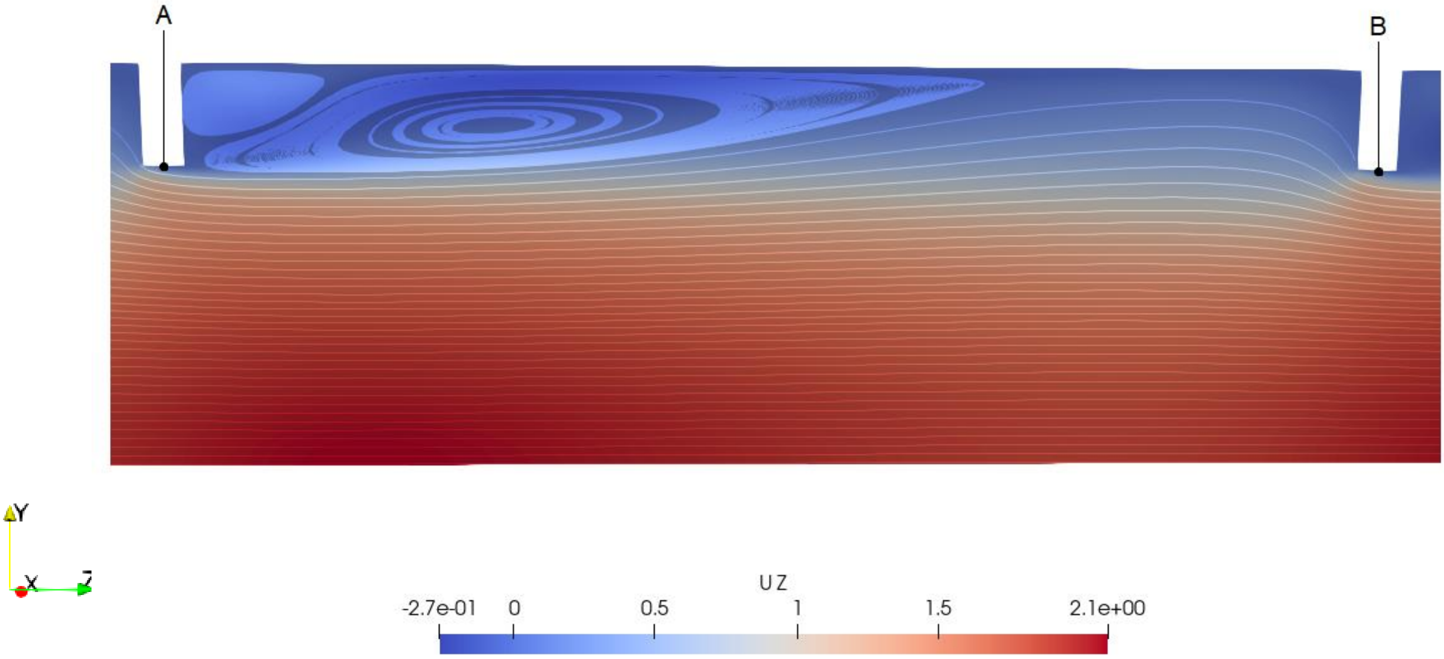

Figure 33: "M" case streamlines between consecutive ribs.

The leftmost and rightmost points in Figure 32 refer to cross-sections at the middle of the two ribs shown in Figure 33. Following the Nusselt number development, we notice a heat transfer deterioration at the region behind the first rib, where the lowest heat transfer coefficients are obtained. Two vortices are generated, evident in Figure 33, creating a recirculating region which acts detrimentally for heat transfer, since the fluid is prevented from flowing close to the heated wall. As the flow progresses less recirculation is noticed resulting into higher Nusselt numbers, reaching a local maximum at the region where recirculation is no longer present. Heat transfer deterioration is noticed again at the region before the second rib, as there is a steep change in the angle of the flow, leading to fluid losing contact with the heated wall. It is important to note that even though heat transfer deteriorates at the areas close to the ribs, heat transfer coefficients are still higher compared to the smooth pipe. This is a result of the promotion of turbulence, leading to high mixing in the flow, which is highly beneficial for heat transfer.

In Figure 34 the turbulent viscosity at $y = 0.0375$ meters, exactly at the tip of the ribs, is compared with the base case for the region between two consecutive ribs. It is evident that mixing is promoted, reaching a maximum at the region close to the second rib, where no recirculation region is present. The uneven distribution of the turbulent viscosity shown in Figure 34 relates to the uneven Nusselt number distribution shown in Figure 32, with both showing a maximum at $z \cong 1.615\ (m)$, indicating the importance of turbulence and mixing enhancement for heat transfer.

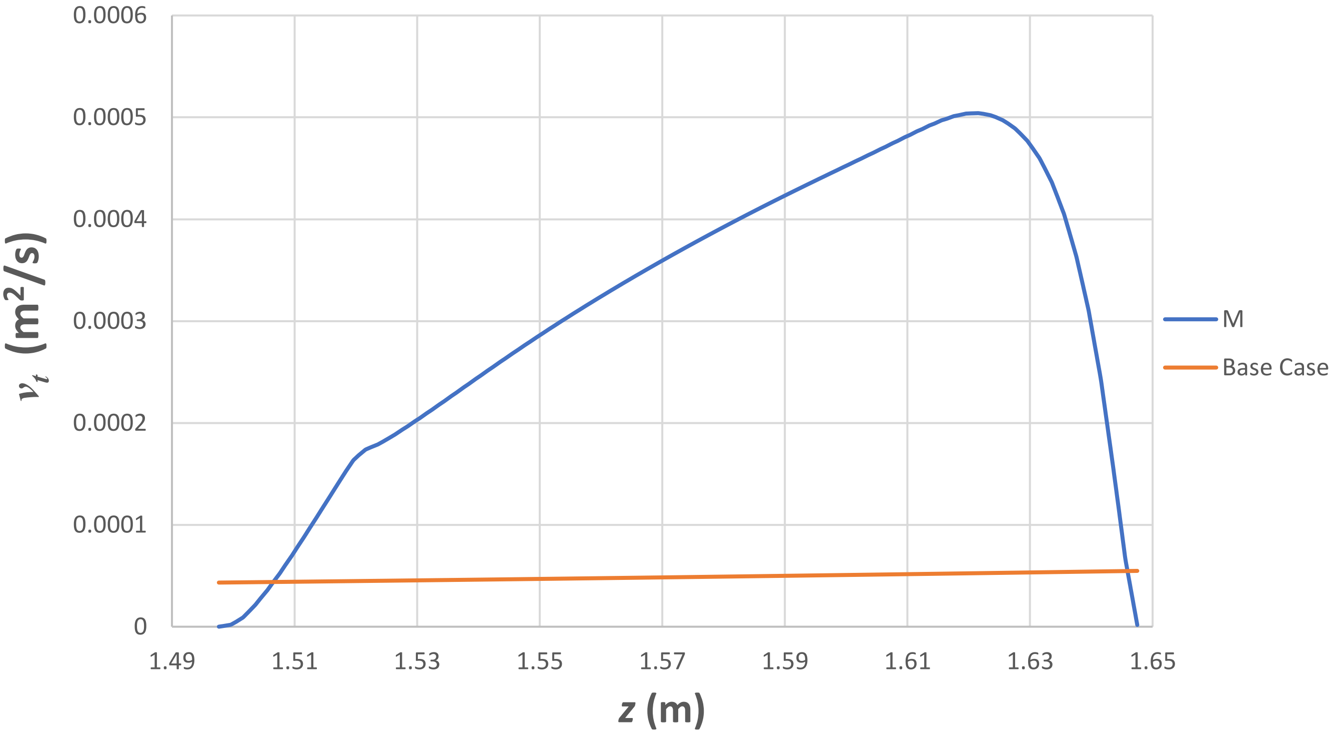

Figure 34: "M" case turbulent viscosity between consecutive ribs along at y = 0.0375 (m).

The recirculation region shown in Figure 33 has a highly beneficial effect on heat transfer by promoting mixing in the flow and preventing the laminarization of the flow, which was evident when investigating the base case. The prevention of flow laminarization by ribbed geometries can be summarized in Figure 35, in which the development of turbulent kinetic energy of the M case is compared with the base case along the centre of the pipe. Results show that turbulence is highly promoted by the rib geometry.

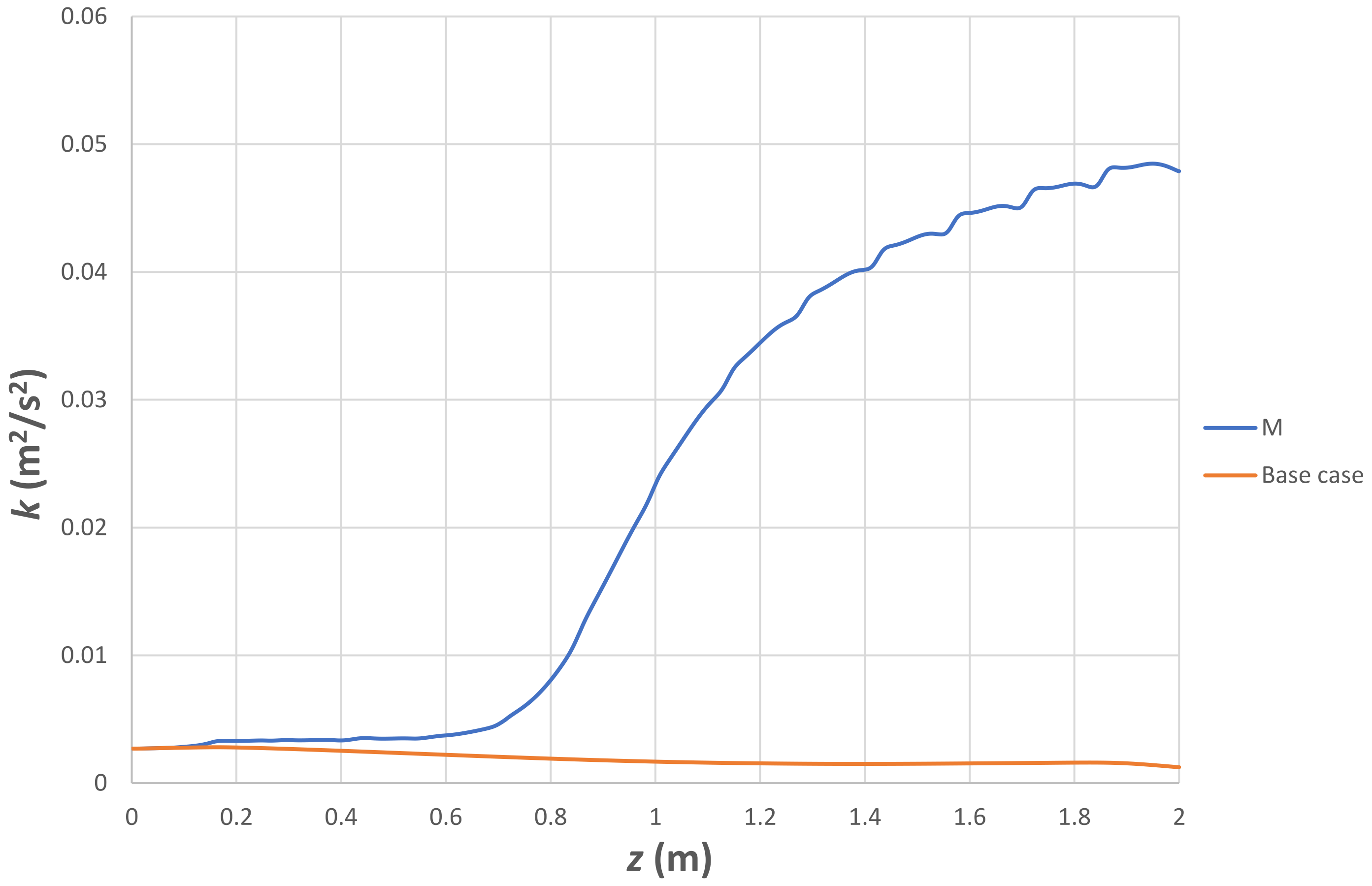

Figure 35: Turbulence kinetic energy development comparison along the pipe centerline using "k-ωSST".

The effect of the rib pitch-to-diameter ratio, p/D, on the local Nusselt number development along the tube is shown in Figure 36. In the cases shown, labeled as "Q", "P" and "S", the rib depth-to-diameter ratio, e/D, is constant and equal to 0.15. On the other hand, Figure 37 depicts the effect of e/D variation on heat transfer for a constant p/D equal to 1.25.

Results using the *"k-ωSST"* model show that a varying pitch-to-diameter ration does not have a significant effect on heat transfer, as shown in Figure 36, with higher ratios resulting into slightly higher Nusselt numbers. On the other hand, the effect of the ribs' depth has a beneficial effect on heat transfer, with higher average Nusselt numbers obtained for higher depths, as shown in Figure 37. Moreover, higher depths lead to higher differences between the local maxima and minima of the Nusselt number distribution.

To further investigate, streamlines are depicted for three different rib depths in Figure 38. The cases M, P and T were used as an example, with M case referring to the smallest depth and T representing the largest. The region depicted is the same region as the one explained in Figures 32 and 33.

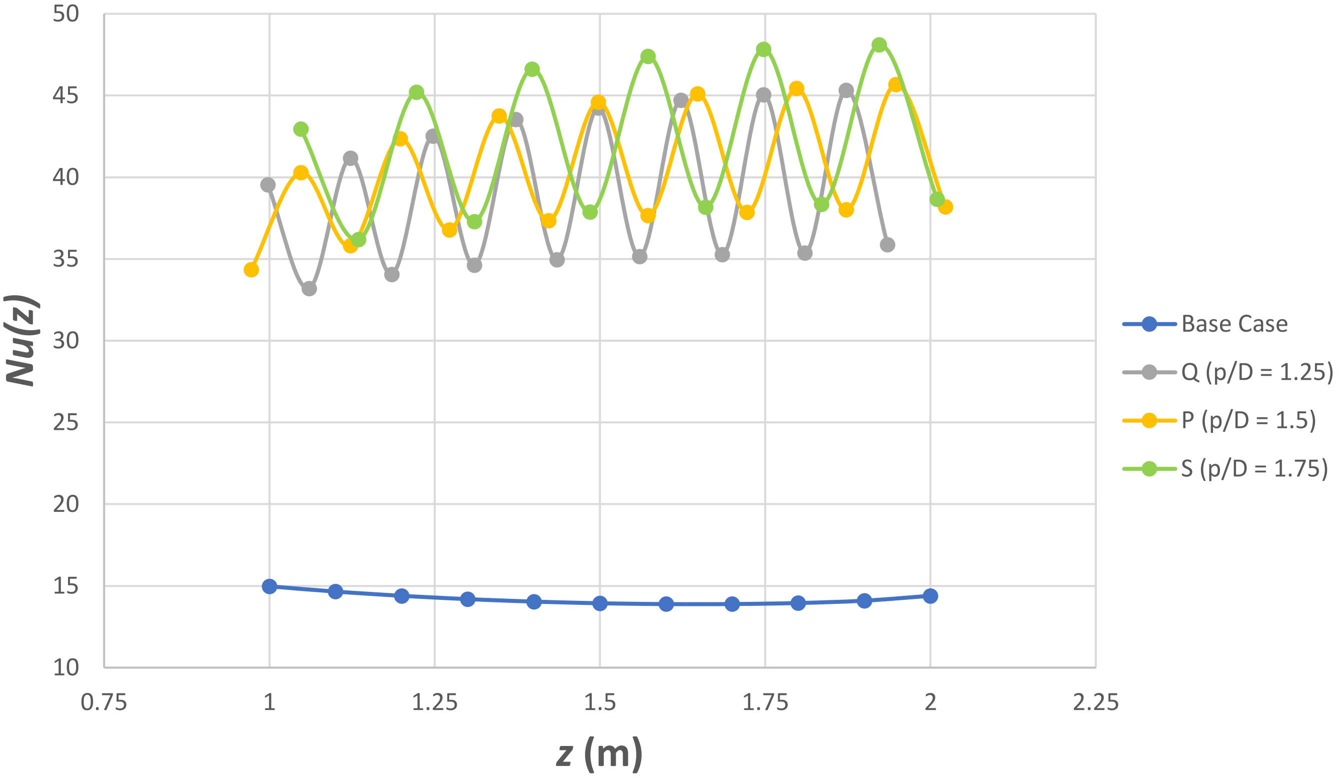

Figure 36: Rib pitch-to-diameter ratio effect on heat transfer using "k-ωSST".

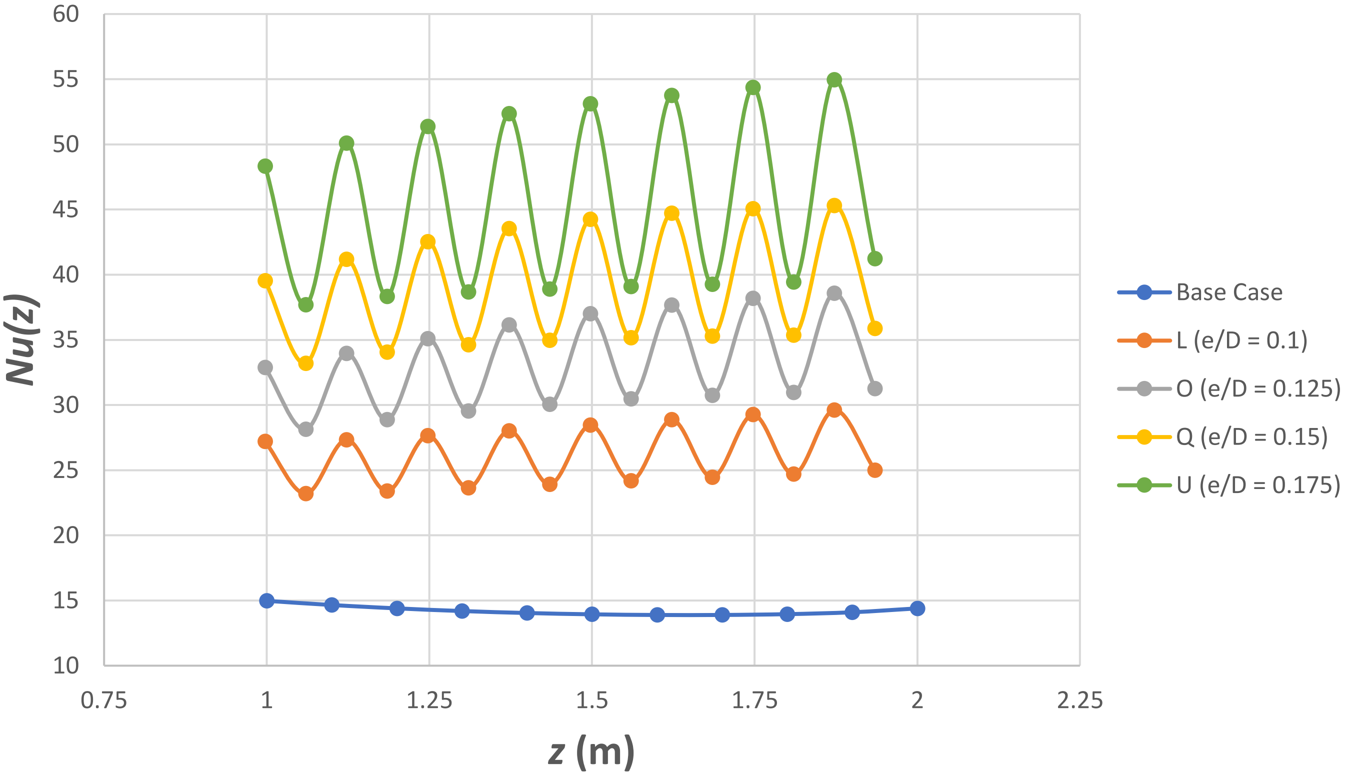

Figure 37: Rib depth-to-diameter ratio effect on heat transfer using "k-ωSST".

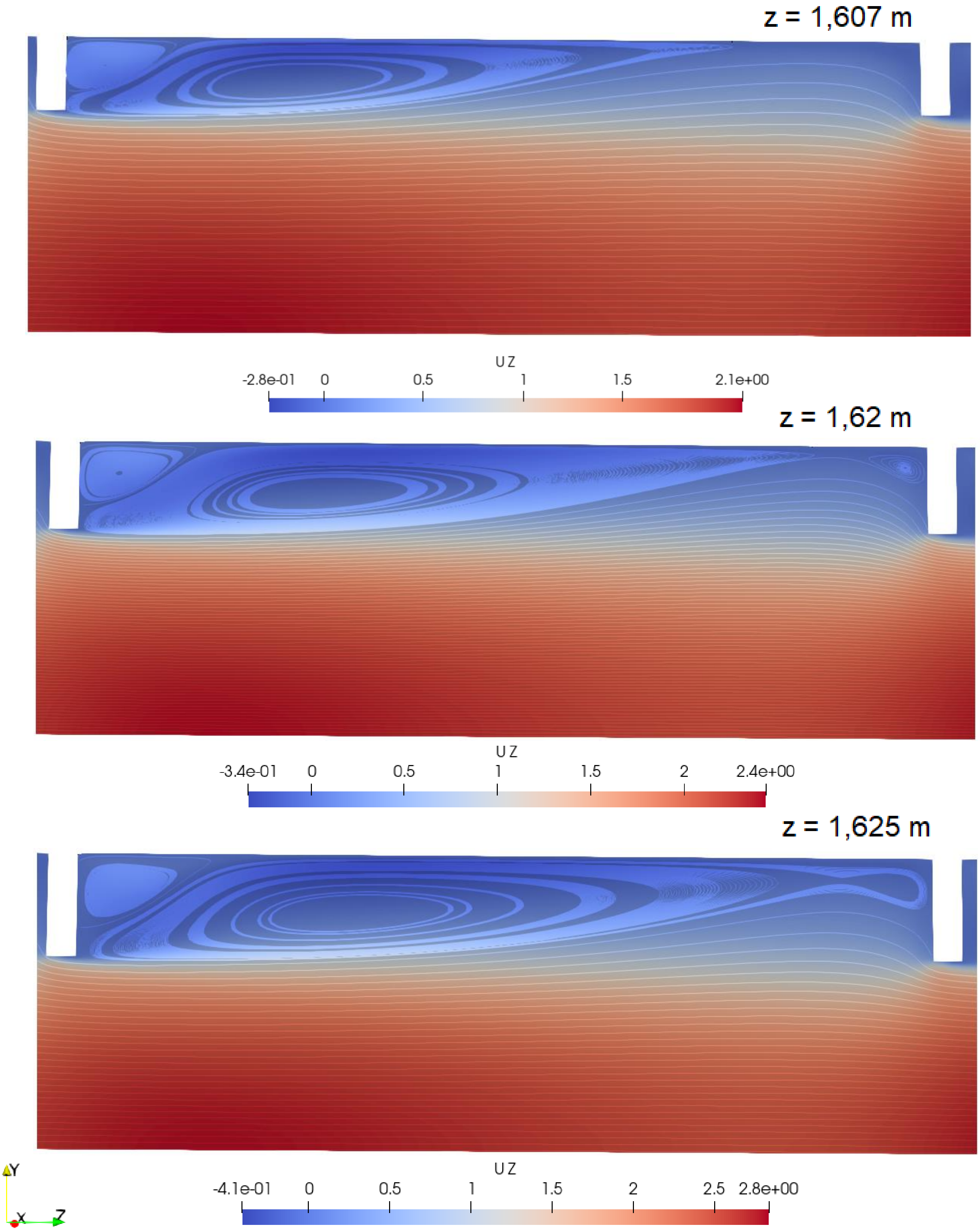

Figure 38: Streamlines, top to bottom: M (e/D = 0.125), P (e/D = 0.15), T (e/D = 0.175) using "k-ωSST".

The coordinate on which the main generated vortex ends is noted at the top right corner of each case, with z = 1.4975 meters referring to the middle of the first rib shown in Figure 38. It is evident that higher rib depths lead to larger recirculation regions. As seen in Figure 39, in which the Nusselt number is compared for the region shown in Figure 38, greater recirculation regions lead to more extended regions of deteriorated heat transfer. However, heat transfer in general benefits from higher ribs' depths, due to the higher promotion of mixing as shown in Figure 40, in which the turbulent viscosity is compared for the three cases along a line at the tip of the ribs.

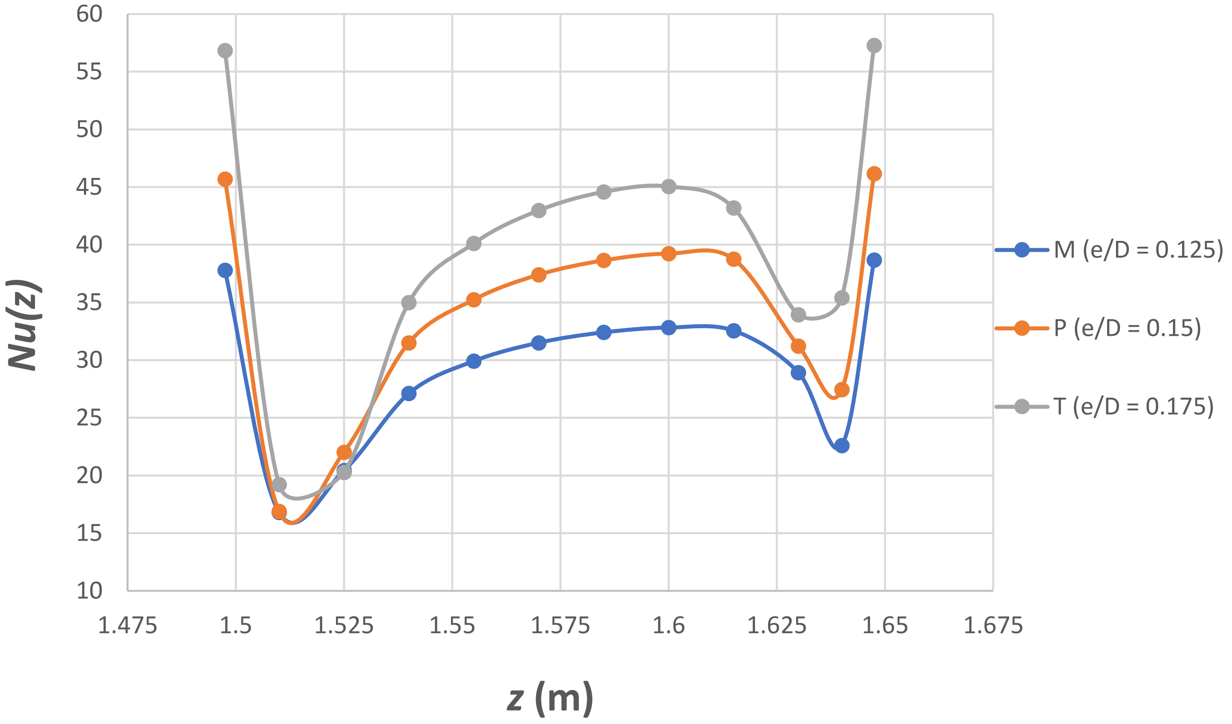

Figure 39: Local Nusselt number in the region between two ribs for different rib depths using "k-ωSST".

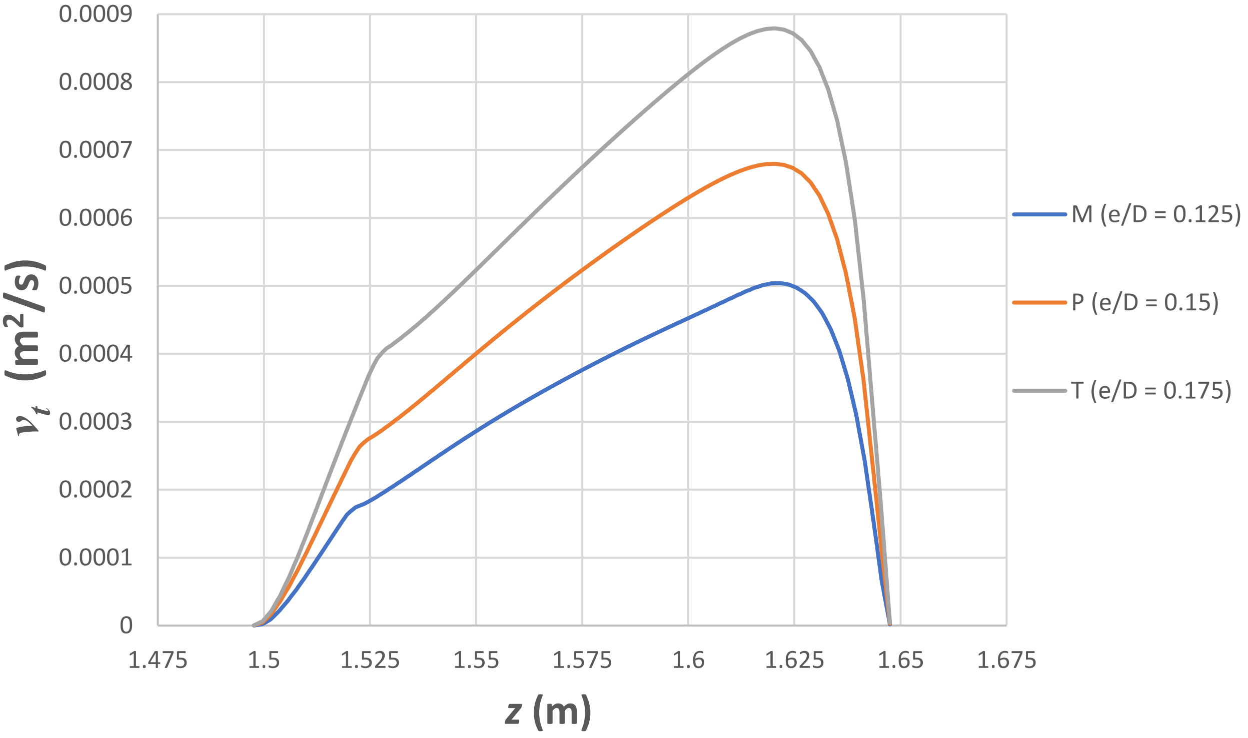

Figure 40: Turbulent viscosity along the center of the pipe for different ribs' depths using "k-ωSST".

5.2 Flow Friction

The increase in friction caused by the artificially roughened pipe is evaluated at different cross sections along the pipe using the Fanning friction factor, given by [70]:

$$f = \frac{\tau_{wall}}{\rho_b \frac{u_b^2}{2}} \tag{64}$$

where ρ_b is the bulk density of the fluid at each cross section evaluated at the bulk temperature T_b given by equation (61) and u_b the bulk velocity of the fluid calculated by equation (55). τ_{wall} represents the shear stress imposed by the wall to the fluid and is calculated by a post-process available in OpenFOAM, which evaluates the shear stress at wall boundaries. Figure 41 shows a Fanning friction factor comparison between the “R” and the base case, using the “k-ωSST” model.

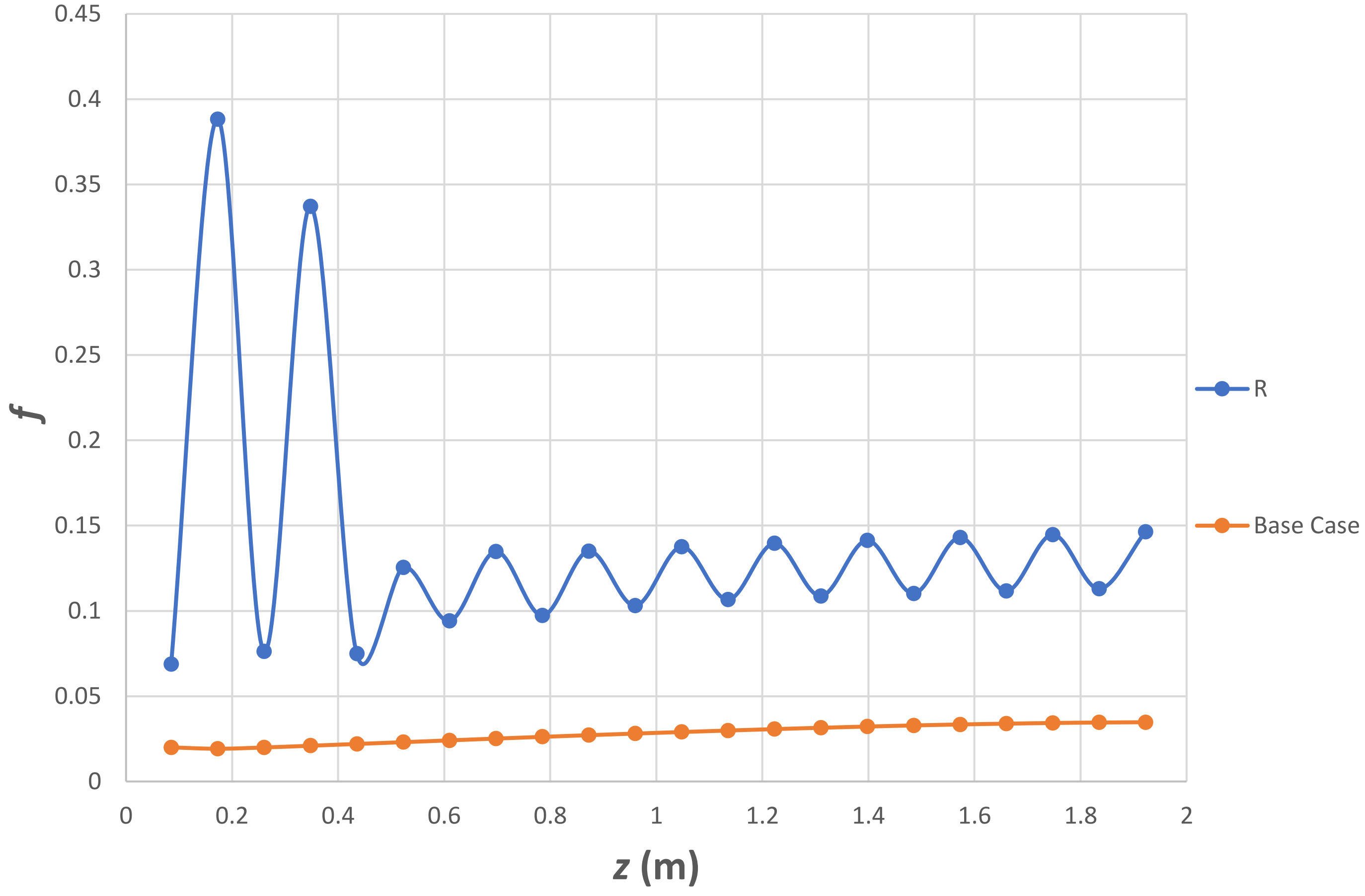

Figure 41: “R” case local Fanning friction factor comparison with base case using “k-ωSST”.

Similar to the local Nusselt number methodology, the local friction factor will be compared to the base case after the length of $L_{entrance} = 1\,m$, after which it is assumed that entrance effects are not present. It is evident in Figure 41 that the friction distribution shows an oscillatory behavior as a result of the ribs’ presence along the pipe, with local maxima referring to cross sections in the middle of each rib and local minima in the middle of the regions between two consecutive ribs. This is a result of the high velocities in the ribbed regions, leading to higher shear stresses compared to the regions between two consecutive ribs, where the fluid decelerates, as seen in Figure 42. Additionally, a global increase in friction is noted compared to the base case, as a result of the turbulence promotion, which leads to generation of vortices and higher mean axial velocity magnitudes, analogous to wall shear stress.

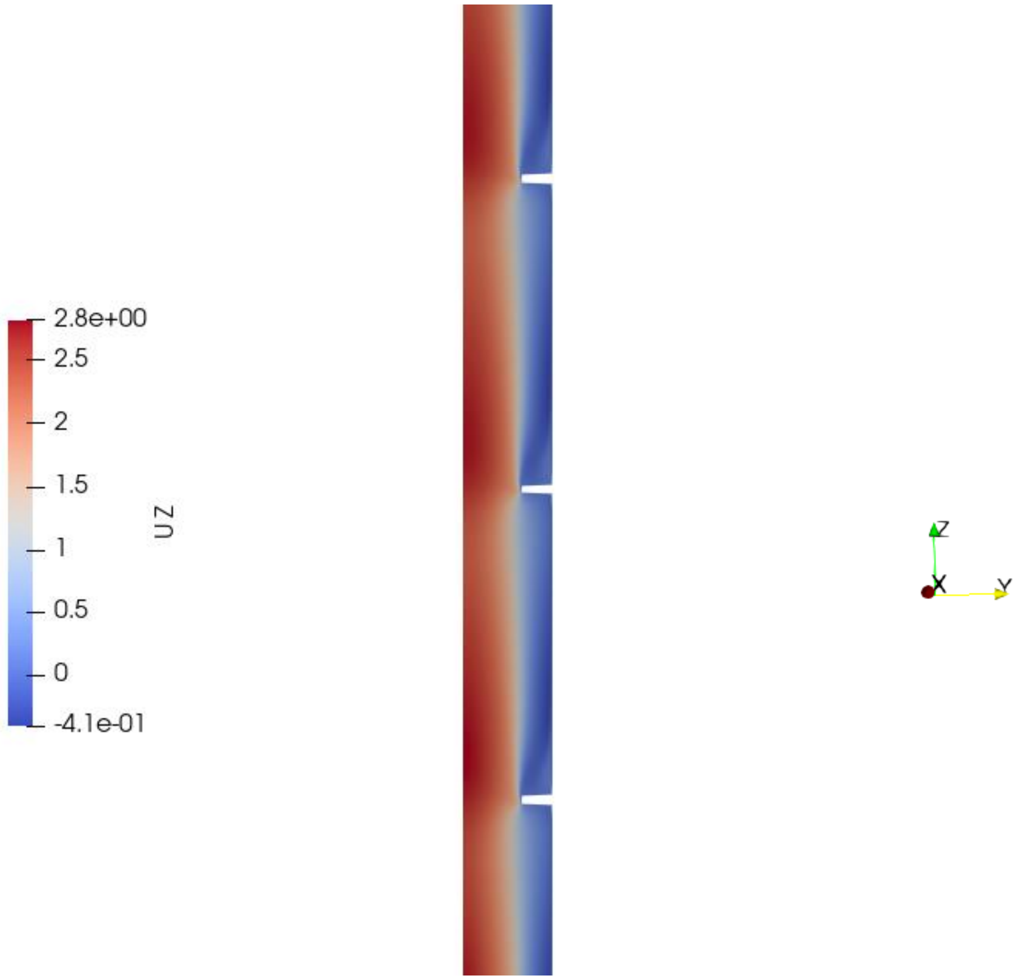

Figure 42: Mean axial velocity along the pipe for the R case.

Following the methodology of the investigation on heat transfer, the effect of varying p/D and e/D on friction is investigated, with results presented in Figures 43 and 44 respectively. Results shown in Figure 43 indicate that a higher pitch acts beneficially for friction, since Fanning friction factor values are lower for higher pitch-to-diameter ratios. On the other hand, as shown in Figure 44, a rib's depth is analogous to friction in the flow, with higher values obtained for higher depth-to-diameter ratios. As shown in the investigation of ribs' effect on heat transfer, promotion of turbulence is higher as ribs' depth increases, leading to the generation of vortices of greater size in the flow, with detrimental effect on friction, as explained in section 1.5.

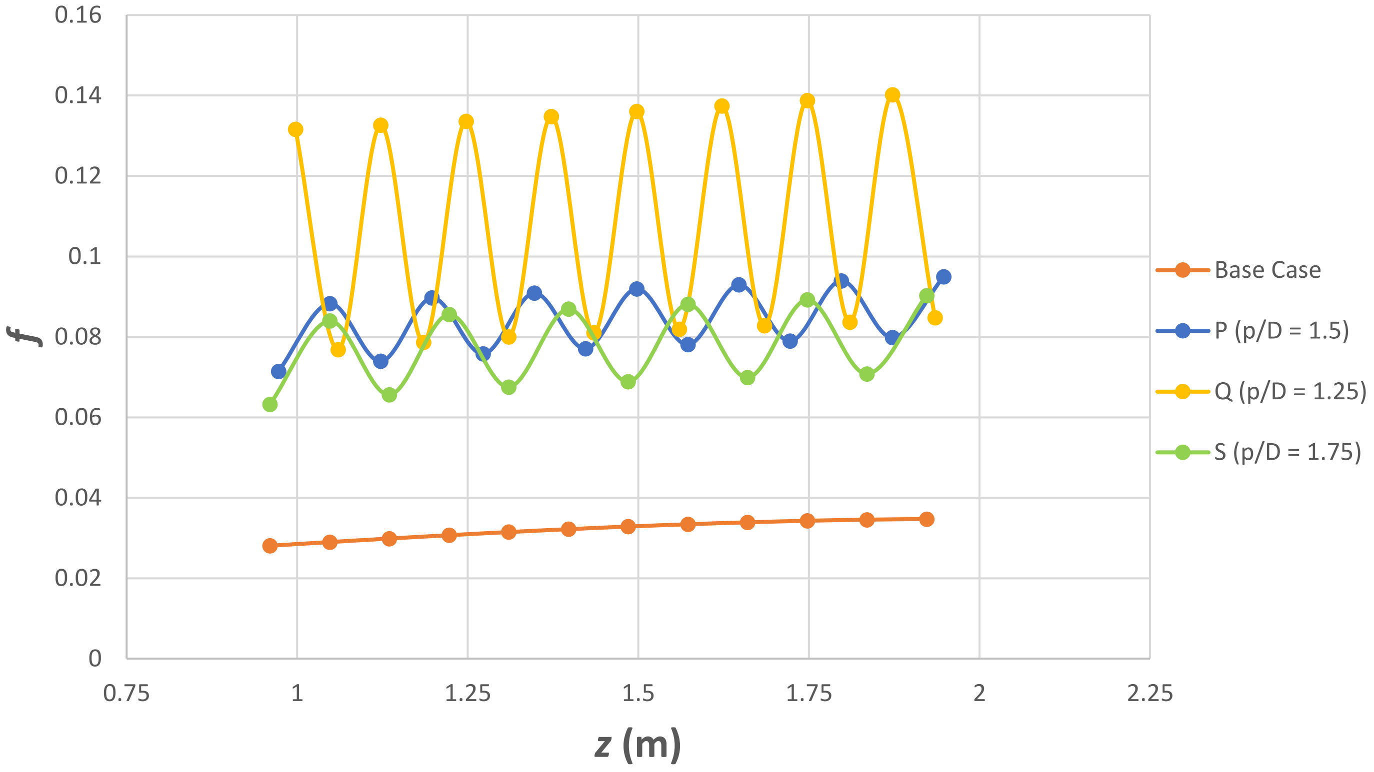

Figure 43: Rib pitch-to-diameter ratio effect on friction using "k-ωSST".

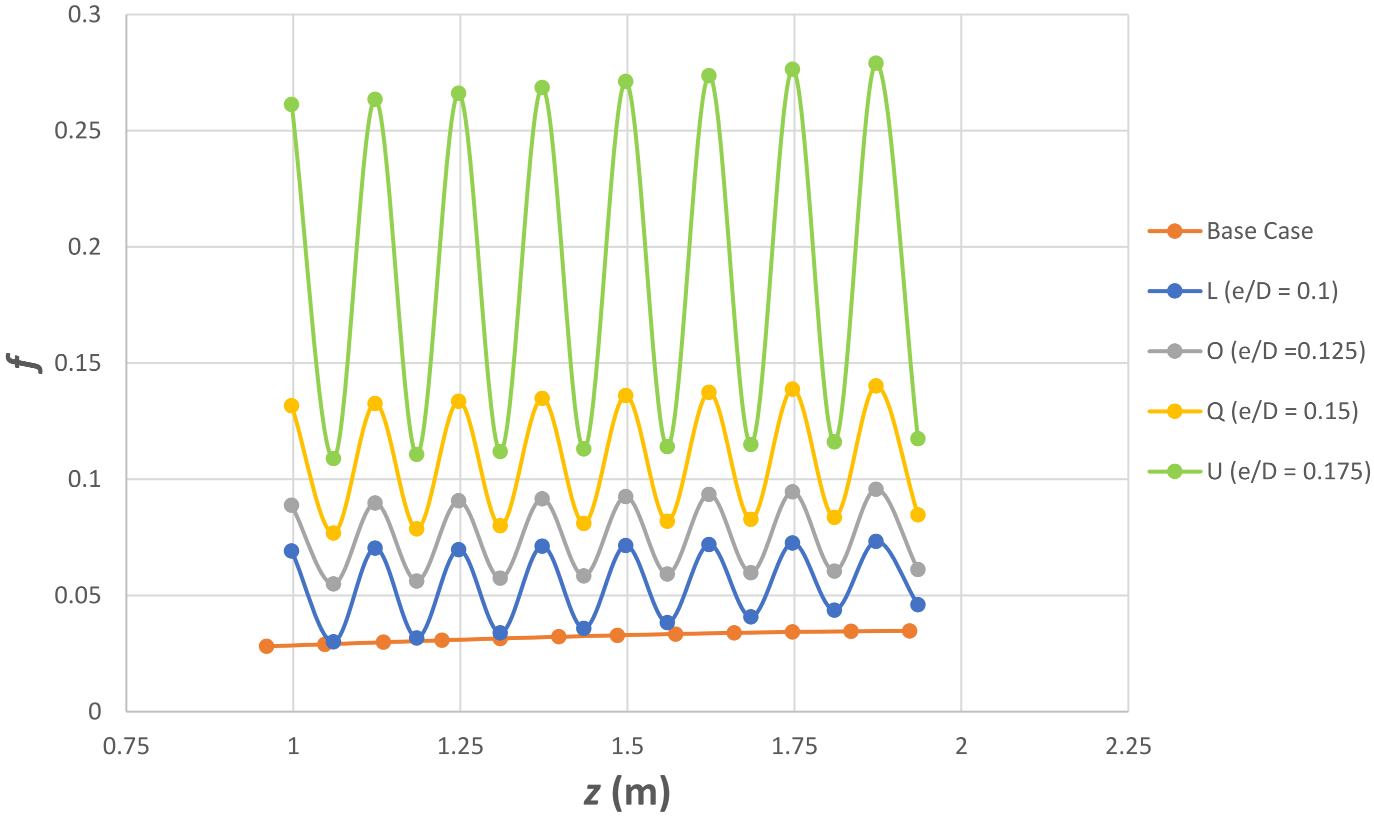

Figure 44: Rib depth-to-diameter ratio effect on friction using "k-ωSST".

6. Results: Spalart – Allmaras Turbulence Model

In this Chapter, the same methodology as in Chapter 5 is followed for the investigation on the effect of ribbed geometries on heat transfer and flow friction. The same cases are investigated, using *"SA"* instead of *"k-ωSST"* to model turbulence. Figures 45 and 46 compare mean axial velocity profiles and temperature distributions at z = 1.835 meters from the inlet for the "R" case, using both turbulence models, with $y = R - r$, with R referring to the pipe radius and r referring to the radial position of interest. High differences were the reason for investigating both turbulence models.

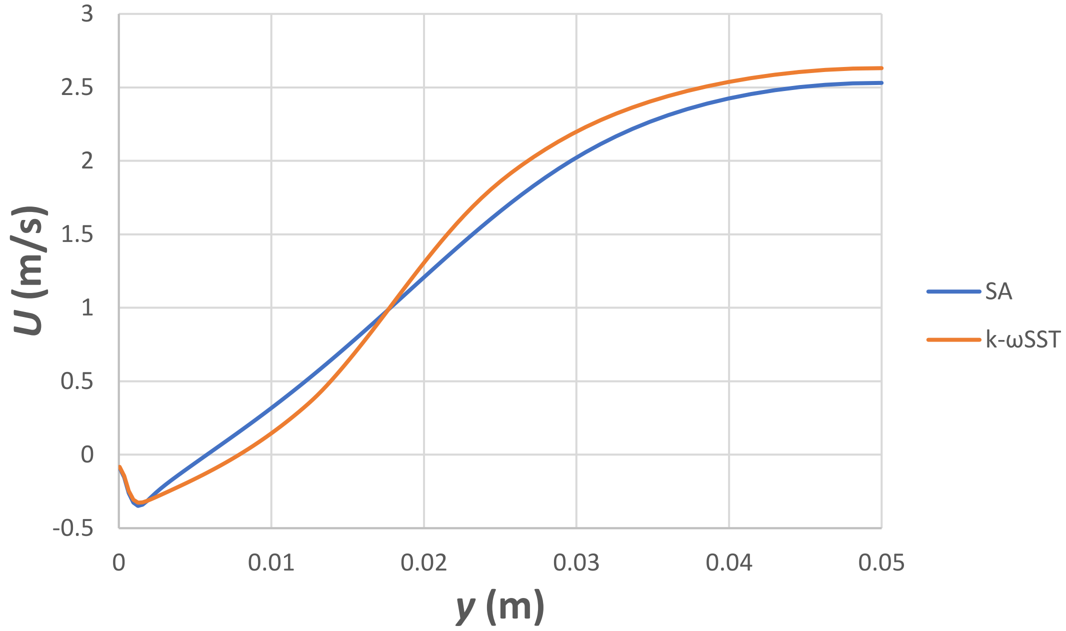

Figure 45: Mean axial velocity profiles comparison of case "R" for different turbulence models at z = 1.835 meters.

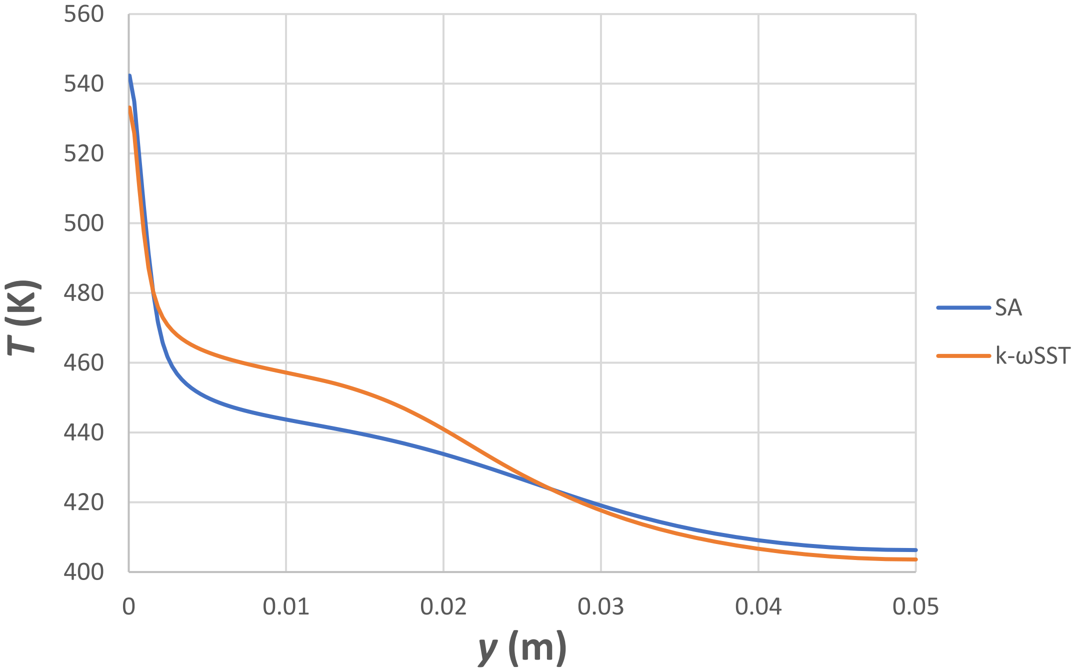

Figure 46: "R" case temperature distribution comparison for different turbulence models at z = 1.835 meters.

6.1 Heat Transfer

Results using *“SA”* turbulence model indicate a similar effect on heat transfer compared to the ones generated using *“k-ωSST”*. The effect of different pitch-to-diameter ratios is insignificant as shown in Figure 47. However, contrary to the *“k-ωSST”* results, smaller ratios result into slightly higher Nusselt numbers.

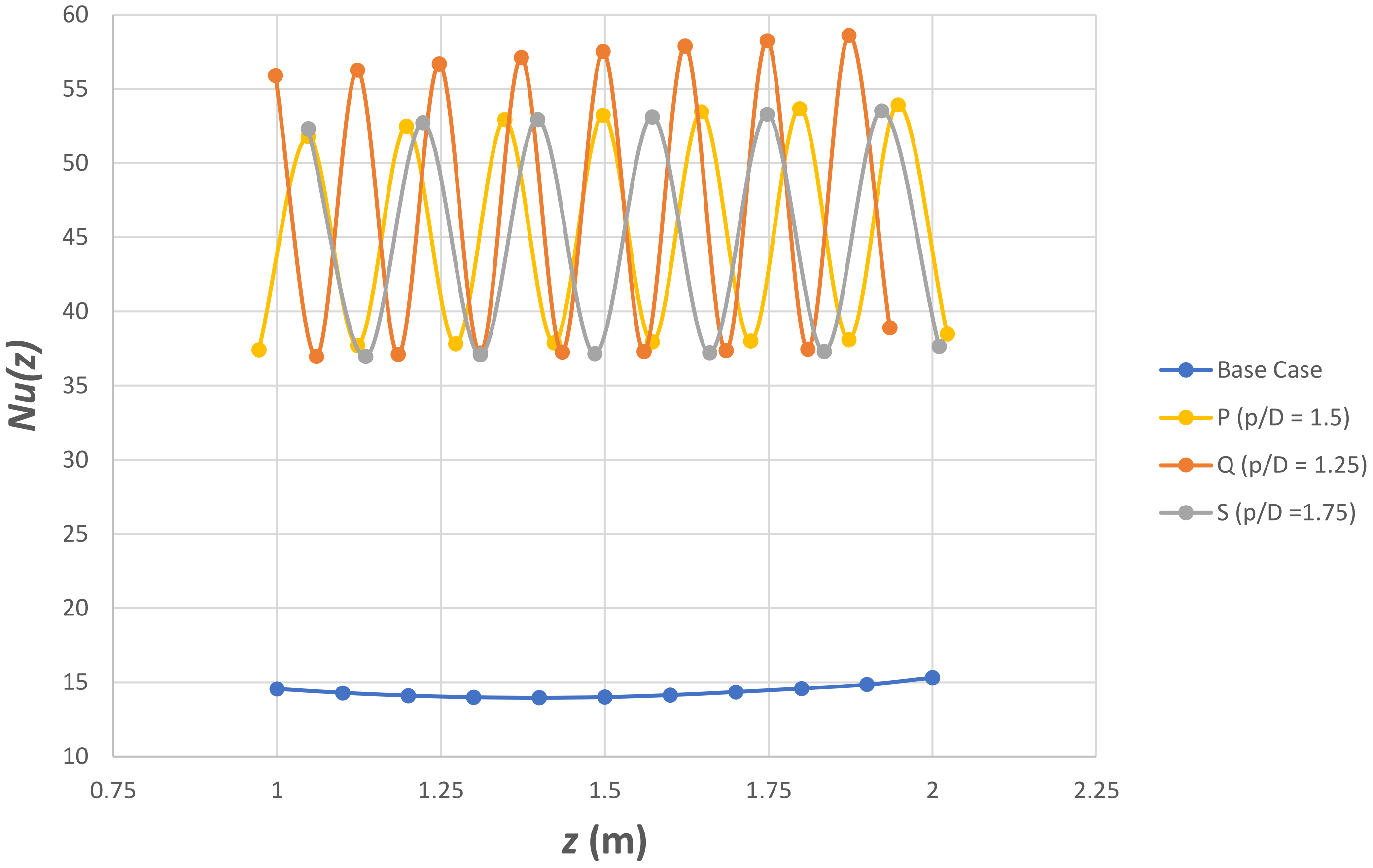

Figure 47: Rib pitch-to-diameter ratio effect on heat transfer using “SA”.

Heat transfer benefits from higher rib depths, similarly to the *“k-ωSST”* results. However, heat transfer shows less dependence on ribs’ depth variations using *“SA”* modelling, by comparing Figures 48 and 37.

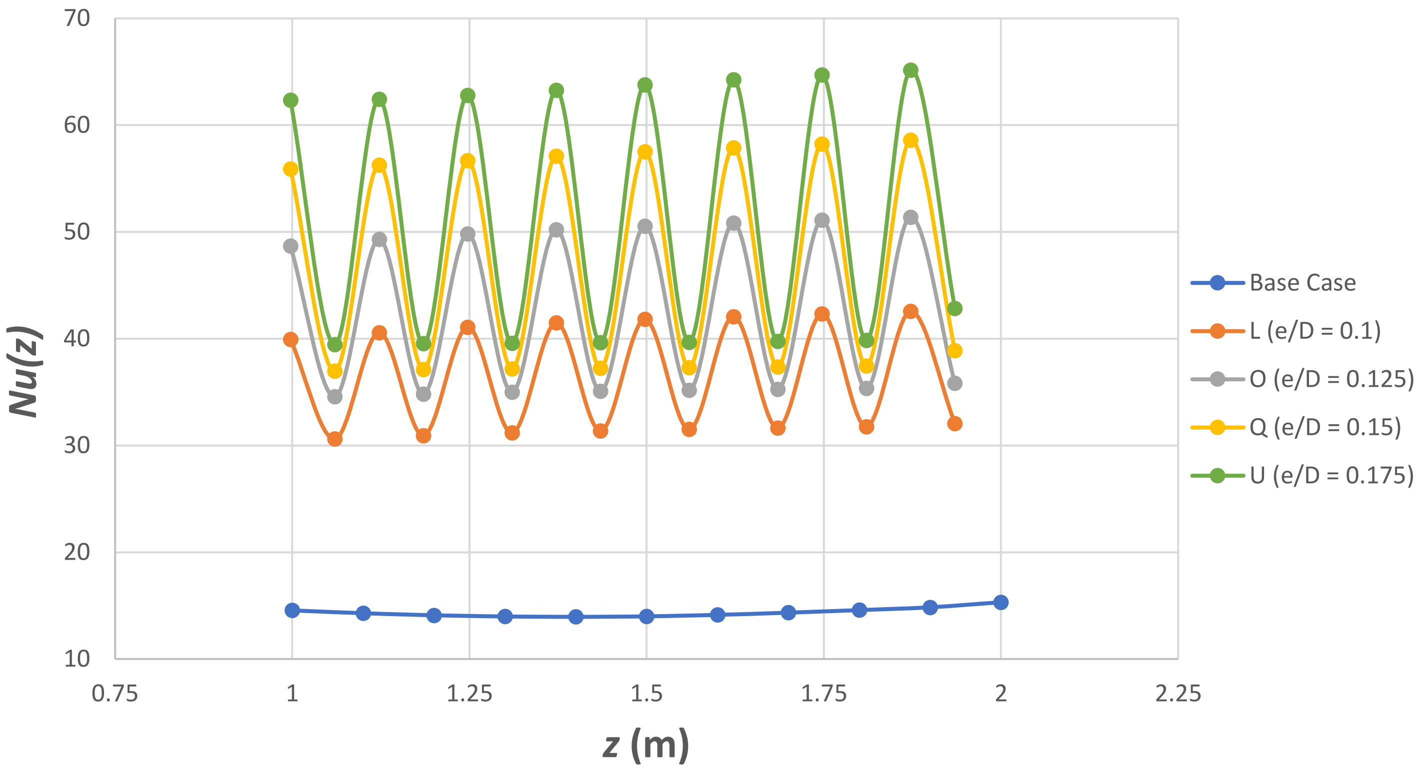

Figure 48: Rib depth-to-diameter ratio effect on heat transfer using "SA".

The effect of the ribs' depth on the flow structure is showing similar results using *"SA"* compared to the "k-ωSST" case, with increasing recirculation area for higher depths, as seen in Figure 49. The region depicted is the same as the region investigated in Chapter 5. Following the "SA" results, smaller recirculation regions are generated for each rib depth compared to the *"k-ωSST"* results.

A local Nusselt comparison is made for SA modelling in the region between two consecutive ribs. Results shown in Figure 50 are similar to the *"k-ωSST"* ones, with lower heat transfer coefficients close to the ribs and drastic enhancement when moving away from them. Comparing results for the two turbulence models, it is evident that the maximum of the local Nusselt number shifts towards the left side when using *"SA"* compared to the *"k-ωSST"* results. This could be attributed to the smaller recirculation area in the *"SA"* results, which is less effective at separating the flow from the heating wall, leading to lesser regions of deteriorated heat transfer and a more even Nusselt number distribution

Looking at the turbulent viscosity distribution at a line along the ribs' tip, shown in Figure 51, a more even distribution is noted in the case of *"SA"* modelling, suggesting a more uniform mixing in the region, which relates to the more uniform Nusselt number distribution. The maxima are shifted to the left, compared to *"k-ωSST"* modeling. However, the local Nusselt number maxima do not come in accordance with the maxima in the turbulent viscosity distribution, which was the case for *"k-ωSST"* modeling. A more detailed analysis needs to be performed for correlating the Nusselt distribution maxima with the recirculation area length scales.

For both turbulence models the promotion of turbulence and mixing is more significant compared to the detrimental effect of fluid recirculation on heat transfer. This can be justified by investigating the effect of ribs' depth on the modified turbulent viscosity, $\tilde{\nu}$, shown in Figure 51. Its drastic increase for increasing rib depths indicates their significantly beneficial effect on turbulence promotion and heat transfer.

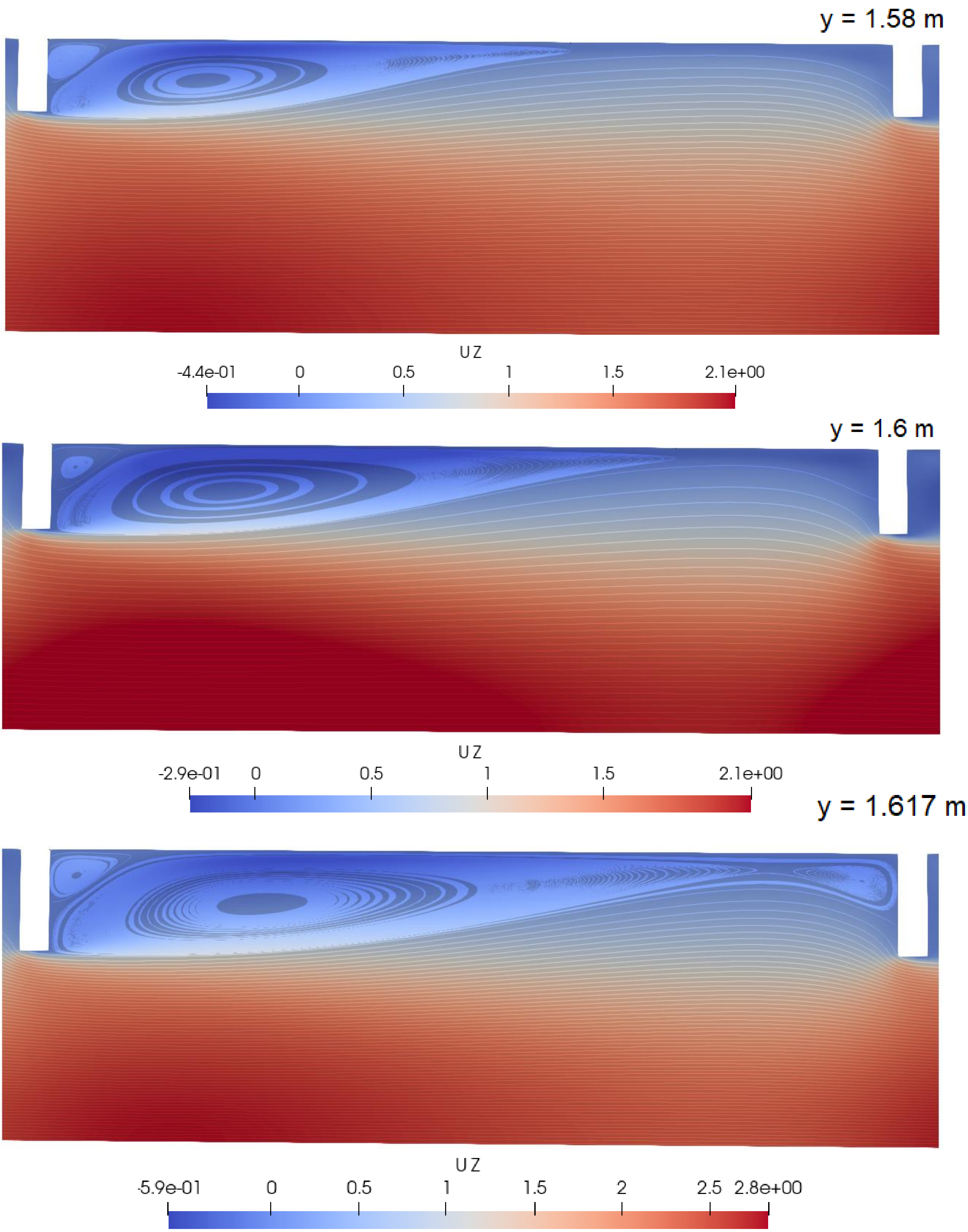

Figure 49: Streamlines, top to bottom: M (e/D = 0.125), P (e/D = 0.15), T (e/D = 0.175) using "SA".

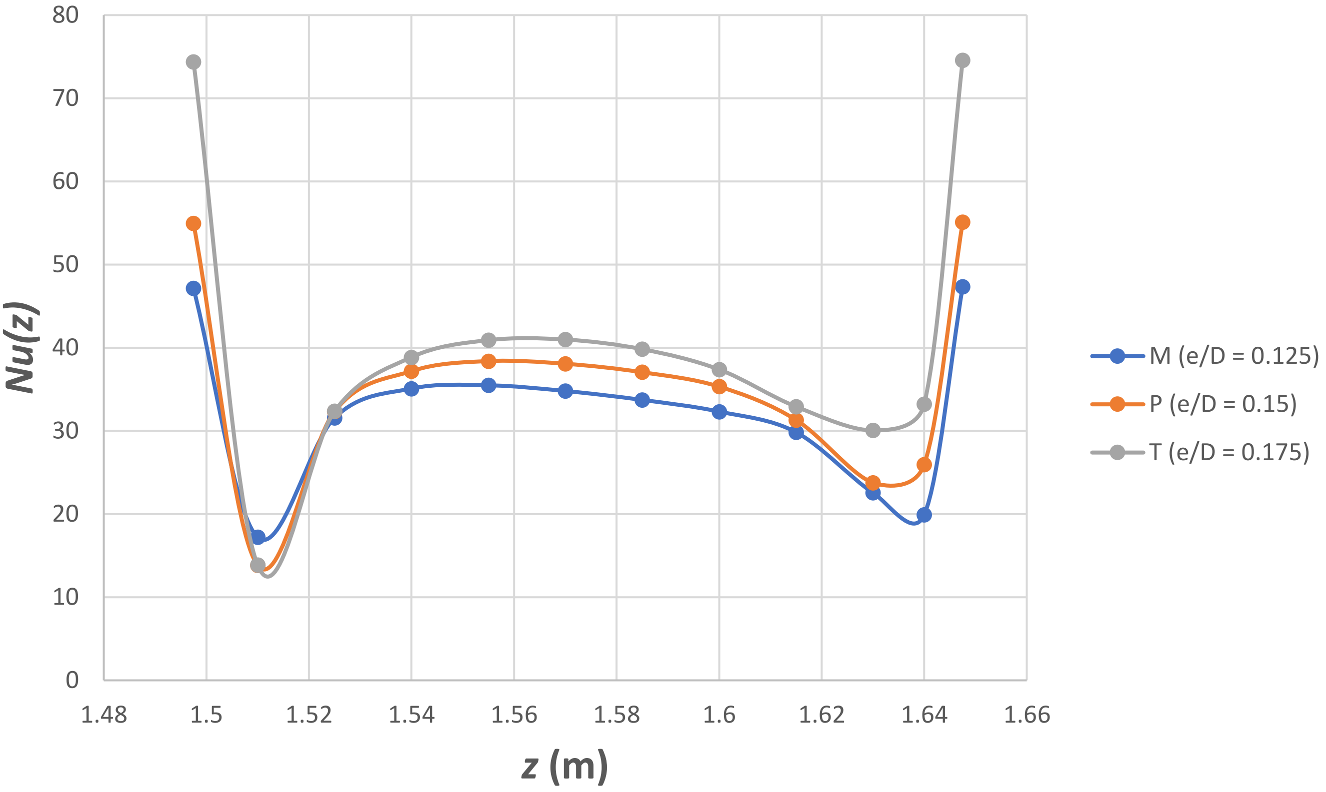

Figure 50: Local Nusselt number in the region between two ribs for different rib depths using "SA".

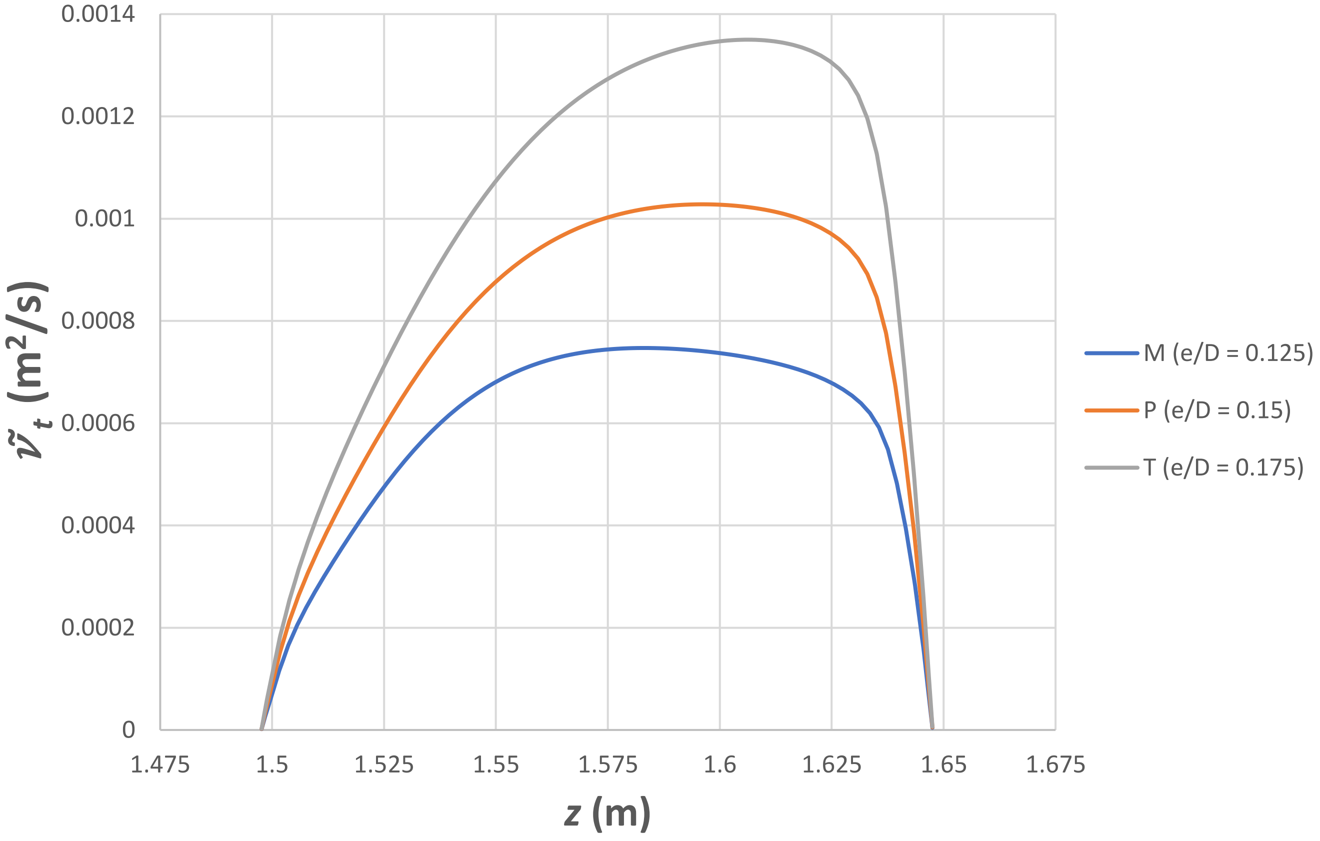

Figure 51: Modified turbulent viscosity along the center of the pipe for different ribs' depths using "SA".

6.2 Flow Friction

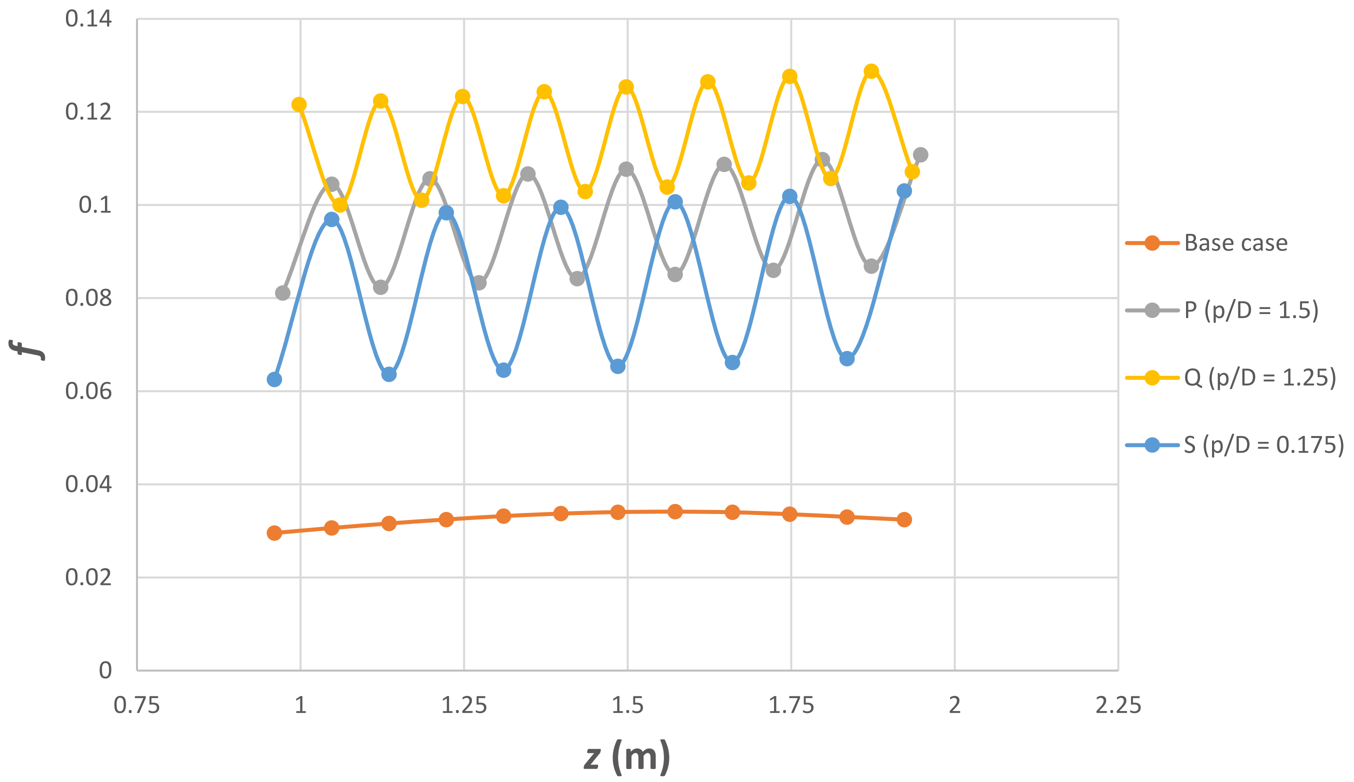

Figure 52: Rib pitch-to-diameter ratio effect on friction using "SA".

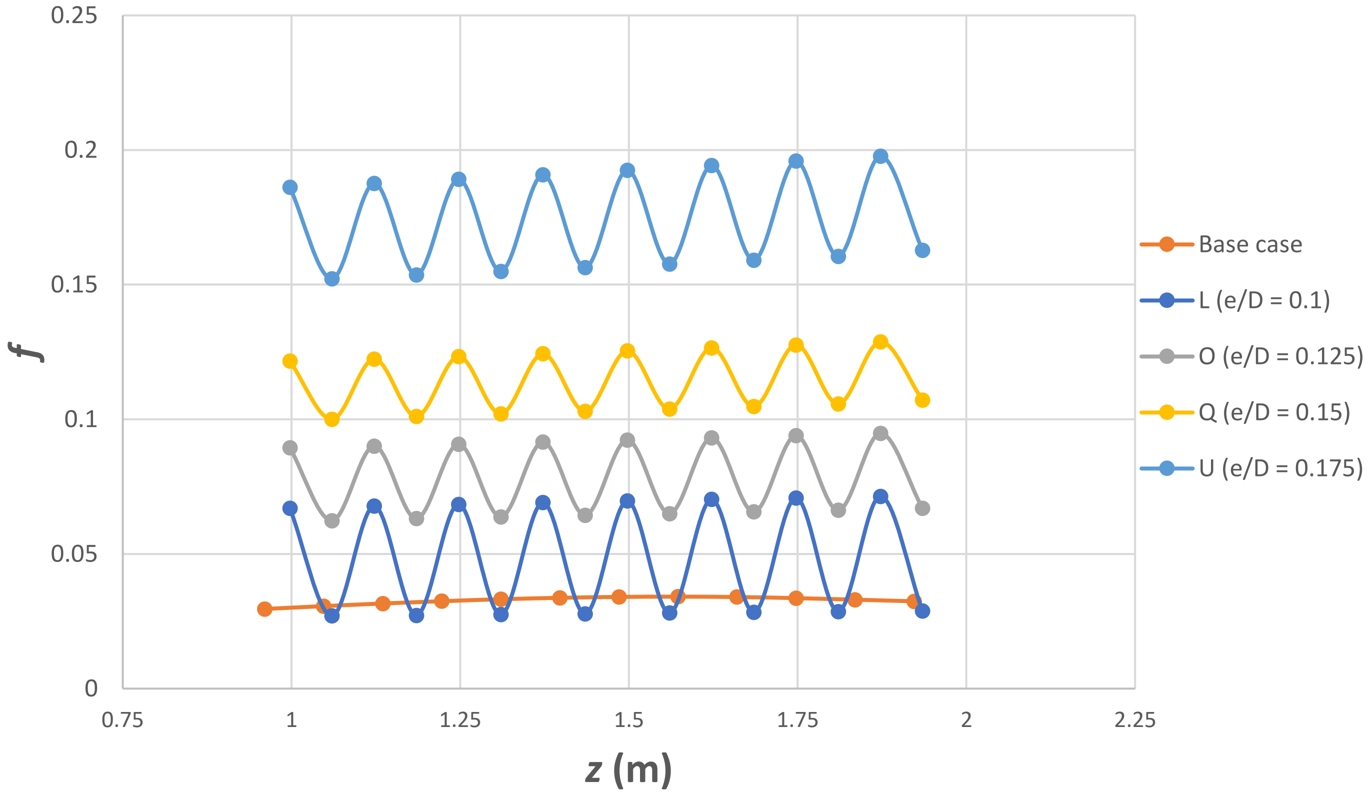

Figure 53: Rib depth-to-diameter ratio effect on friction using "SA".

An oscillatory behavior is shown in the results concerning the effect of ribbed surfaces on flow friction. Although there are certain differences in the values generated, resulting from differences in the generated temperature and velocity fields between the two turbulence models, the results are similar qualitatively. Higher pitch-to-diameter ratios are beneficial, since they result into lower friction factors, while increasing depth-to-diameter ratios lead to increasing friction in the flow.

A final remark on the *"SA"* results is summarized in Figure 54, in which the modified turbulent viscosity along the middle of the pipe of the "S" case is compared to the base case. It is easily noticed that turbulence and mixing is highly promoted by the presence of ribs.

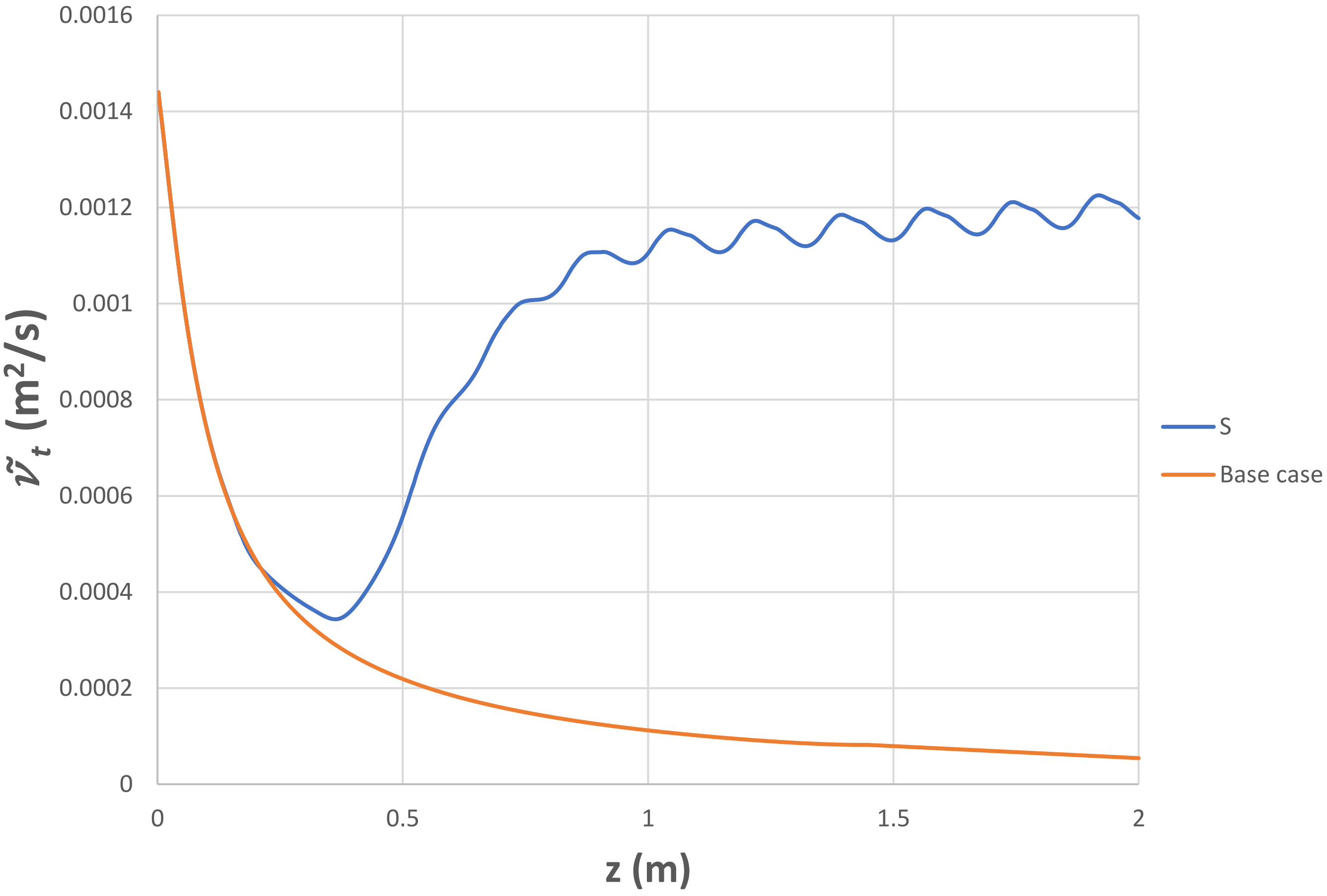

Figure 54: "S" case modified turbulent development along the pipe centerline using "SA".

7. Results: Performance Comparison

As mentioned in section 1.3, the performance of an artificially roughened surface is evaluated by the overall enhancement ratio η, with is the ratio of heat transfer enhancement to the increase in friction compared to the smooth surface, given by equation (1) as:

$$\eta = \frac{(Nu/Nu_0)}{(f/f_0)^{\frac{1}{3}}} \tag{1}$$

For the comparisons presented the average Nusselt number and friction factor values were used for the region starting at $L_{developed} = 1$ m.

Table 16: Overall performance using "k-ωSST".

Simulation Name	p/D	e/D	Nu/Nu_0	f/f_0	η
J	1.5	0.1	1.87	1.31	1.71
M	1.5	0.125	2.41	1.92	1.94
P	1.5	0.15	2.85	2.61	2.07
T	1.5	0.175	3.38	4.22	2.09
K	1	0.1	1.79	1.92	1.44
N	1	0.125	2.28	2.99	1.58
L	1.25	0.1	1.84	1.67	1.54
O	1.25	0.125	2.32	2.32	1.75
Q	1.25	0.15	2.74	3.34	1.83
U	1.25	0.175	3.21	5.9	1.77
V	1.75	0.1	1.88	1.16	1.79
S	1.75	0.15	2.95	2.40	2.20
R	1.75	0.175	3.33	3.90	2.11

Table 17: Overall performance using "SA".

Simulation Name	p/D	e/D	Nu/Nu_0	f/f_0	η
J	1.5	0.1	2.43	1.26	2.24
M	1.5	0.125	2.84	2.02	2.24
P	1.5	0.15	3.16	2.94	2.20
T	1.5	0.175	3.79	5.00	2.21
K	1	0.1	2.66	2.03	2.10
N	1	0.125	3.13	3.25	2.11
L	1.25	0.1	2.53	1.48	2.22
O	1.25	0.125	2.97	2.39	2.21
Q	1.25	0.15	3.29	3.49	2.17
U	1.25	0.175	3.6	5.33	2.06
V	1.75	0.1	2.36	1.15	2.26
S	1.75	0.15	3.13	2.53	2.30
R	1.75	0.175	3.55	4.40	2.16

Tables 18 and 19 include the performance evaluation of all the cases included in this work, using the “k-ωSST” and “SA” models respectively. Rows noted with a green color refer to the maximum overall enhancement ratio achieved with each model. It is important to note that the same case was calculated as the optimum using both turbulence models.

According to the results, a maximum overall enhancement ratio equal to $\eta = 2.2$ can be achieved among the cases tested, specifically under the conditions of case “S”, using “k-ωSST”. The same case is indicated as the optimum one using “SA”, reaching an overall enhancement ratio $\eta = 2.3$. In general, there is a higher variation in the overall enhancement ratios concerning “k-ωSST” modeling, a fact which can be attributed to the higher sensitivity of heat transfer on a varying ribs’ depth-to-diameter ratio, already discussed in Chapter 6.

8. Conclusions

Summing up, the numerical research presented in this report has been successful in answering the most important research questions set in the beginning of the project using two turbulence models. These are:

- **Can simple artificial roughness geometries promote turbulence and prevent laminarization, leading to enhanced heat transfer in mixed convection flows?**

The current research showed that simple artificial roughness geometries, in this case transverse rib geometries, can be beneficial for heat transfer in turbulent mixed convective flows by preventing laminarization. The turbulent kinetic energy and turbulent viscosity along the pipe were evidently enhanced by ribbed geometries, indicative of turbulence promotion. This led to higher Nusselt numbers, as shown in Chapters 5-7.

- **What is the effect of roughness elements' height and arrangement on heat transfer in turbulent mixed convection flows?**

Different rib pitch-to-diameter and depth-to-diameter ratios where tested for their effect on heat transfer, showing that the higher the ribs' depth the higher the heat transfer enhancement. On the other hand, the different pitch-to-diameters ratios tested did not appear to have a significant effect on heat transfer.

- **What is the cost in terms of momentum transfer and is the enhancement in heat transfer higher related to that?**

The negative effect of the ribs' presence on friction was investigated, leading to higher Fanning friction factor values for higher depths-to-diameter ratios. Higher pitch-to-diameter ratios on the other hand resulted into less friction. Using the overall enhancement ratio as a criterion, the study showed that the transverse rib geometries can promote heat transfer on a greater scale, compared to the increase in friction. It is important to note, that both turbulence models tested predicted the same geometry as the optimum based on the overall enhancement ratio.

Further Research

Even though some important research questions were answered in this project, there are additional important areas that are recommended for further research:

- The effect of transverse rib geometries on turbulent mixed convective flows for different wall heating rates.
- A more detailed investigation needs to be carried out focusing on correlating flow structures generated by different geometries and their effect on heat transfer.
- The effect of transverse rib geometries on turbulent mixed convective flows for different Reynolds numbers.
- The effect of additional pitch-to-diameter and depth-to-diameter ratios on turbulent mixed convective flows.
- The effect of different artifcial roughness geometries, as dimpled surfaces, on turbulent mixed convective flows.
- Research should be conducted performing LES or DNS for more accurate results.

9. Epilogue

This project has been highly valuable personally, in understanding the basics of performing scientific research in engineering applications using numerical tools. Important skills have been developed which are vital for the development as an engineer by overcoming difficulties. These include, getting familiar with performing CFD simulations using OpenFOAM, a very important tool for CFD engineers globally, understanding and analyzing the most important aspects of turbulence, extremely important in real life engineering applications, and getting familiar with ways of promoting heat transfer in flows found in important engineering applications. All in all, this has been the most important project, individually, for setting the basis for the future engineering career.

Appendix: Shehata et. al [65] validation figures

All the figures included in the validation of the turbulent case are included in this section, offering a complete view of the process. Distances from the inlet are indicated in the figure captions by a number, e.g., “14.2”, meaning $14.2 \times D = 0.39\ (m)$ from the tube inlet. Results are shown against $y = R - r$, with R referring to the pipe radius and r referring to the radial position of interest.

Temperature Distribution

Run 618

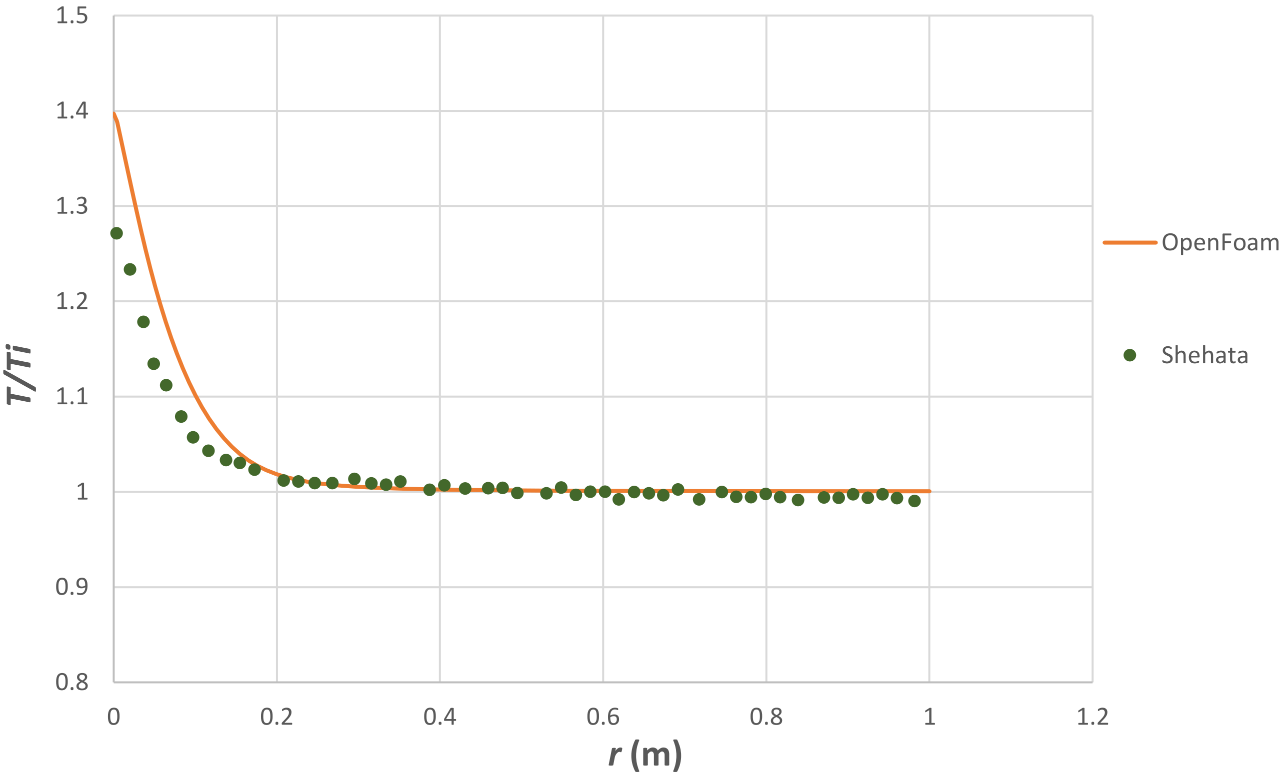

Figure A.1: 3.2 temperature distribution of Run 618.

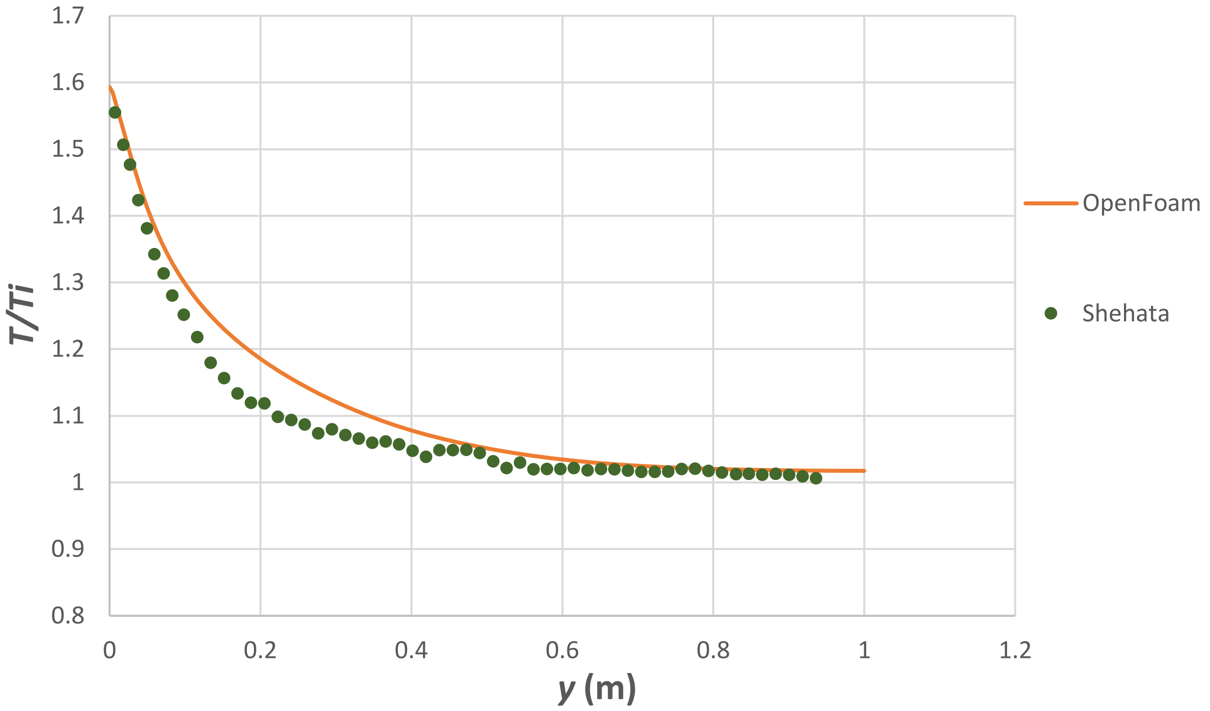

Figure A.2: 14.2 temperature distribution of Run 618.

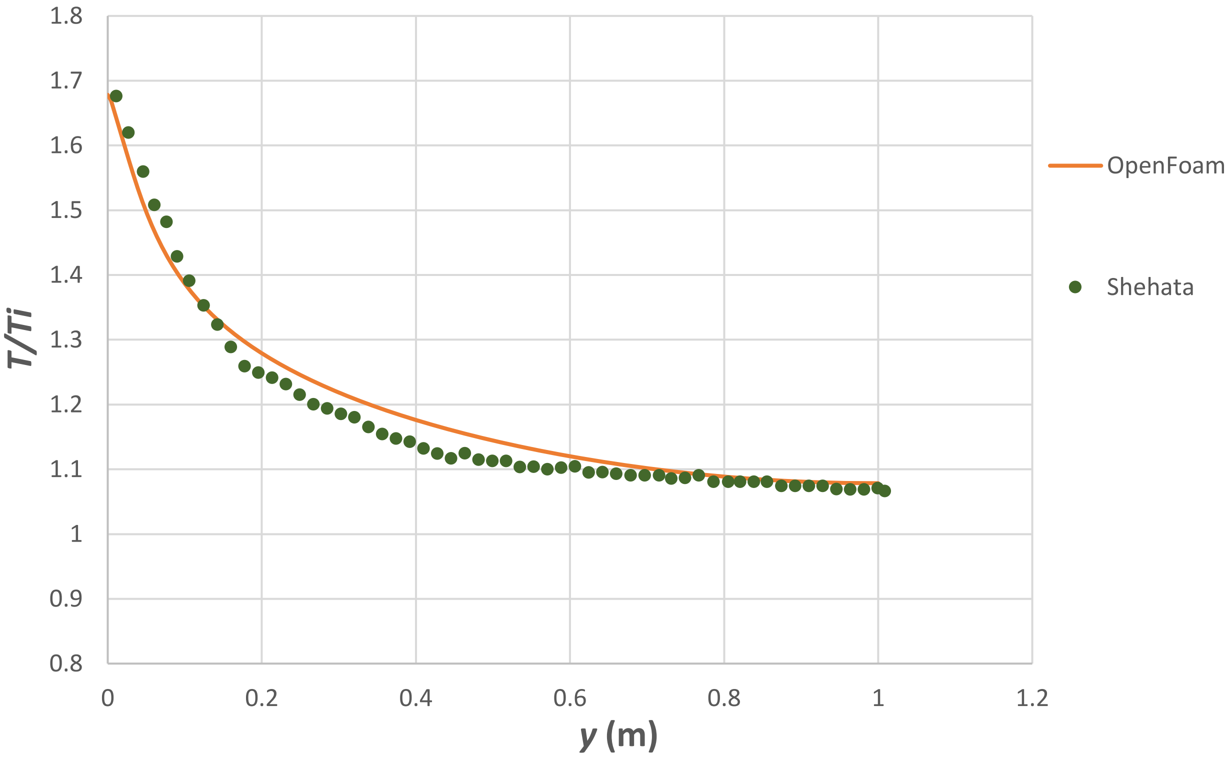

Figure A.3: 24.5 temperature distribution of Run 618.

Run 635

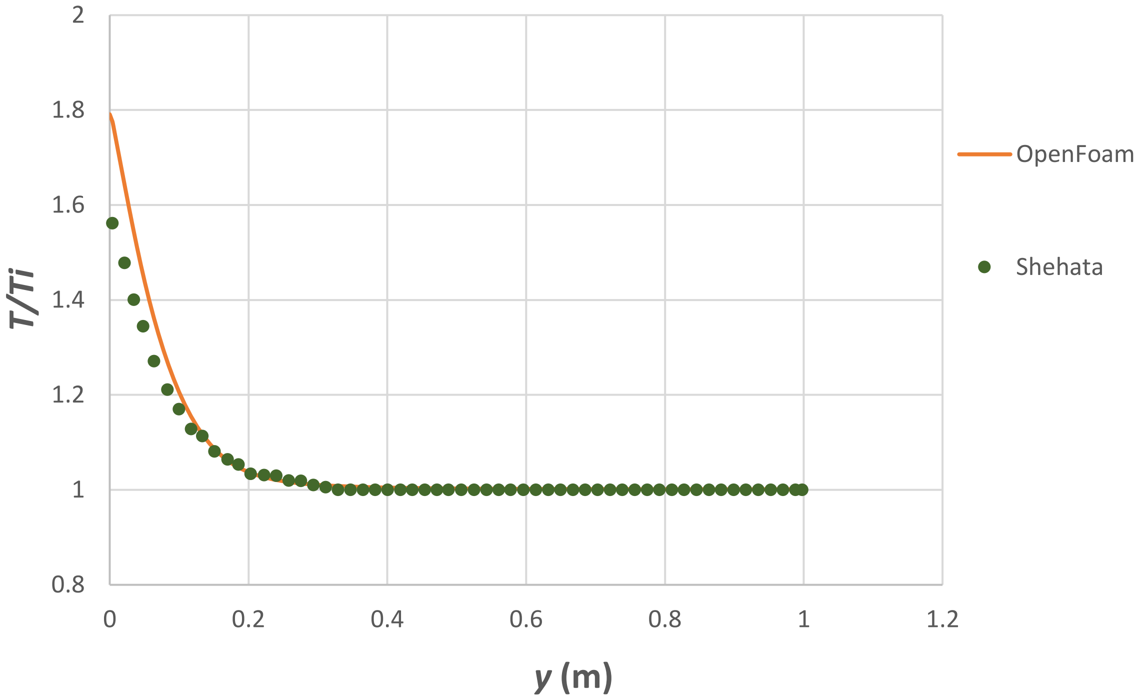

Figure A.4: 3.2 temperature distribution of Run 635.

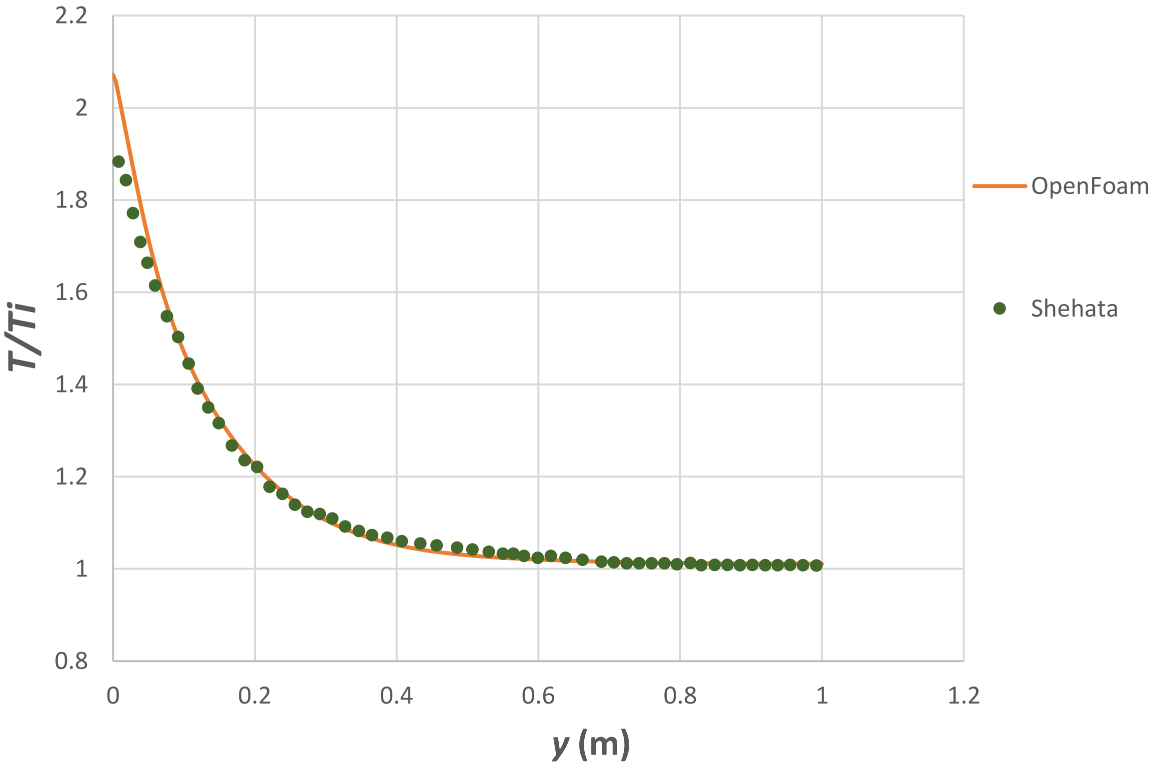

Figure A.5: 8.7 temperature distribution of Run 635.

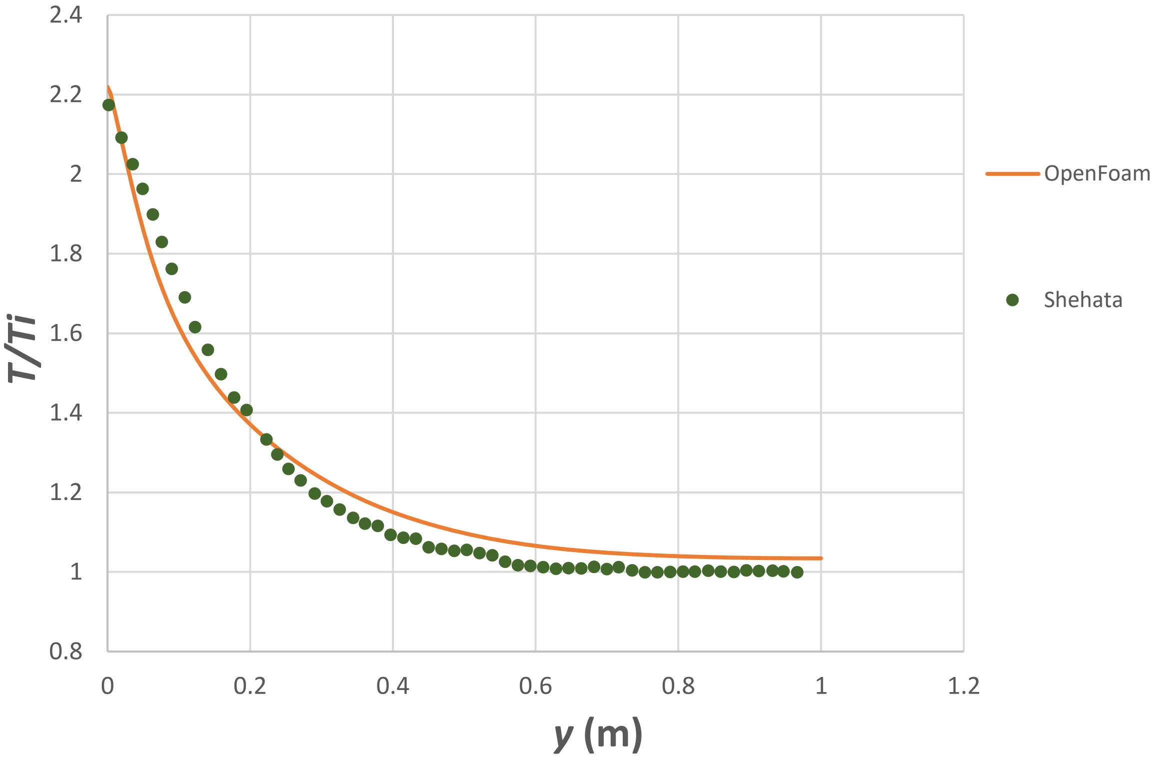

Figure A.6: 14.2 temperature distribution of Run 635.

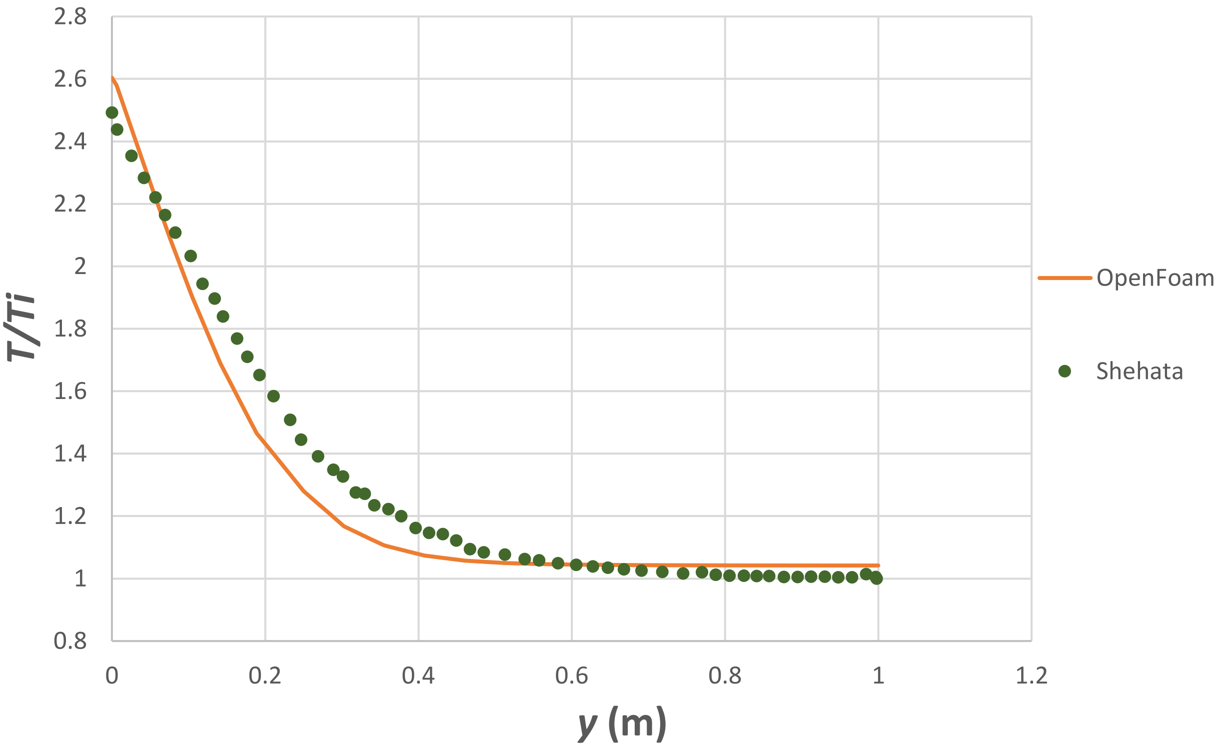

Figure A.7: 19.9 temperature distribution of Run 635.

Run 445

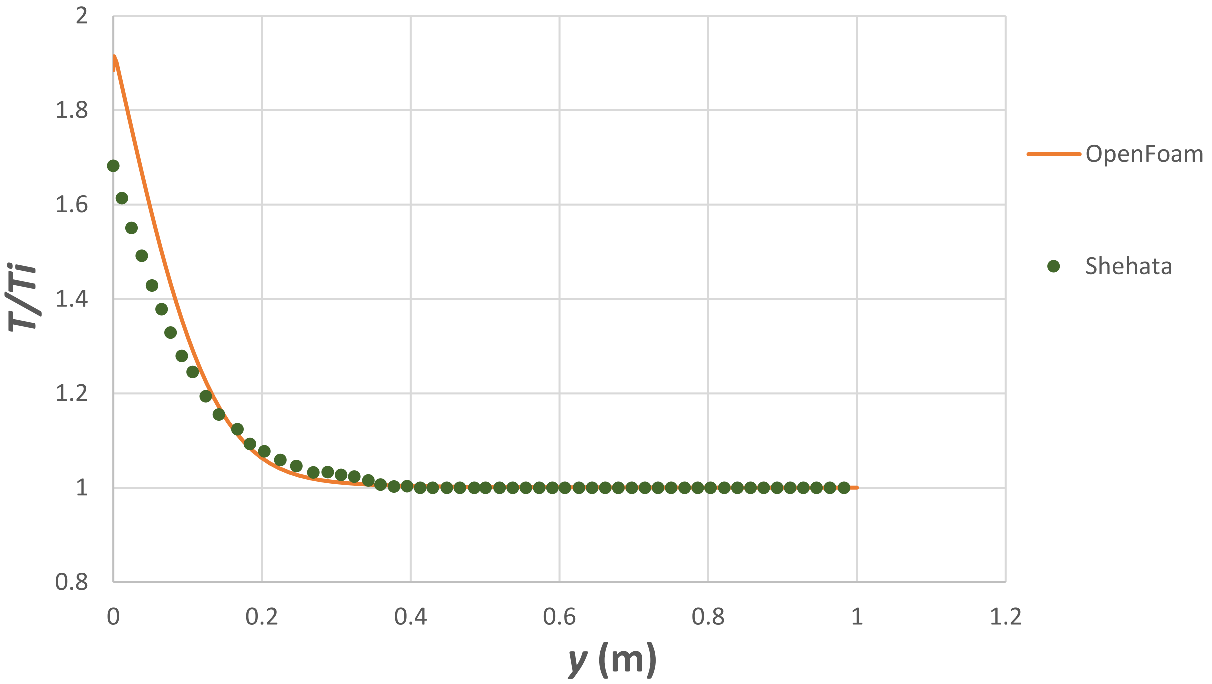

Figure A.8: 3.2 temperature distribution of Run 445.

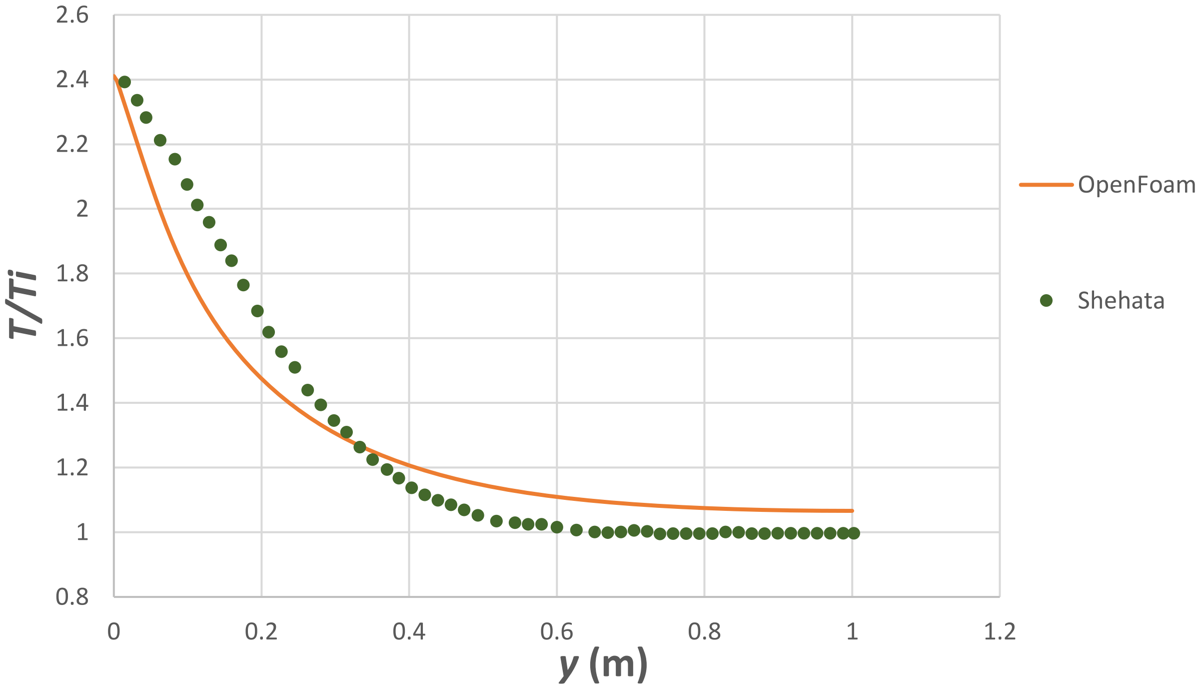

Figure A.9: 14.2 temperature distribution of Run 445.

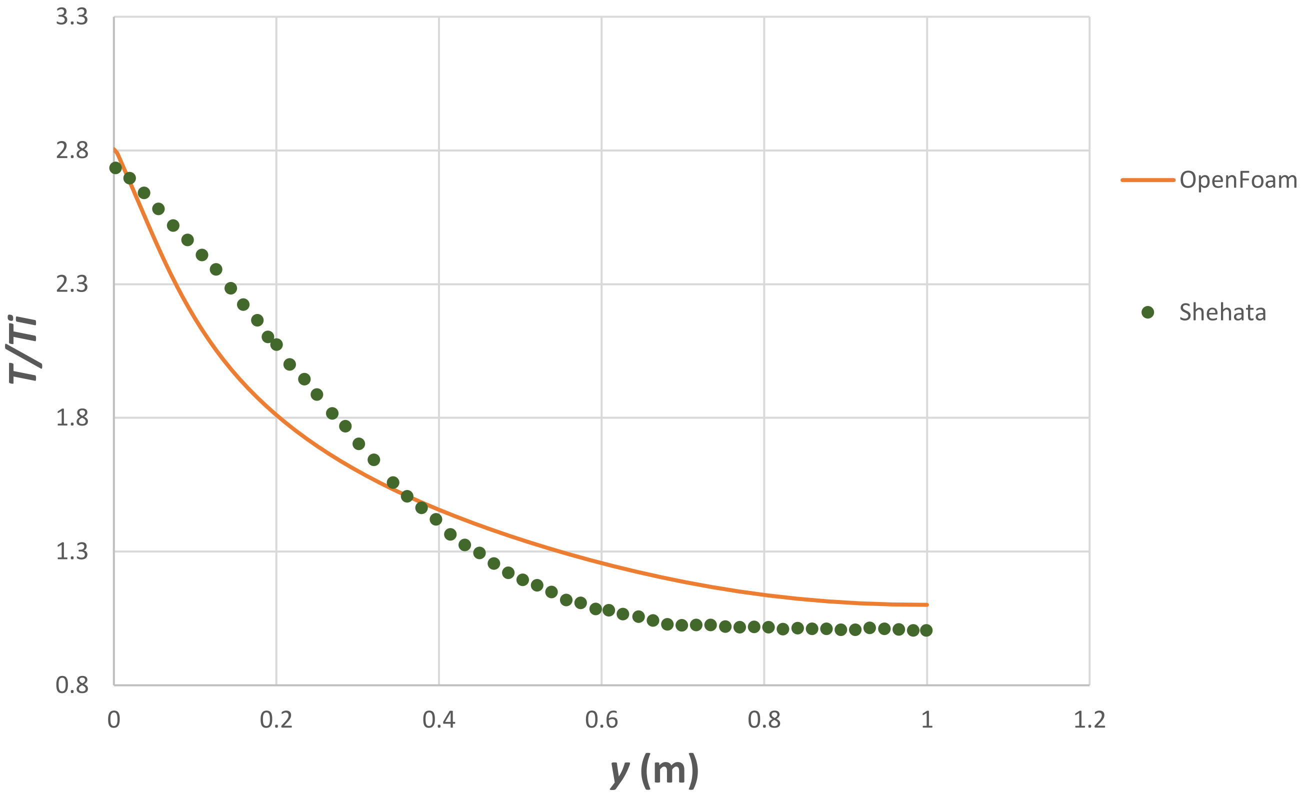

Figure A.10: 24.5 temperature distribution of Run 445.

Mean Axial Velocity Profiles

Run 618

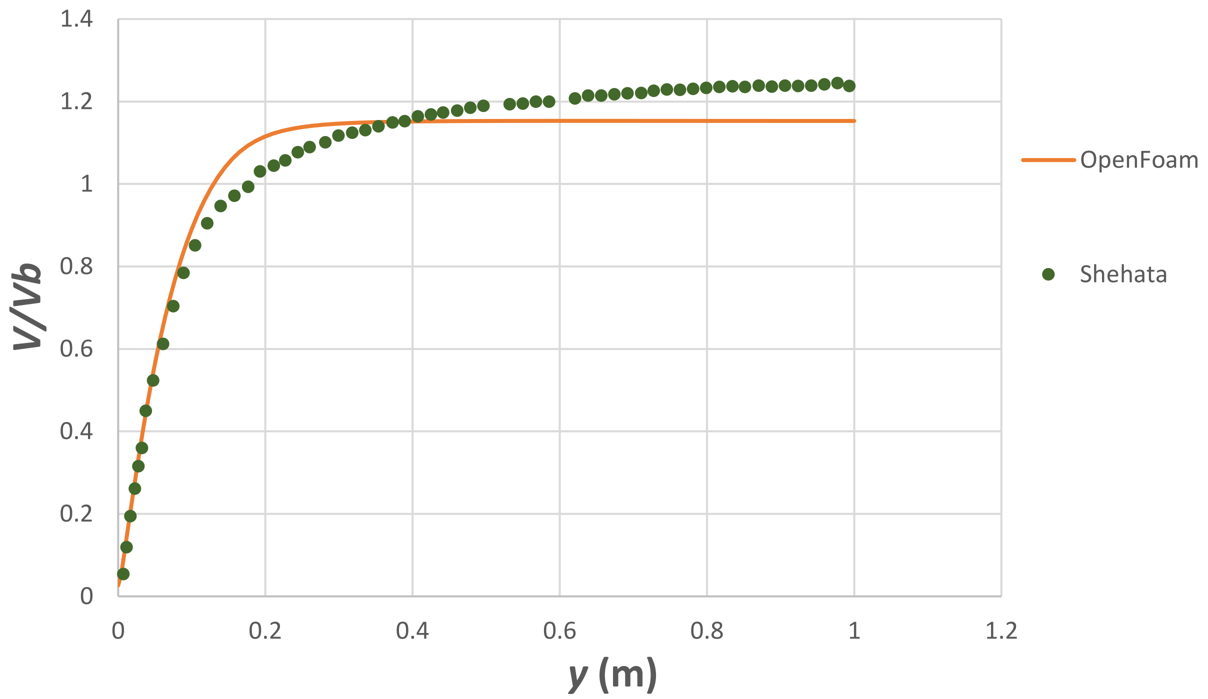

Figure A.11: 3.2 mean axial velocity profile of Run 618.

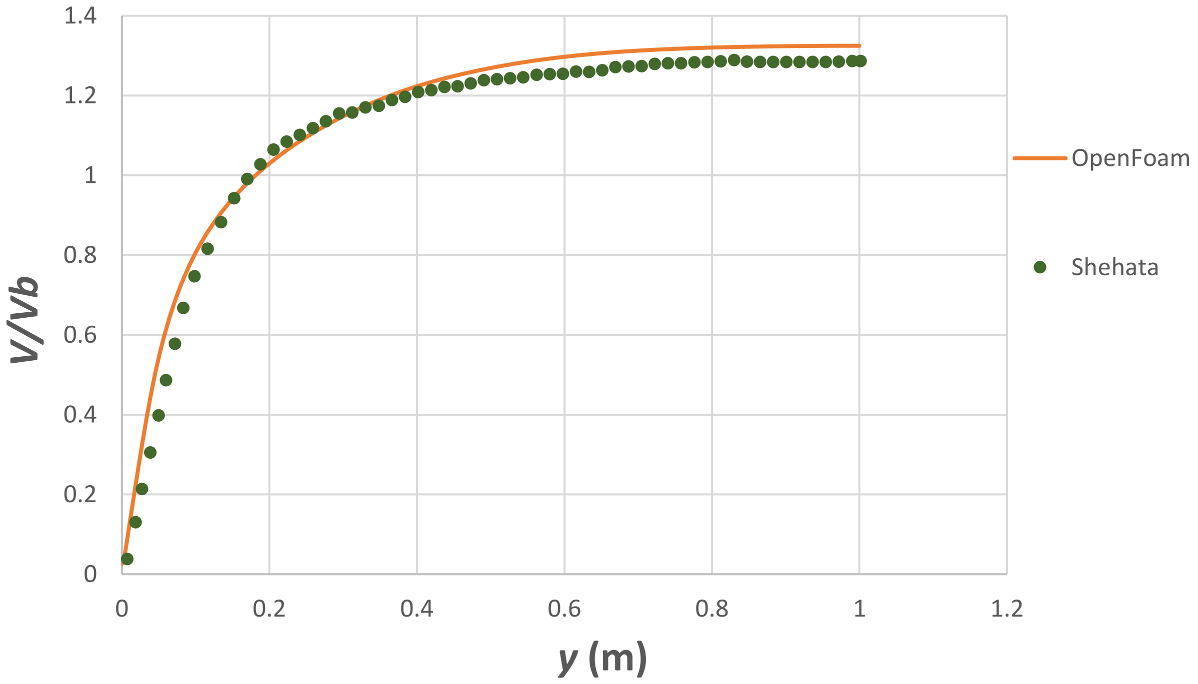

Figure A.12: 14.2 mean axial velocity profile of Run 618.

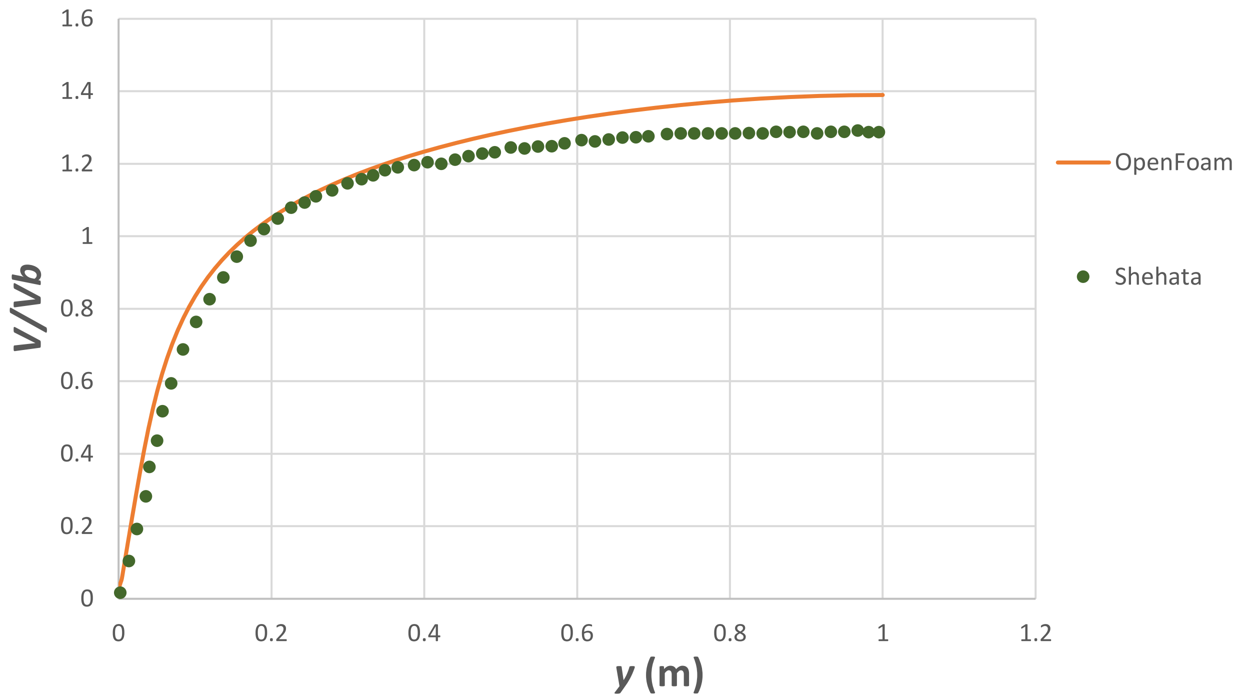

Figure A.13: 24.5 mean axial velocity profile of Run 618.

Run 635

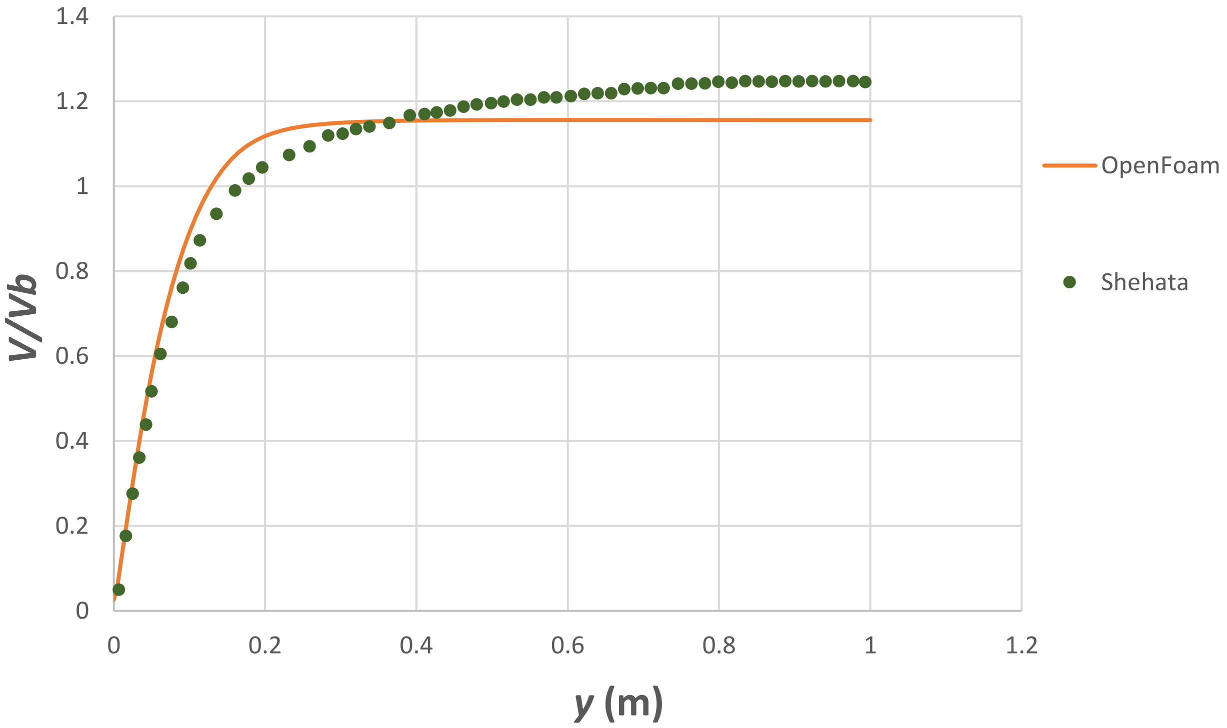

Figure A.14: 3.2 mean axial velocity profile of Run 635.

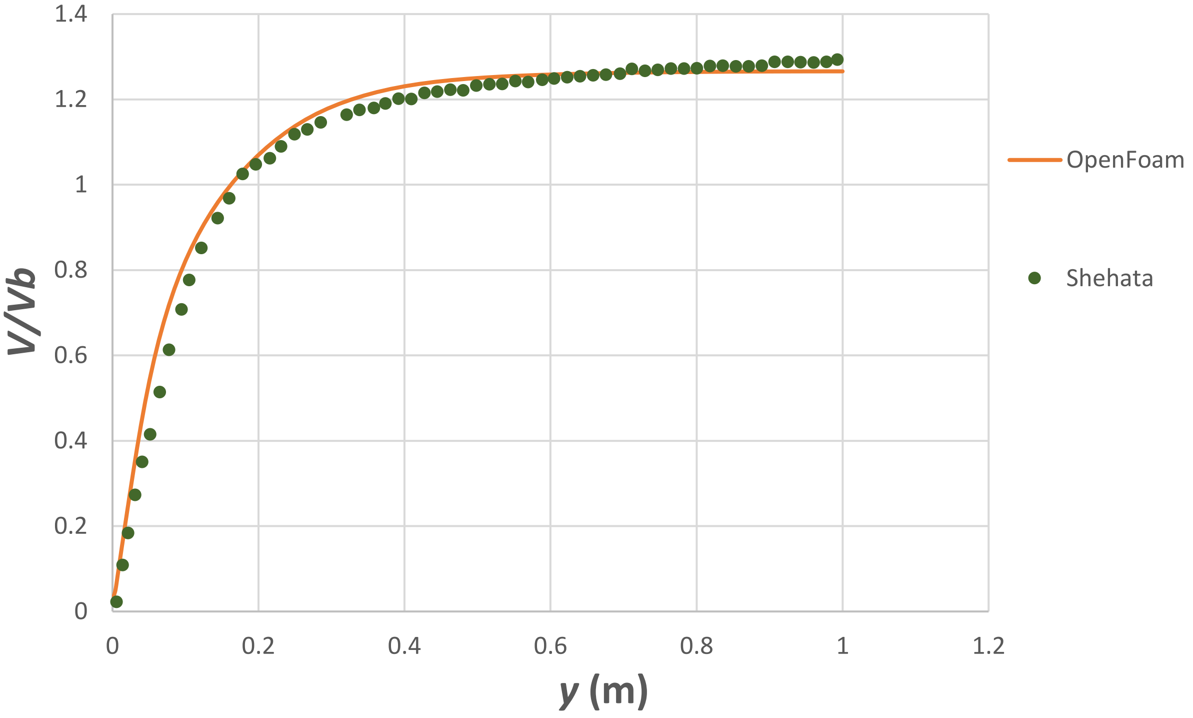

Figure A.15: 8.7 mean axial velocity profile of Run 635.

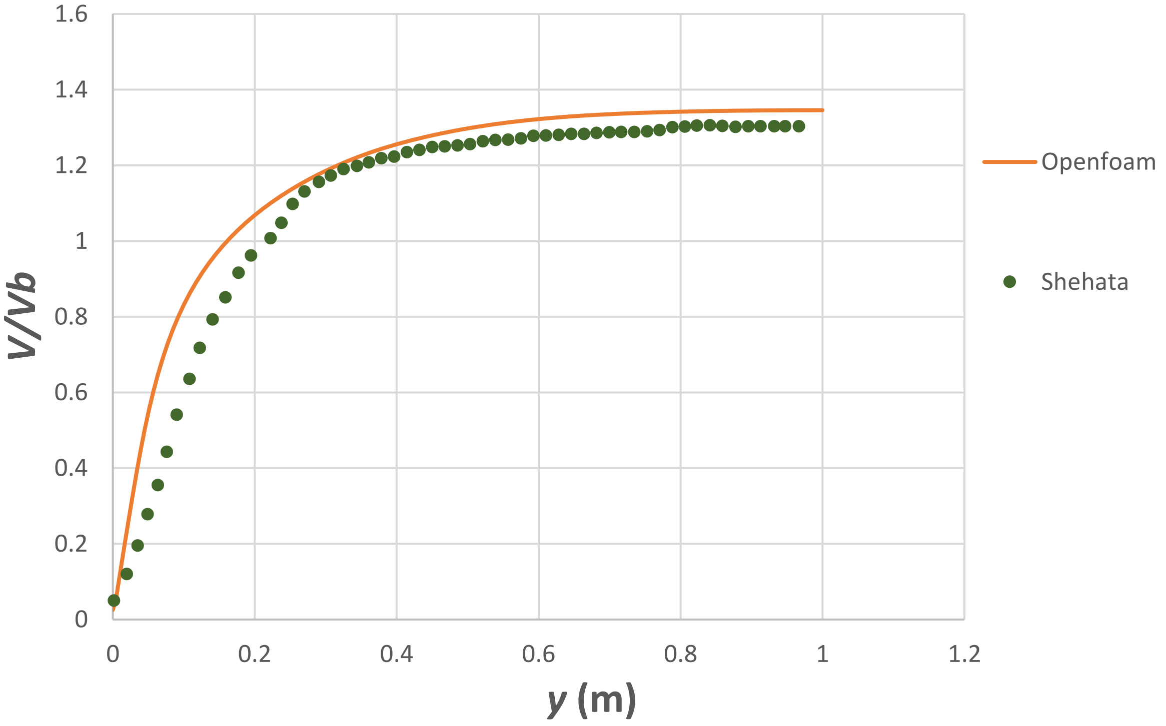

Figure A.16: 14.2 mean axial velocity profile of Run 635.

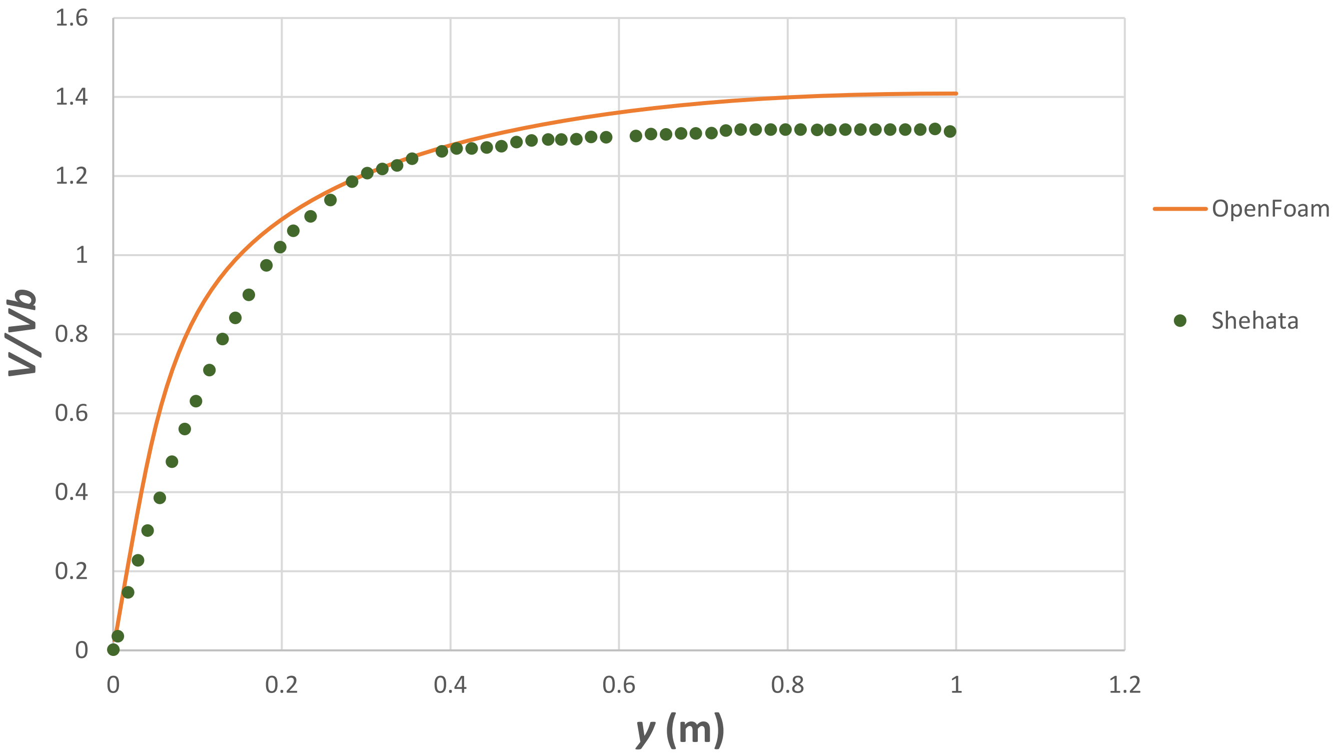

Figure A.17: 19.9 mean axial velocity profile of Run 635.

Run 445

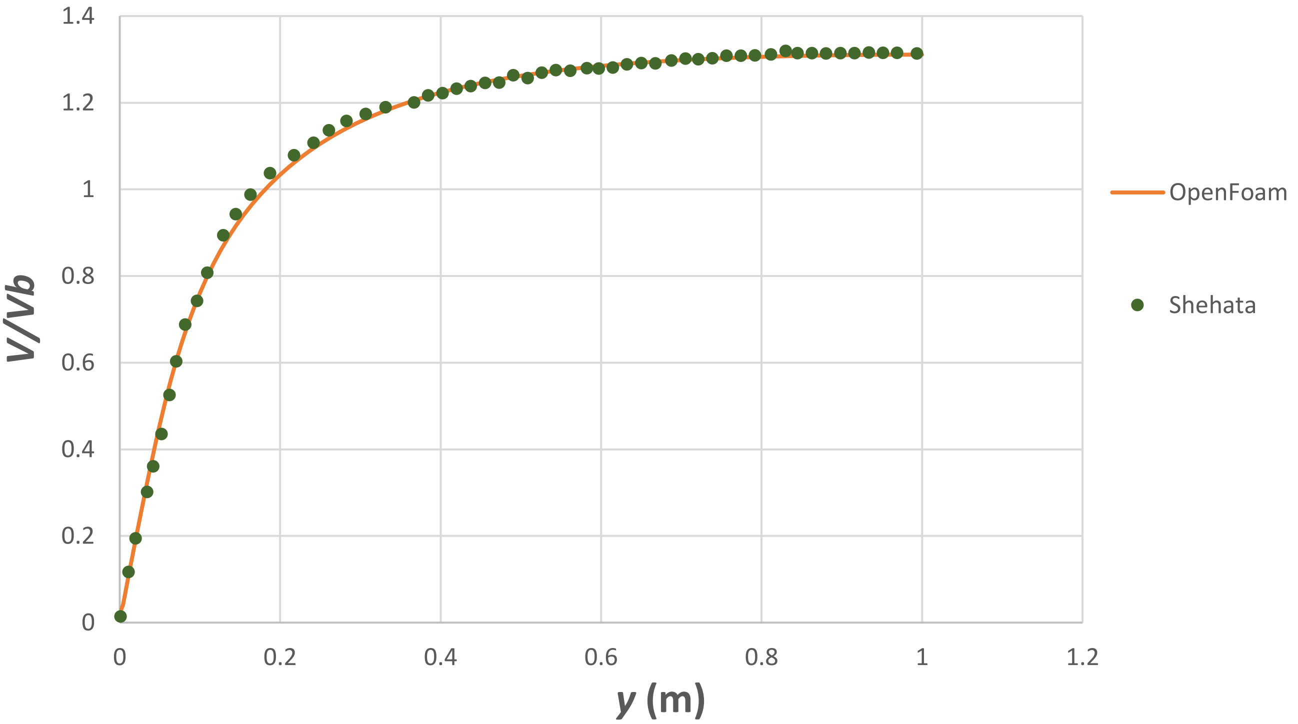

Figure A.18: 3.2 mean axial velocity profile of Run 445.

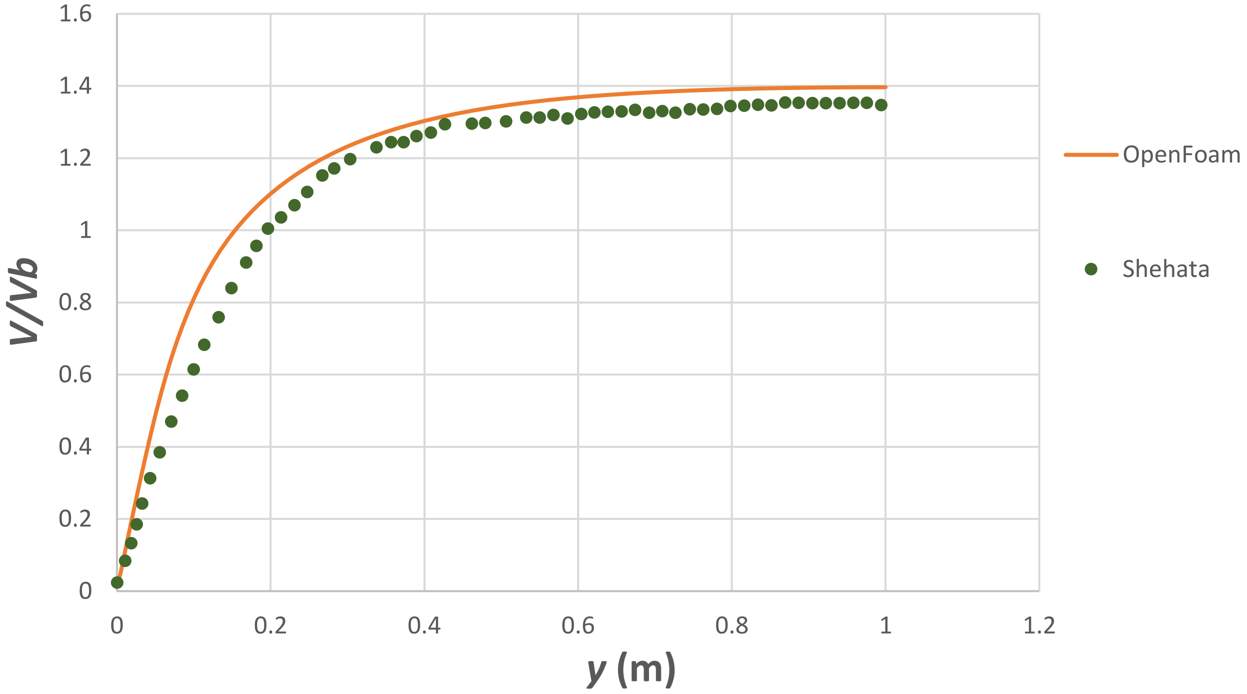

Figure A.19: 14.2 mean axial velocity profile of Run 445.

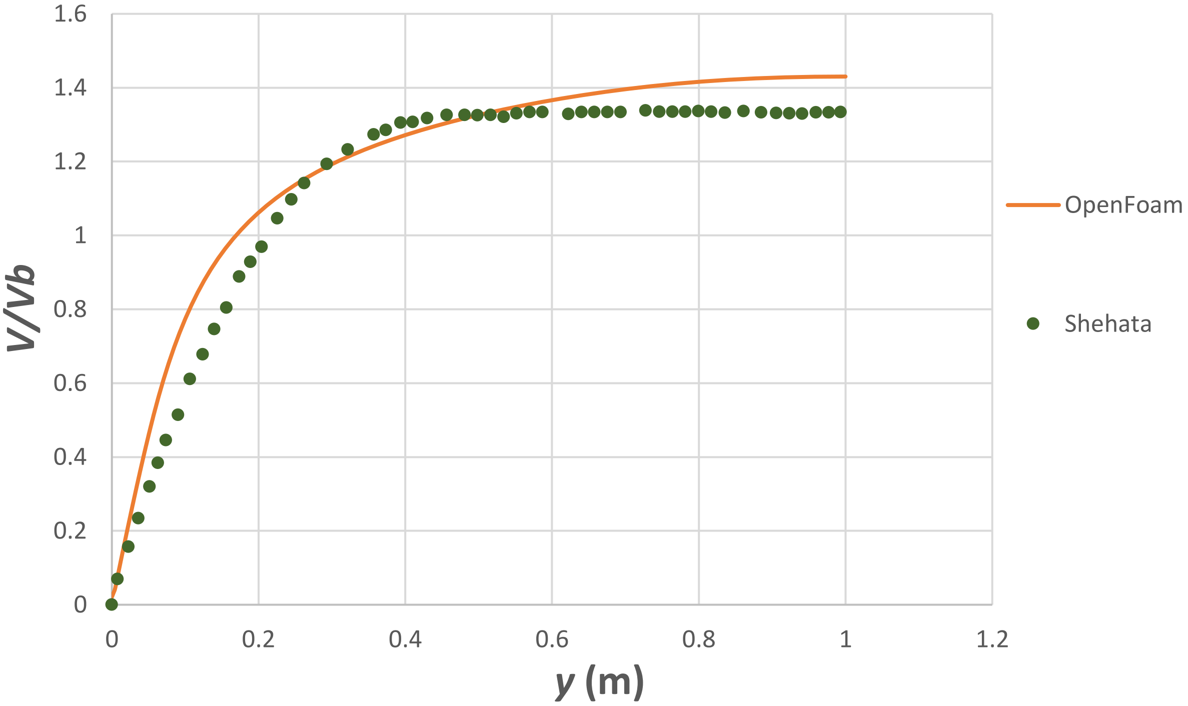

Figure A.20: 24.5 mean axial velocity profile of Run 445.

Bibliography

1. Jackson J. D., Cotton M. A., Axcell B. P., Studies of mixed convection in vertical tubes, International Journal of Heat and Fluid Flow 10 (1989) 2-15
2. Wang J., Li J., Jackson J. D., A study of the influence of buoyancy on turbulent flow in a vertical plane passage, International Journal of Heat and Fluid Flow 25 (2004) 420-430.
3. Zhang X., Dutta S., Heat transfer analysis of buoyancy-assisted mixed convection with asymmetric heating conditions, International Journal of Heat and Mass Transfer 41 (1998) 3255-3264.
4. Kasagi N., Nishimura M., Direct numerical simulation of combined forced and natural turbulent convection in a vertical plane channel, International Journal of Heat and Fluid Flow 18 (1997) 88-99.
5. Shitsman M. E., Natural convection effect on heat transfer to a turbulent water flow in intensively heated tubes at supercritical pressures, Institution of Mechanical Engineers 182 (1967).
6. Ackerman J. W., Pseudoboiling heat transfer to supercritical pressure water in smooth and ribbed tubes, J. Heat Transfer 92 (1970) 490-497.
7. Steiner A. A., On the reverse transition of a turbulent flow under the action of buoyancy forces, Journal of Fluid Mechanics 47 (1971) 503-512.
8. Kenning D. B. T., Shock R. A. W., Poon J. Y. M., Local reduction in heat transfer due to buoyancy effects in upward turbulent flow, IHTC 5 (1974) 139-143.
9. Fewster J., Mixed forced and free convective heat transfer to supercritical pressure fluids flowing in vertical pipes, The University of Manchester (1976).
10. Hall W. B., Jackson J. D., Watson A., A review of forced convection heat transfer to fluids at supercritical pressures, Institution of Mechanical Engineers 182 (1967) 10-22.
11. Jackson J. D., Fluid flow and convective heat transfer to fluids at supercritical pressure, Nuclear Engineering and Design 264 (2013) 24-40.
12. Bergles A. E., The implications and challenges of enhanced heat transfer for the chemical process industries, Trans IChemE 79 (2001) Part A.
13. Popov I., Industrial applications of heat transfer enhancement: The modern state of the problem (a Review), Thermal Engineering 59 (2012).
14. Liebenberg L., Meyer J. P., In-tube passive heat transfer enhancement in the process industry, Applied Thermal Engineering 27 (2007) 2713-2726.
15. Arsenyeva O. P., Smith R., Bulatov I., Tovazhnyanskyy L. L., Kaputsenko P. O., Khavin G. L., Estimation of enhanced heat transfer area targets in process industries, ESCAPE 23 (2013).
16. Bayrak E., Olcay A. B., Recent developments in passive heat transfer enhancement techniques for microcooling technology, International Academic Research Congress (2017).
17. Krishnasamy K., Heat transfer enhancement in waste heat recovery system, National Conference on Smart Energy Systems for Sustainable Development (2017).
18. Jiang B., Dehong X., Guo H., Xiao L., Qu H., Liu X., Efficient waste heat recovery system for high-temperature solid particles based on heat transfer enhancement, Applied Thermal Engineering 155 (2019) 166-174.
19. Bejan A., Kraus A. D., Heat Transfer Handbook (2003).
20. Mills, A. F., Basic heat and mass transfer (1999).
21. Dewan A., Mahanta P., Raju K. S., Kumar P. S., Review of passive heat transfer augmentation techniques, Journal of Power of Energy 218 (2004).
22. Ji W. T., Jacobi A. M., He Y. L., Tao W. Q., Summary and evaluation on single-phase heat transfer enhancement techniques of liquid laminar and turbulent pipe flow, International Journal of Heat and Mass Transfer 88 (2015) 735-754.
23. Rabas T. J., Webb R. L., Thors P., Kim N., -K., Influence of Roughness Shape and Spacing on the Performance of Three-Dimensional Helically Dimpled Tubes, Journal of Enhanced Heat Transfer 1 (1994) 53-64.

24. Suresh S., Chandrasekar M., Chandra Sekhar S., Experimental studies on heat transfer and friction factor characteristics of CuO/water nanofluid under turbulent flow in a helically dimpled tube, Experimental Thermal and Fluid Science 35 (2011) 542-549.
25. Liao Q., Xin M. D., Experimental Investigation on Forced Convective Heat Transfer and Pressure Drop of Ethylene Glycol in Tubes with Three-Dimensional Internally Extended Surface, Experimental Thermal and Fluid Science 11 (1995) 343-347.
26. Li X., Meng J., Guo Z., Turbulent flow and heat transfer in discrete double inclined ribs tube, International Journal of Heat and Mass Transfer 52 (2009) 962-970.
27. Darzi A. A. R., Farhadi M., Sedighi K., Experimental investigation of convective heat transfer and friction factor of Al_2O_3/water nanofluid in helically corrugated tube, Experimental Thermal and Fluid Science 57 (2014) 188-199.
28. Garcia A., Solano J. P., Vicente P. G., Viedma A., The influence of artificial roughness shape on heat transfer enhancement: Corrugated tubes, dimpled tubes and wired coils, Applied Thermal Engineering 35 (2012) 196-201.
29. Smithberg E., Landis F., Friction and Forced Convection Heat-Transfer Characteristics in Tubes with Twisted Tape Swirl Generators, Journal of Heat Transfer 86 (1964) 39-48.
30. Gowen R. A., Smith J. W., Turbulent Heat Tranfer from Smooth and Rough Surfaces, International Journal of Heat and Mass Transfer 11 (1968) 1657-1673.
31. Nikuradse J., Laws of flow in rough pipes, VDI Forschungsheft 361 (1933).
32. Colebroook C. F., Turbulent flow in pipes, with particular reference to the transition region between the smooth and rough pipe laws, Journal of the Institution of Civil Engineers 11 (1939) 133-156.
33. Robinson S. K., Coherent motions in the turbulent boundary layer, Annual Review of Fluid Mechanics 23 (1991) 601-639.
34. Nieuwstadt F. T. M., Boersma B. J., Westerweel J., Turbulence, Introduction to theory and applications of turbulent flows (2016).
35. Soleimani S., Eckels S., A review of drag reduction and heat transfer enhancement by riblet surfaces in closed and open channel flow, International Journal of Thermofluids 9 (2020).
36. Nunner W., Heat transfer and pressure drop in rough tubes, VDI-Forschungsheft 22 (1956) 5-39.
37. Owen P., Thomson W., Heat transfer across rough surfaces, Journal of Fluid Mechanics 15 (1963) 321-334.
38. Dipprey D. F., Sabersky R. H., 1962, Heat and momentum transfer in smooth and rough tubes at various Prandtl numbers, International Journal of Heat and Mass Transfer 6 (1963) 329-353.
39. Webb R. L., Heat transfer and friction in tubes with repeated-rib roughness, International Journal of Heat and Mass Transfer 14 (1971) 601-617.
40. Hosni M. H., Coleman H. W., Roughness element shape effects on heat transfer and skin friction in rough-wall turbulent boundary layers, International Journal of Heat and Mass Transfer 36 (1993) 147-153.
41. Hosni M. H., Coleman H, Taylor R. P., Measurements and calculations of rough-wall heat transfer in the turbulent boundary layer, International Journal of Heat and Mass Transfer 34 (1991) 1967-1082.
42. Katoh K., Choi K. S., Azuma T., Heat-transfer enhancement and pressure loss by surface roughness in turbulent channel flows, International Journal of Heat and Mass Transfer 43 (2000) 4009-4017.
43. Bons J., A critical assessment of Reynolds analogy for turbine flows, J. Heat Transfer 127 (2005) 472-485.
44. Forooghi P., Weidenlener A., Magagnato F., Böhm B., Kubach H., Koch T., Frohnapfel B., DNS of momentum and heat transfer over rough surfaces based on realistic combustion chamber deposit geometries, International Journal of Heat and Fluid Flow 69 (2018) 83-94.
45. Choi K. S., Orchard D. M., 1997, Turbulence management using riblets for heat and momentum transfer, Experimental Thermal and Fluid Science 15 (1997) 109-124.
46. Afanasyev V. N., Chudnovsky Ya. P., Leontiev A. I., Roganov P. S., Turbulent flow friction and heat transfer characteristics of spherical cavities on a flat plate, Experimental Thermal and Fluid Science 7 (1993) 1-8.
47. Chen J., Muller-Steinhagen H., Duffy G. G., Heat transfer enhancement in dimpled tubes, Applied Thermal Engineering 21 (2001) 535-547.

48. Boles J., Milligan R., The advantages and costs of higher-fidelity turbulence modeling, High Performance Computing Modernization Program Users Group Conference (2010).
49. Boussinesq J., Théorie de l'Ecoulement Tourbillant, Mém. prés. Acad. Sci., Vol. XXIII, 1877, p. 46.
50. Alfonsi G., Reynolds-Averaged Navier-Stokes Equations for Turbulence Modeling, Applied Mechanics Reviews (2009) 62 (4).
51. Mellor G.L., Herring H.L., A Survey of the Mean Turbulent Field Closure Models, AIAA J. 11 (1973) 590-599.
52. Spalart P.R., Allmaras S.R., A one-equation turbulence model for aerodynamic flows, La Recherche Aerospatiale 1 (1994) 5-21.
53. Menter F.R., Two-Equation Eddy-Viscosity Turbulence Models for Engineering Applications, AIAA J. 32 (1994).
54. Oler A.M., Clifford C.E., Kimber M. L., Quantitative assessment of eddy viscosity rans models for turbulent mixed convection in a differentially heated plane channel, International Journal of Heat and Mass Transfer 161 (2020).
55. Gentry A., Roy C., Geffray C., Numerical simulation of steady-state mixed convection sodium flow experiments, Nuclear Engineering and Design 381 (2021).
56. Kim S.Y., Shin D.H., Kim C.S., Park G.C., Cho H.K., Computational fluid dynamics analysis of buoyancy-aided turbulent mixed convection inside a heated vertical rectangular duct, Progress in Nuclear Energy 137 (2021).
57. Wu J.Y., Lv R.R., Huang Y.Y., Yang G., Transverse buoyant jet-induced mixed convection inside a large thermal cycling test chamber with perforated plates, International Journal of Thermal Sciences 168 (2021).
58. Grassi W., Testi D., Evaluation of two RANS turbulence models in predicting developing mixed convection within a heated horizontal pipe, International Journal of Computational Fluid Dynamics 21 (2007) 267-276.
59. https://www.openfoam.com/documentation/user-guide (Last accessed : 26/11/2021)
60. https://caefn.com/tag/buoyantboussinesqpimplefoam (Last accessed : 26/11/2021)
61. https://caefn.com/openfoam/solvers-buoyantpimplefoam (Last accessed : 26/11/2021)
62. https://www.learncax.com/knowledge-base/blog/by-category/cfd/basics-of-y-plus-boundary-layer-and-wall-function-in-turbulent-flows (Last accessed : 26/11/2021)
63. https://www.cfd-online.com/Forums/ (Last accessed : 26/11/2021)
64. Desrayaud G., Lauriat G., Flow reversal of laminar mixed convection in the entry region of symmetrically heated, vertical plate channels, International Journal of Thermal Sciences 48 (2009) 2036-2045.
65. Shehata A.M., McEligot D.M., Mean structure in the viscous layer of strongly heated internal gas flows. Measurements, International Journal of Heat and Mass Transfer 41 (1998) 4297-4313.
66. https://www.engineeringtoolbox.com/ (Last accessed : 26/11/2021)
67. Chang B. H., Mills A. F., Turbulent flow in a channel with transverse rib heat transfer augmentation, Int J. Heat Mass Transfer 36 (1993) 1459-1469.
68. Karwa R., Experimental studies of augmented heat transfer and friction in asymmetrically heated rectangular ducts with ribs on the heated wall in transverse, inclined, v-continuous and v-discrete pattern, Int. Comm. Heat Mass Transfer 30 (2003) 241-250.
69. San J. Y., Huang W. C., Heat transfer enhancement of transverse ribs in circular tubes with consideration of entrance effect., , Int J. Heat Mass Transfer 49 (2006) 2965-2971.
70. Kundu P. K., Cohen I. M., Dowling D. R., Fluid mechanics, Sixth edition (2016).